University of Tennessee, Knoxville
Trace: Tennessee Research and Creative Exchange

Doctoral Dissertations | Graduate School

5-2014

Neutron Scattering Studies of Cuprates and Iron Pnictides

Mengshu Liu
University of Tennessee - Knoxville, mliu8@utk.edu

This Dissertation is brought to you for free and open access by the Graduate School at Trace: Tennessee Research and Creative Exchange. It has been accepted for inclusion in Doctoral Dissertations by an authorized administrator of Trace: Tennessee Research and Creative Exchange. For more information, please contact trace@utk.edu.

To the Graduate Council:

I am submitting herewith a dissertation written by Mengshu Liu entitled "Neutron Scattering Studies of Cuprates and Iron Pnictides." I have examined the final electronic copy of this dissertation for form and content and recommend that it be accepted in partial fulfillment of the requirements for the degree of Doctor of Philosophy, with a major in Physics.

Pengcheng Dai, Major Professor

We have read this dissertation and recommend its acceptance:

Hanno Weitering, Takeshi Egami, Adriana Moreo, Haidong Zhou

Accepted for the Council:
Carolyn R. Hodges

Vice Provost and Dean of the Graduate School

(Original signatures are on file with official student records.)

Neutron Scattering Studies of Cuprates and Iron Pnictides

A Dissertation

Presented for the

Doctor of Philosophy

Degree

The University of Tennessee, Knoxville

Mengshu Liu

May 2014

© by Mengshu Liu, 2014

All Rights Reserved.

To

my husband Xiangshi and my unborn daughter

Acknowledgements

Firstly I owe enormous thanks to my supervisor, Pengcheng Dai for his guidance and insight throughout my graduate studies. During my six years in the group, I have found in him limitless energy, deep passion for research, and infectious optimism. Not many students are afforded the opportunities for doing experiments worldwide and supports that I have received, and I thank him for that.

I would also like to acknowledge my collaborators at various neutron sources: Dr.Toby Perring, Dr. Devashibhai Adroja, Dr. Russell Ewings, and Dr.Tatiana Guidi at ISIS, Dr.Louis-Pierre Regnault, Dr.Jiri Kulda at ILL. They offered me generous help during experiments. Special thanks go to Dr.Perring and Dr.Adroja, who have saved me many times from troubles in the lab.

I would like to acknowledge the senior members of Dr.Dai's research group: Dr.Clarina De La Cruz, Dr.Chenglin Zhang, Dr.Jun Zhao, Dr.Oliver Lipscombe, Dr.Songxue Chi, Dr. Huiqian Luo, and Dr. Shiliang Li, whom have taught me a lot. I especially need to thank Clarina, who is the most cheerful girl I know, and a true friend.

Thanks to my peer colleagues, Dr.Leland Harriger, Dr. Miaoyin Wang, Yu song, Scott Carr, Xingye Lu, Meng Wang. It's been a great pleasure to play neutrons with them 3 AM in the lab.

I also need to thank Dr. Hanno Weitering for his guidance and support during my last year at UT.

Finally I would like to thank my parents, and Xiangshi, for their unconditional love.

Abstract

Presented within are neutron scattering studies of several different high temperature superconducting materials: $BaFe_{1.9}Ni_{0.1}As_2$[Barium Iron Nickel Arsenic], $BaFe_{1.85}Ni_{0.15}As_2$[Barium Iron Nickel Arsenic], $Ba_{0.67}K_{0.33}Fe_2As_2$[Barium Potassium Iron Arsenic], and $Pr_{0.88}LaCe_{0.12}CuO_{4-\delta}$[Praseodymium Lanthanum Cerium Copper Oxide]. The main focus is on the magnetic excitations within the systems.

For $BaFe_{1.9}Ni_{0.1}As_2$ [Barium Iron Nickel Arsenic], we measured the intensity of its magnetic excitations and compared the results with excitations in antiferromagnetic non-superconducting $BaFe_2As_2$[Barium Iron Arsenic]. We find electron-doping only affects spin excitations below 100 meV while the total size of the magnetic moment and the energy distribution do not change much. It shows that the magnetic moments in both materials are similar to insulating copper oxides, an indicator of the importance of strong electron correlations in high temperature superconductivity.

For both $BaFe_{1.85}Ni_{0.15}As_2$[Barium Iron Nickel Arsenic] and $Ba_{0.67}K_{0.33}Fe_2As_2$[Barium Potassium Iron Arsenic], we use polarized inelastic neutron scattering to study

their low-energy spin excitations and their spatial anisotropy. Our neutron polarization analysis reveals that magnetic excitations are isotropic for the in-plane and out-of-plane components in both the normal and superconducting states for $BaFe_{1.85}Ni_{0.15}As_2$[Barium Iron Nickel Arsenic], while in $Ba_{0.67}K_{0.33}Fe_2As_2$[Barium Potassium Iron Arsenic] large difference in spin gaps were found. A comparison of these results with those of undoped $BaFe_2As_2$[Barium Iron Arsenic] and optimally electron-doped $BaFe_{1.9}Ni_{0.1}As_2$[Barium Iron Nickel Arsenic] suggests that the spin anisotropy observed $Ba_{0.67}K_{0.33}Fe_2As_2$[Barium Potassium Iron Arsenic]are likely due to their proximity to their parent compound, where spin anisotropy exists below TN [Neel Temperature], while the neutron spin resonance is isotropic in the overdoped regime, consistent with a singlet to triplet excitation.

For as-grown and optimal superconducting $Pr_{0.88}LaCe_{0.12}CuO_{4-\delta}$[Praseodymium Lanthanum Cerium Copper Oxide] (PLCCO), we measured their magnetic excitations over a wide energy range, and compared their corresponding results. The spectra is considerably larger throughout the whole zone in as-grown PLCCO, than in the optimal superconducting PLCCO, which is very different from the $BaFe_2As_2$[Barium Iron Arsenic]system.

Preface

Portions of this dissertation are derived from published work. The publication information of each work is listed with its corresponding chapter.

Chapter 4

Mengshu Liu, Leland W. Harriger, Huiqian Luo, Meng Wang, R. A. Ewings, T. Guidi, Hyowon Park, Kristjan Haule, Gabriel Kotliar, S. M. Hayden, Pengcheng Dai. Nature, 8(5), 376381, (2012).

Chapter 5

Mengshu Liu, C. Lester, Jiri Kulda, Xinye Lu, Huiqian Luo, Meng Wang, S. M. Hayden, Pengcheng Dai. Physical Review B, 85(21), 214516, (2012).

Chapter 6

Chenglin Zhang, Mengshu Liu, Yixi Su, Louis-Pierre Regnault, Meng Wang, Guotai Tan, Th. Bruckel, Takeshi Egami, Pengcheng Dai. Physical Review B, 87(8), 081101, (2013).

Table of Contents

1 Introduction **1**

1.1 Superconductivity 1

1.1.1 Conventional Superconductivity 2

1.1.2 Unconventional Superconductivity 3

1.2 Excitations 4

1.2.1 Spin Waves in Localised Magnets 4

1.2.2 Spin Excitations in Itinerant Magnets 6

2 Introduction to Neutron Scattering **9**

2.1 Neutron Scattering Cross-Section 9

2.2 The Nuclear Interaction 12

2.3 The Magnetic Interaction 13

3 Crystal Growth **16**

3.1 The Method of Traveling Solvent Floating Zone Growth 17

3.2 Preparing for the Growth of PLCCO 19

3.2.1 The Feed Rod 19

3.2.2 The Solvent 20

3.3 The Growing Procedure of PLCCO 21

3.4 Flux Method 22

4 Magnetic Excitations in Optimal Doped $BaFe_{1.9}Ni_{0.1}As_2$ 29

4.1 Introduction 30

4.2 Experimental Results 31

4.3 Theoretical Calculation 35

4.4 Conlusion 40

5 Magnetic Excitations in Overdoped $BaFe_{1.85}Ni_{0.15}As_2$ 50

5.1 Introduction 51

5.2 Experimental Details 56

5.3 Experimental Results 64

5.4 Discussion and Conclusions 70

6 Magnetic Excitations in Optimally Hole-doped $Ba_{0.67}K_{0.33}Fe_2As_2$ 72

6.1 Introduction 73

6.2 Experimental Details 78

6.3 Experimental Results 84

6.4 Conlusion 84

7 Magnetic Excitations in $Pr_{0.88}LaCe_{0.12}CuO_{4-\delta}$ 86

7.1 Introduction 86

7.2 Experimental details 90

7.3 Conclusion 96

Bibliography **99**

Vita **120**

List of Figures

1.1 (Top) History of the transition temperature Tc for the first 70 years following the discovery of superconductivity in 1911. The A-15 compounds were of particular interest in the search for higher Tc - superconductors. (Bottom) Overview of superconducting metals (blue) in the periodic table. Note the absence of superconductivity in the ferromagnetic transition metals and rare-earth and actinide metals. Other superconductors (under pressure) are marked in red. The superconducting transition temperature Tc is indicated. 7

1.2 a microscopic view of spin orientations in a ferromagnetic spin wave state. 8

1.3 Schematic diagram for how spin-wave dispersion enters into the Stoner continuum. 8

2.1 The scattering triangle, relating the incident and final wavevectors to the scattering wavevector. 10

3.1 Overview of different methods of crystal growth reproduced from [Müller and Friedrich, 2005], with the two main method in growing high T_C superconductors in bold. 23

3.2 a) Floating zone furnace at the University of Tennessee which is used for the growth of PLCCO. b) Principles of operating the furnace[Revcolevschi and Jegoudez, 1997]. 24

3.3 a) A hypothetical binary phase diagram of peritectic crystal growth of β, reproduced from[Revcolevschi and Jegoudez, 1997]. b) A schematic plot showing the steady state growth conditions and the compositional variations throughout the growing process. 25

3.4 On the left is a photo taken during the growth of a PLCCO crystal using the floating zone at the University of Tennessee; On the right is a schematic plot of different parts of a growing crystal. 26

3.5 An array of aligned PLCCO single crystals, with total mass 25g. . . 27

3.6 Neutron diffraction pattens of the aligned PLCCO shown in Fig.5 (Data taken at ALF, ISIS). The left shows the (0,0,L) Bragg peak, with a satellite peak to its right; The right shows the (H,H,0) Bragg peak, corresponding to the main (0,0,L) Bragg peak. 28

3.7 An array of $Ba_{1.9}Ni_{0.1}Fe_2As_2$ single crystals grown at IOP, Beijing [Chen et al., 2011]. 28

4.1 (a) AF spin structure of $BaFe_2As_2$ with Fe spin ordering. The effective magnetic exchange couplings along different directions are depicted. (b) RPA and LDA+DMFT calculations of $\chi''(\omega)$ in absolute units for $BaFe_2As_2$ and $BaFe_{1.9}Ni_{0.1}As_2$. (c) The solid lines show spin awave dispersions of $BaFe_2As_2$ for $J_{1a} \neq J_{1b}$ along the $[1, K]$ and $[H, 0]$ directions obtained in Ref. [Harriger et al., 2011]. The filled circles and upper triangles are spin excitation dispersions of $BaFe_{1.9}Ni_{0.1}As_2$ at 5 K and 150 K, respectively. (d) The solid line shows low energy spin waves of $BaFe_2As_2$. The horizontal bars show the full-width-half-maximum of spin excitations in $BaFe_{1.9}Ni_{0.1}As_2$. 42

4.2 Energy dependence of $\chi''(\omega)$ for $BaFe_2As_2$ (filled blue circles) and $BaFe_{1.9}Ni_{0.1}As_2$ below (filled red circles) and above (open red circles) T_c. The solid and dashed lines are guide to the line. The vertical error bars indicate the statistical errors of one standard deviation. The horizontal error bars in (e) indicate energy integration range. 43

4.3 Constant-energy slices through the magnetic excitations of $BaFe_{1.9}Ni_{0.1}As_2$ at different energies in several Brillouin zones. The images were obtained after subtracting the background integrated from $1.8 < H < 2.2$ and $-0.2 < K < 0.2$. The color bars represent the vanadium normalized absolute spin excitation intensity in the units of mbarn/sr/meV/f.u and the dashed boxes indicate AF zone boundaries for a single FeAs layer. Two dimensional images of spin excitations at (a) $E = 10 \pm 3$, (b) 33 ± 3, (c) 43 ± 3, (d) 60 ± 10, (e) 81 ± 10, (f) 113 ± 10, (g) 135 ± 10, (h) 157 ± 10, and (i) 214 ± 10 meV. 44

4.4 Constant-energy cuts of the spin excitation dispersion as a function of increasing energy along the $[1, K]$ and $[H, 0]$ directions for $BaFe_{1.9}Ni_{0.1}As_2$. The solid lines show identical cuts for spin waves of $BaFe_2As_2$ in absolute units. (a) Constant-energy cut along the $[1, K]$ direction at $E = 25 \pm 5$, (b) 55 ± 5, (c) 95 ± 10, (d) 125 ± 10, (e) 150 ± 10, and (f) 210 ± 10 meV. (g) Constant-energy cut along the $[H, 0]$ direction at $E = 25 \pm 5$, (h) 55 ± 5, and 95 ± 10 meV. The error bars indicate the statistical errors of one standard deviation. 45

4.5 (e) Constant-energy cuts at the neutron spin resonance energy of $E = 9 \pm 1$ meV [Chi et al., 2009] below and above T_c. The solid lines are Gaussian fits on linear backgrounds. (f) Temperature dependence of spin excitations at $E = 90 \pm 5$ meV. (g) Energy dependence of the dynamic spin-spin correlation lengths (ξ) at 5 K obtained by Fourier transform of constant-energy cuts similar to those in Fig. 3a-f and Fig. 4e,f. 46

4.6 For all excitation energies probed ($10 \leq E \leq 200$ meV), the dynamic spin-spin correlation lengths are independent of energy. The solid line shows energy dependence of ξ for $BaFe_2As_2$. The error bars indicate the statistical errors of one standard deviation. 47

4.7 Constant-energy images of the spin excitations as a function of increasing energy for $BaFe_{1.9}Ni_{0.1}As_2$ and $BaFe_2As_2$ in units of mbarns/sr/meV/f.u. (a) $E = 33 \pm 3$, (b) 43 ± 3, (c) 60 ± 10, (d) 81 ± 10, (e) 113 ± 10, (f) 135 ± 10, (g) 157 ± 10, and (h) 214 ± 10 meV. 48

4.8 The Feynman diagrams for the Bethe-Salpeter equation. It relates the two-particle Green's function (χ) with the polarization (χ^0) and the local irreducible vertex function (Γ^{irr}_{loc}). The non-local two-particle Green's function is obtained by replacing the local propagator by the non-local propagator. 49

5.1 (Color online) (a) The schematic antiferromagnetic and superconducting phase diagram of $BaFe_{2-x}Ni_xAs_2$ as determined from neutron diffraction experiments [Luo et al., 2012b]. The present composition is highlighted with an arrow. The inset shows an illustration of quasiparticle excitations from the hole Fermi pocket at the Γ point to the electron pocket at the M point as predicted by Fermi surface nesting theories. (b) The three neutron polarization directions (x, y and z) oriented in the (H, H, L) plane of the reciprocal space. 54

5.2 The relationship between magnetic components M_y and M_z measured by polarized neutron scattering and in-plane (M_{110}) and out-of-plane (M_{001}) dynamic spin susceptibility. The solid arrow denotes the measured magnetic component in a SF channel and the dashed arrow denotes the component measured in a NSF channel. In this geometry, we have $M_z \propto M_{1\bar{1}0} = M_{110}$, due to tetragonal symmetry; and $M_y \sim M_{001}$, given that θ is a small value. 55

5.3 (Color online) Constant-Q scans at $\mathbf{Q} = (0.5, 0.5, 1)$ below and above T_c. Using polarized neutrons, we can measure six independent scattering cross sections: incoming neutrons polarized along the x, y or z directions, with outgoing neutrons flipped (SF), or not flipped (NSF). (a) The raw data for SF scattering at 2 K, denoted as $\sigma^{\mathrm{SF}}_{x,y,z}$; (b) Identical scans in NSF channel, or $\sigma^{\mathrm{NSF}}_{x,y,z}$; (c) SF scattering $\sigma^{\mathrm{SF}}_{x,y,z}$ at 20 K, and (d) NSF scattering $\sigma^{\mathrm{NSF}}_{x,y,z}$ at 20 K. 57

5.4 (Color online) (a) Simulation of unpolarized energy scans using $\sigma_\alpha^{\mathrm{SF}} + \sigma_\alpha^{\mathrm{NSF}}$ with $\alpha = x, y, z$ at 2 K and (b) 20 K. The wave vector is fixed at $\mathbf{Q} = (0.5, 0.5, 1)$. (c) Unpolarized energy scan at $(1/2, 1/2, 1)$ below and above T_c obtained by adding all six channels together. (d) Temperature difference plot between 2 K and 20 K reveals a neutron spin resonance at $E = 7$ meV and negative scattering below 4 meV, very similar to the earlier unpolarized measurements on the same Ni-doping level [Wang et al., 2010]. 58

5.5 (Color online) Neutron polarization analysis used to extract the in-plane (M_{110}) and out-of-plane M_{001} components of spin excitations in $BaFe_{1.85}Ni_{0.15}As_2$ from SF and NSF data in Fig. 2. M_{110} and M_{001} at 2 K are extracted from (a) SF, and (b) NSF data in Figure 3. (d,e) M_{110} and M_{001} at 20 K. The above analysis is based on the assumption that the background scattering for the x, y, and z spin polarizations are different (see eqs. (2) and (3)). However, if we assume that backgrounds are identical for different spin polarizations, we would obtain higher magnetic scattering intensity in the NSF channel compared with that of the SF channel at all measured temperatures and energies. At present, the microscopic origin of such a difference is unclear. (c) The combination of SF and NSF data at 2K. (f) The combination of SF and NSF data at 20K. These data reveal isotropic paramagnetic scattering at the probed energies and temperatures. . 59

5.6 (Color online) Constant-energy scans along the $[H, H, 1]$ direction at the resonance energy of $E = 7$ meV at 2 K for different neutron polarization directions. (a) Neutron SF scattering cross sections for the x, y, and z polarization directions. (b) NSF scattering cross sections. A clear peak is seen at $\mathbf{Q} = (0.5, 0.5, 1)$ in the σ_x^{SF} channel that is absent in the σ_x^{NSF} channel, thus confirming the magnetic nature of the resonance. 62

5.7 (Color online) Constant-energy scans along $(0.5, 0.5, L)$ at the resonance energy of $E = 7$ meV. The σ_x^{SF} and σ_x^{NSF} data show no L dependence. The solid and dashed lines show the expected magnetic scattering intensity assuming an Fe^{2+} form factor. 64

5.8 (Color online) Constant-Q scans at $\mathbf{Q} = (0.5, 0.5, 2)$ at 2 K. (a) The three neutron SF scattering energy scans below T_c, marked as $\sigma_{x,y,z}^{\mathrm{SF}}$. (b) Identical scans in the neutron NSF channel, marked as $\sigma_{x,y,z}^{\mathrm{NSF}}$. . . 66

5.9 (Color online) Constant-Q scans at $\mathbf{Q} = (0.5, 0.5, 2)$ at 2 K. The in-plane (M_{110}) and out-of-plane (M_{001}) magnetic response extracted from the (a) SF data, and (b) NSF data, respectively; (c) The combination of SF and NSF data at 2 K shows no difference between the two magnetic moment components, indicating isotropic paramagnetic scattering. . 68

6.1 (Color online) Neutron polarization analysis determined c-axis ($\chi''_c \propto M_{001}$) and in-plane ($\chi''_{a/b} \propto M_{110}$) components of spin excitations in $Ba_{0.67}K_{0.33}Fe_2As_2$ from raw SF constant-Q scans at $\mathbf{Q} = (0.5, 0.5, 0)$ and and $(0.5, 0.5, 2)$. To extract M_{001} and M_{110}, we use methods described in Ref. [Liu et al., 2012b] and assume $M_{1\bar{1}0} = M_{110}$ in the tetragonal crystal. (a) Energy dependence of M_{001} and M_{110} at $T = 45$ K. (b) Identical scans at $T = 2$ K. (c) The solid and open circles show the temperature difference (2 K−45 K) for M_{001} and M_{110}, respectively. (d) The sum of $\sigma^{\mathrm{SF}}_{xx} + \sigma^{\mathrm{SF}}_{yy} + \sigma^{\mathrm{SF}}_{zz}$ at 45 and 2 K. Since background scattering is not expected to change between these temperatures [Zhang et al., 2011], such a procedure will increase statistics of magnetic scattering. The black data points are collected at $\mathbf{Q} = (0.5, 0.5, 0)$ with $k_f = 2.66$ Å^{-1}, while the red data points are at $\mathbf{Q} = (0.5, 0.5, 1)$ with $k_f = 3.84$ Å^{-1}. The solid and dashed lines are guided to the eyes. 76

6.2 (Color online) Constant-Q scans at $\mathbf{Q} = (0.5, 0.5, 1)$ below and above T_c. (a) Energy dependence of M_{001} and M_{110} at $T = 45$ K and (b) at 2 K. The superconductivity-induced spin gaps are at ≤ 2 and 7 meV for M_{001} and M_{110}, respectively. At resonance energy of $E_r = 15$ meV, the scattering is isotropic. (c) The solid and open circles show the temperature difference (2 K−45 K) for M_{001} and M_{110}, respectively. (d) The sum of $\sigma_{xx}^{\mathrm{SF}} + \sigma_{yy}^{\mathrm{SF}} + \sigma_{zz}^{\mathrm{SF}}$ at 45 and 2 K. The solid and dashed lines are guided to the eyes. 77

6.3 (Color online) Energy dependence of spin anisotropy as determined by the difference between $M_{001} - M_{110}$ for temperatures (a) 45 K and (b) 2 K at wave vector $\mathbf{Q} = (0.5, 0.5, 0)$ and $\mathbf{Q} = (0.5, 0.5, 2)$. Similar differences above (c) and below (d) T_c at $\mathbf{Q} = (0.5, 0.5, 1)$. The energy width is broader in (d) compared with (b). The solid and dashed lines are guided to the eyes. 79

6.4 (Color online) Constant-energy scans along the $[H, H, 0]$ and $[H, H, 1]$ directions at an energy transfer of $E = 4$ meV for different neutron polarization directions. (a) Neutron SF scattering cross sections $\sigma_{xx}^{\mathrm{SF}}$, $\sigma_{yy}^{\mathrm{SF}}$, and $\sigma_{zz}^{\mathrm{SF}}$ at 45 K along the $[H, H, 0]$ direction. Similar scans along the $[H, H, 1]$ direction at (b) 2 K and (c) 45 K. All data are obtained with $k_f = 2.66$ Å^{-1}. The solid lines are fit by Gaussian. 81

7.1 (a) Phase diagram of electron doped PLCCO. (b) Energy scans showing two crystal field levels in PLCCO. (c) antiferromagnetic spin structure of PLCCO with Cu spin ordering. (d) Pictorial representation of the dispersions of the spin excitations in a classical Heisenberg Hamiltonian. 91

7.2 Constant-energy slices through the magnetic excitations of as grown PLCCO and optimal superconducting PLCCO ($T_C = 24$K) at different energies. The color bars represent the vanadium normalized absolute spin excitation intensity in the units of mbarn/sr/meV/f.u.. Two dimensional images of spin excitations at (a) $E = 4 \pm 1$ meV, (b) 6.5 ± 1.5 meV, (c) 110 ± 10 meV, (d) 130 ± 10 meV, (e) 150 ± 10 meV, (f) 190 ± 10 meV. 94

7.3 Constant-energy cuts of the spin excitation dispersion as a function of increasing energy along the $[-H, H]$ direction for both as-grown PLCCO (filled blue circles) and optimal superconducting PLCCO (filled red circles) Constant-energy cut along the $[-H, H]$ direction at (a) $E = 4 \pm 1$ meV, (b) 6.5 ± 1.5 meV, (c) 110 ± 10 meV, (d) 130 ± 10 meV, (e) 150 ± 10 meV, (f) 190 ± 10 meV. 95

7.4 (a) The dispersion of spin excitations in PLCCO. Thick solid thick lines denote peaks centerd around (0.5, 0.5) and represent the FWHM of a Gaussian fit with the instrument resolution deconvoluted. Black solid line shows dispersion from linear spin wave fit. (b)Energy dependence of $\chi''(\omega)$ for as grown PLCCO (filled blue circles) and optimal superconducting PLCCO (filled red circles) at base temperature. The vertical error bars indicate the statistical errors of one standard deviation. The horizontal error bars indicate energy integration range. The magenta solid line is data from PLCCO with T_C=21K [Wilson et al., 2006b]. The green solid line is data from 11% PLCCO with T_C=25.5K [Fujita et al., 2006]. 97

Chapter 1

Introduction

1.1 Superconductivity

Superconductivity, the resistance-free flow of electrical charges, is an important area of solid state physics with continuing surprises. In 1911, H. Kamerlingh Onnes first discovered superconductivity in Hg at 4.2K, when he found the disappearance of resistance in a solid mercury wire immersed in liquid helium. However, the fact that below a certain critical temperature, Tc, a superconductor has zero electrical resistance does not distinguish it from a perfect conductor. There are a number of physical properties that are necessary for a material to be considered a superconductor, and which distinguish it from a perfect conductor, one of which is the Meissner effect. When a superconductor enters its superconducting state, the magnetic flux is completely excluded from the materials interior and it becomes a

perfect diamagnet, provided any applied magnetic field is not above the materials critical field H_c.

1.1.1 Conventional Superconductivity

After Onnes initial discovery of superconductivity in Hg, many more materials were found to superconducting (Figure 1), though it was not until 1957 when a theoretical understanding of the phenomenon was established, when Bardeen, Cooper, and Schrieffer proposed what has come to be known as the BCS theory. In BCS theory, electrons become bound together by exchange of virtual phonons and form into Cooper pairs, which decrease their energy. These Cooper pairs are bosons and therefore the Pauli exclusion principle does not apply, so if one pair of electrons can save energy by becoming bound together, then other electrons are likely to do the same. Since Cooper pairs are Bosons there is no restriction on the number that exist in any particular quantum state. The binding energy (reduction in energy of the electron pair) is greatest if electrons with equal but opposite momentum become bound together. Once these bound Cooper pairs form long range phase coherence, then the superconducting phase appears. The electron-pairing in this phonon-mediated BCS mechanism was formulated for spin-singlet formation (S=0) with no net angular momentum (L=0) for the paired state, that is,

$$|\uparrow> \otimes |\downarrow> = \frac{1}{\sqrt{2}}(|\uparrow\downarrow> - |\uparrow\downarrow>)) \tag{1.1}$$

1.1.2 Unconventional Superconductivity

The BCS theory suggests that T_c have a fundamental limit of about 25K-30K. This conviction was soon challenged by the paradigm shifting discovery of the copper oxide based superconductors in 1986 with a T_c as high as 140K. The cuprates remained to be the only high T_c superconductors until 2008, when a group of new iron-based superconductors, with a highest T_c 56K was found. This discovery demonstrated that unconventional high T_c superconductivity is not unique for copper oxides and may be just as ubiquitous as the conventional ones The cuprates and iron pnictides differ from the conventional superconductors in that the formation of Cooper pair can no longer be attributed to the electron-lattice coupling. Despite intensive studies, the correct pairing mechanism is still elusive. However, a common feature of these systems is a long range antiferromagnetic ground state in the nonsuperconducting parent which, upon doping, evolves into loosely correlated magnetic excitations coexisting with superconductivity. To date, the pairing mechanism mediated by magnetic fluctuations has been regarded as a leading candidate to resolve the problem of high-T_c superconductivity. A quantitative comparison between the magnetic excitations of both the parent compound and its corresponding doped superconductors will provide direct information on the effect of doping for spin excitations and its relationship to superconductivity.

1.2 Excitations

In an ordered array of atoms, i.e. a crystal lattice, the order can be disrupted by thermally excited lattice vibrations. These are quantized as phonons and their behaviour is described by a dispersion relation, which determines the relationship between the energy of the phonon and wavevector (or momentum). In a magnetically ordered compound the ordered spins can similarly be disrupted by excitations called spin waves which are quantized as magnons. These can be conceptualized as flipped spins that propagate through the material like a wave. Their behaviour is similarly described by a dispersion relation.

1.2.1 Spin Waves in Localised Magnets

Spin waves are collective excitations of a system of ordered magnetic moments, and they can be visualized as single spins flipped from their ground state propagating through the system (Figure 2), which is parameterised by a dispersion relation. As a simple example consider a one-dimensional Heisenberg ferromagnet, i.e. a chain where all the spins are localised and parallel to the +z direction in the ground state, which is described by the eigenfunction —0?. The Heisenberg Hamiltonian can be written as,

$$H = J \sum_i [S_i^z S_{i+1}^z + \frac{1}{2}(S_i^+ S_{i+1}^- + S_i^- S_{i+1}^+)], \tag{1.2}$$

where S_i^α is the α component of the spin S_i on site i, S_i^+ and S_i^- are the annihilation and creation operators for a flipped spin on site i, and J is the exchange constant (negative for a ferromagnet). The ground state is defined so that $H|0? = E0|0?$, with $E_0 = NS^2J$, where N is the number of spins in the chain. An excitation in this ordered system is created by flipping a spin at site j, i.e. the excited state $|j? = S_j^?|0?$. Applying the Hamiltonian to this excited state gives

$$H|j >= (NS^2J - 2SJ)|j > +SJ|j+1 > +1 > SJ|j-1 > \tag{1.3}$$

Considering the Fourier transform $|q >= \sum_j e^{iqr_j}|j >$ then gives

$$H|q >= (E_0 + \hbar\omega)|q >= \left\{NS^2J - 2JS[1 - cos(qa)]\right\}|q >, \tag{1.4}$$

where a is the lattice spacing, and the dispersion of the excitation is given by the expression $\hbar\omega = -2JS[1 - cos(qa)]$, recalling that J is negative for a ferromagnet. It can be shown that for a three dimensional ferromagnet with nearest neighbour interactions this becomes

$$\hbar\omega = -2JS[3 - cos(q_x a) - cos(q_y b) - cos(q_z c)] \tag{1.5}$$

where $q\alpha$ is the αcomponent of the wavevector and a,b,c are the lattice vectors in the directions specified by α. At small wavevectors (q,0,0), for the simple case of a

cubic system, this can be expanded in a Taylor series to give the spin-wave stiffness constant D

$$\hbar\omega = JSa^2q^2 = Dq^2. \tag{1.6}$$

1.2.2 Spin Excitations in Itinerant Magnets

In an metallic (itinerant electron) ferromagnet there exist spin-split Stoner bands, separated by a gap Δ. It is possible to excite an electron from one band to another provided that its spin is flipped during the excitation process. This can be achieved if the electron is excited using a neutron (neutron magnetic inelastic scattering), and the resulting magnetic excitation spectrum, shown by the shaded area is diffuse and isotropic. There is also a line in figure corresponding to dispersive excitations at energies and wavevectors below the threshold of the Stoner continuum. Such localised excitations have been observed in, for example iron [26], where outside the Stoner continuum spin-wave modes can still propagate (Figure 3).

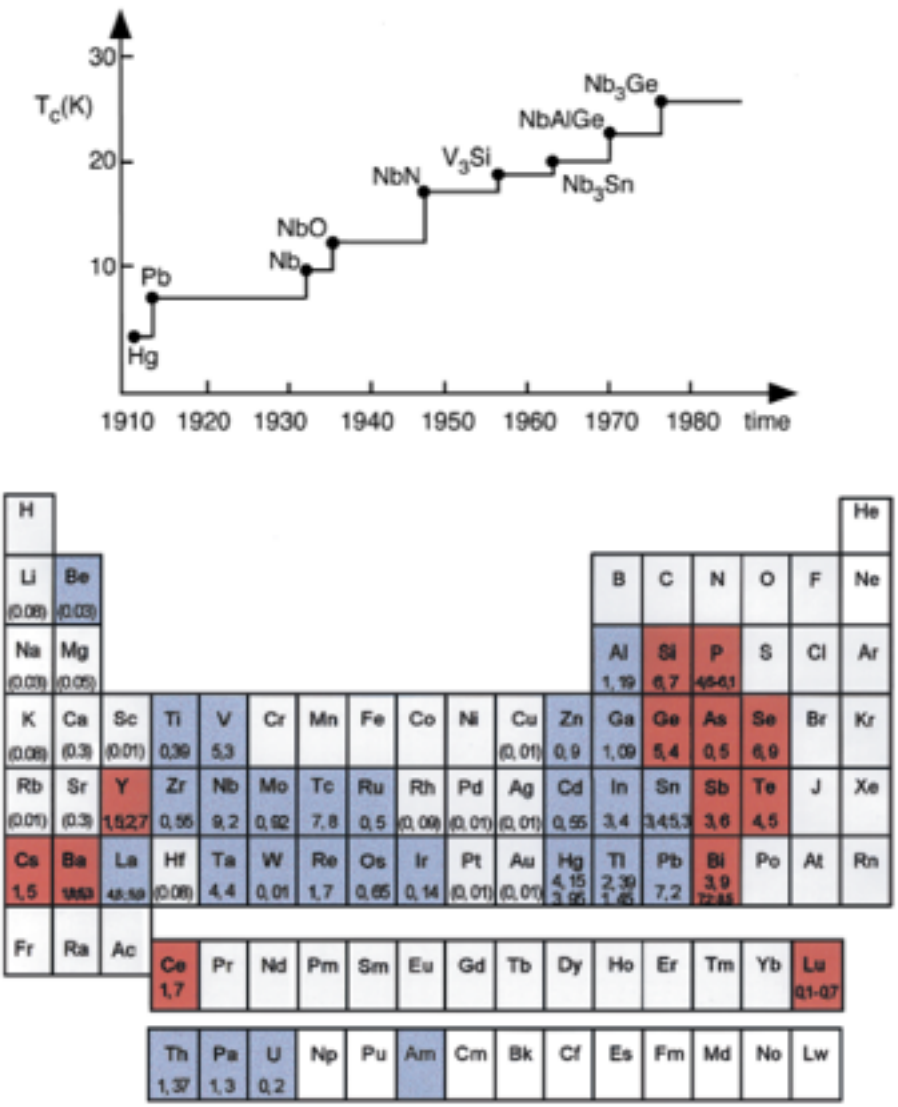

Figure 1.1: (Top) History of the transition temperature Tc for the first 70 years following the discovery of superconductivity in 1911. The A-15 compounds were of particular interest in the search for higher Tc -superconductors. (Bottom) Overview of superconducting metals (blue) in the periodic table. Note the absence of superconductivity in the ferromagnetic transition metals and rare-earth and actinide metals. Other superconductors (under pressure) are marked in red. The superconducting transition temperature Tc is indicated.

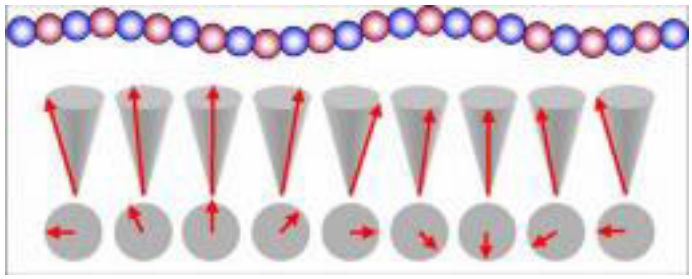

Figure 1.2: a microscopic view of spin orientations in a ferromagnetic spin wave state.

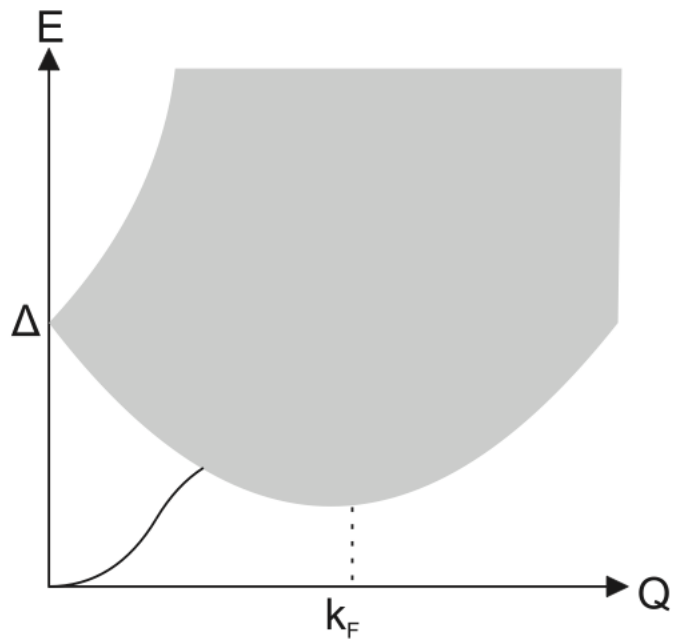

Figure 1.3: Schematic diagram for how spin-wave dispersion enters into the Stoner continuum.

Chapter 2

Introduction to Neutron Scattering

2.1 Neutron Scattering Cross-Section

A neutron scattering event must conserve both momentum and energy, and these simple rules provide a starting point for the theory of neutron scattering (Figure 1). Energy conservation gives us

$$E_i - E_f = \frac{\hbar^2}{2m_N}(\mathbf{k_i}^2 - \mathbf{k_f}^2) = \hbar\omega \tag{2.1}$$

where E_i and E_f are respectively the incident and final energies of the neutron, k_i and k_f are the incident and final neutron wavevectors and $\hbar\omega$ is the energy of excitation in the sample. Meanwhile momentum conservation gives us

$$\mathbf{Q} = \mathbf{K_i} - \mathbf{K_f} \tag{2.2}$$

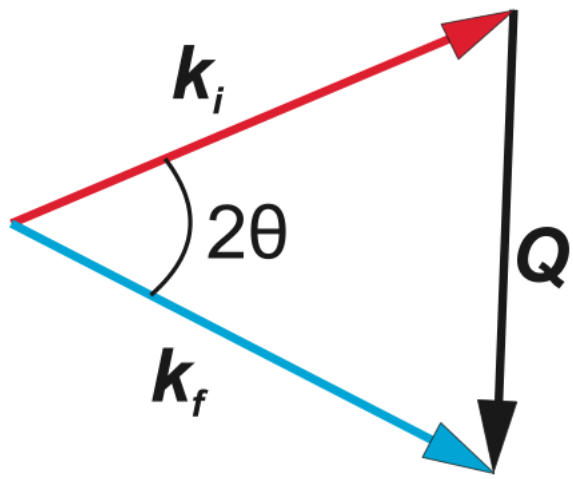

Figure 2.1: The scattering triangle, relating the incident and final wavevectors to the scattering wavevector.

where **Q** is the scattering wavevector. The process is shown schematically in figure 2.1. Taken together equations 2.1 and 2.2 allow us to calculate from a given scattering event the wavevector and energy of the excitations (or static order if $\hbar\omega$ is zero) in the sample. The quantity measured during a neutron scattering experiment is the double differential cross-section, which is defined as:

$$\frac{d^2\sigma}{d\Omega dE} = \frac{A}{dEd\Omega\Phi} \tag{2.3}$$

with A=total number of neutrons scattered per unit time into the solid angle dΩ in the direction θ, ϕ with energy between E and E+dE, and Φ=the total incident neutron flux.

For elastic scattering we do not include the dE term in the denominator, i.e. we are only interested in the differential cross-section dσ. This is because elastic

scattering has a greater probability amplitude than inelastic dΩ scattering, rendering the differentiation with respect to energy redundant, as we assume scattering which is not in the elastic channel to be negligible. So in both nuclear and magnetic elastic scattering it is dσ that is of interest.

To obtain an expression for the partial differential cross-section we consider the probability of a transition of the neutron-target system from an initial state λ_i to a final state λ_f. Since neutron scattering is shown experimentally to be a very weak process the interacting potential between neutron and target can be treated as a perturbation and Fermis Golden Rule can be applied to calculate the transition probability. In scattering theory this is equivalent to the Born approximation which assumes that both the incoming and scattered beam are plane waves. The neutron is described by a plane wave state characterized by its wavevector λ, and the scattering cross section between λ_i and λ_i can be written in the Born approximation as

$$(\frac{d^2\sigma}{d\Omega dE_f})^{\lambda_i}_{\lambda_f} = \frac{k_f}{k_i}(\frac{m_n}{2\pi\hbar^2})^2 | < \lambda_f|V(\mathbf{Q})|\lambda_i > |^2 \delta(E_{\lambda_f} - E_{\lambda_i} - \hbar\omega), \tag{2.4}$$

where $V(\mathbf{Q})$ is the Fourier transform of the neutron-matter interaction potential $V(\mathbf{r})$:

$$V(\mathbf{Q}) = \int V(\mathbf{r}) exp(i\mathbf{Q}\cdot\mathbf{r}) d^3\mathbf{r}. \tag{2.5}$$

The scattering cross-section for whole process is a sum of equation 2.4 over all possible initial and final states of the system, and over all possible initial and final spin-states of the neutron:

$$\frac{d^2\sigma}{d\Omega dE_f} = \frac{k_f}{k_i}(\frac{m_n}{2\pi\hbar^2})^2 \sum_{\sigma_i,\sigma_f} p_{\sigma_i} \sum_{\lambda_i,\lambda_f} p_{\lambda_i} | < \sigma_f \lambda_f | V(\mathbf{Q}) | \sigma_i \lambda_i > |^2 \delta(E_{\lambda_f} - E_{\lambda_i} - \hbar\omega), \quad (2.6)$$

where p_{λ_i} is the probability distribution for initial states λ_i and p_{σ_i} is the probability distribution for the initial spin-states of the neutron σ_i. The spin-states of the neutron will be discussed in detail in section 2.1.4 when we discuss polarized neutron scattering. The scattering cross-section is therefore dependent on the type of interaction between the neutron and the matter it scatters from, and hence the interaction potential $V(\mathbf{r})$ (equation 2.5). The derivations of this potential and the corresponding scattering cross-sections for different interactions are covered in depth in texts by Squires, Lovesey and others. Here we will briefly discuss some results that will be used later.

2.2 The Nuclear Interaction

In any neutron scattering experiment the dominant contribution to the total scattering will come from nuclear elastic scattering which arises from the neutron interacting with nuclei in the sample through the strong nuclear force. Neutrons interact with nuclei j at positions r_j through an interaction potential which can be approximated by

$$V_N(\mathbf{r}) = \frac{2\pi\hbar^2}{m_n} \sum_j \bar{b}_j \delta(\mathbf{r} - \mathbf{r}_j), \tag{2.7}$$

where $\bar{b}_j$are the scattering lengths of each atomic nucleus.

For unpolarized neutrons it is possible to express the partial differential cross-section as a sum of a coherent and incoherent term:

$$\frac{d^2\sigma}{d\Omega dE_f} = \frac{d^2\sigma_{coh}}{d\Omega dE_f} + \frac{d^2\sigma_{incoh}}{d\Omega dE_f} \tag{2.8}$$

The coherent scattering results from interference effects between the nuclei and in a neutron scattering experiment is observed as elastic Bragg scattering and inelastic phonon scattering. The incoherent scattering is observed as an isotropic background, and is usually subtracted before analysis of the coherent scattering, so we neglect this term.

2.3 The Magnetic Interaction

Magnetic scattering of neutrons occurs due to an interaction between the magnetic dipole moment of the incident neutron and the electromagnetic field due to the intrinsic spin and orbital momentum of unpaired electrons in magnetic ions in the sample. The neutron magnetic moment is

$$\boldsymbol{\mu}_n = -\gamma\mu_N\boldsymbol{\sigma}, \tag{2.9}$$

where μ_N is the nuclear magneton, $\gamma \approx 1.913$ is the gyromagnetic ratio and σ is the Pauli spin operator with eigenvalues of ± 1. The interaction potential for magnetic scattering takes the form

$$V_M(\mathbf{r}) = -\boldsymbol{\mu}_n \cdot \mathbf{B}(\mathbf{r}), \tag{2.10}$$

where $\mathbf{B}$ represents the local magnetic flux density from the unpaired electrons of the magnetic ions, due to both their intrinsic spin and orbital motion (angular momentum). It is the Fourier transform of the interaction potential, $V_M(\mathbf{Q})$, that is needed to determine the cross section. Using Maxwells equations, $\mathbf{B}$ can be related to the magnetization $\mathbf{M}$, so that the Fourier transform of the interaction potential can be written as:

$$V_M(\mathbf{Q}) = -\boldsymbol{\mu}_n \cdot \mathbf{B}(\mathbf{Q}) = -\mu_0 \boldsymbol{\mu}_n \cdot \mathbf{M}_\perp(\mathbf{Q}) \tag{2.11}$$

where $\mathbf{M}_\perp(\mathbf{Q})$ is the component of the magnetization perpendicular to the scattering vector $\mathbf{Q}$:

$$\mathbf{M}_\perp(\mathbf{Q}) = \hat{\mathbf{Q}} \times \left\{ \mathbf{M}(\mathbf{Q}) \times \hat{\mathbf{Q}} \right\} \tag{2.12}$$

In ordered magnetic systems magnetic elastic scattering is observed as magnetic Bragg peaks, in an analogous way to nuclear Bragg peaks. Magnetic Bragg peaks arise from scattering from the average magnetic lattice, occurring when the scattering

vector Q coincides with a reciprocal magnetic lattice vector ?M. For example, in a simple antiferromagnetically ordered structure, where the magnetic unit cell is doubled compared to the nuclear unit cell, Bragg peaks would be observed at half-integer wavevectors. The scattering cross-section for magnetic elastic scattering in the dipole approximation is given by

$$(\frac{d^2\sigma}{d\Omega dE_f})_{\text{magnetic elastic}} = \delta(\hbar\omega)\frac{d\sigma_M}{d\Omega}(\mathbf{Q})$$
$$= \frac{N_m(2\pi)^3}{V_{0m}}(\frac{\gamma r_0}{2})^2 \sum_{\alpha\beta} < (\delta_{\alpha,\beta} - \hat{Q}_\alpha \hat{Q}_\beta) F^\alpha(\mathbf{Q}) F^{\beta *}(\mathbf{Q}) > \tag{2.13}$$
$$\times \delta(\mathbf{Q} - \boldsymbol{\tau}_M)\delta(\hbar\omega)$$

The cross section for magnetic inelastic neutron scattering can be written as

$$(\frac{d^2\sigma}{d\Omega dE_f})_{\text{magnetic inelastic}} = (\frac{\gamma r_0}{2})^2 f^2(\mathbf{Q}) e^{-2W(Q,T)} \frac{k_f}{k_i} S(\mathbf{Q}, \omega), \tag{2.14}$$

where $S(\mathbf{Q}, \omega)$ is known as the response function, and is written as

$$S(\mathbf{Q}, \omega) = \sum_{\alpha\beta} < (\delta_{\alpha,\beta} - \hat{Q}_\alpha \hat{Q}_\beta) S^{\alpha,\beta}(\mathbf{Q}, \omega) > . \tag{2.15}$$

Chapter 3

Crystal Growth

Many researches of condensed matter systems would not exist if not the availability of pure high quality single crystals. Therefore [Harriger et al., 2011], the technique to grow bulk single crystals is essential for the understanding of different compounds. There are many techniques available to grow bulk single crystals [Müller and Friedrich, 2005] (Fig. 3.1). The most frequently used methods to grow high T_C superconductors are traveling solvent floating zone (TSFZ) method and the flux method. In this chapter, a brief description is given of the the growth of electron-doped cuprate $Pr_{0.88}LaCe_{0.12}CuO_{4-\delta}$ (PLCCO) using the traveling solvent floating zone (TSFZ) method.

3.1 The Method of Traveling Solvent Floating Zone Growth

The most common method to grow single crystals is the melting method which involves solidification of a material from its melting. TSFZ is one of the many melting methods (Fig. 3.1) using a floating zone furnace (Fig.3.2a). The floating zone furnace has a elliptical shaped mirror with two halogen lamp installed at its two focal points (Fig.3.2.b). Therefore, a high temperature zone is formed in the center of the ellipse. A polycrystalline rod (the feed rod) is placed above the zone, and a single crystal rod (the seed) is placed below the zone, both of which are moving constantly downward. When the feed rod moves into the focused high temperature zone, it melts into liquid. When the liquid gradually moves out of the melting zone, it solidifies, and precipitates on the seed.

In order to control the growing condition so that the melt will precipitate into its corresponding single crystal, the phase diagram needs to be scrutinized. A hypothetical phase diagram of a binary system α - γ, which contains a peritectic compound β is shown in Fig.3.3a. At high temperatures, the composition is in liquid state. While pure α or γ can be crystalized by directly cooling down from liquid (yellow dashed lines), liquid β turns incongruently into liquid phase L and another solid phase α upon cooling,

$$Reaction1 : liquid(P'') \rightarrow liquid(P') \rightarrow liquid(X') + solid(\alpha) \tag{3.1}$$

However, if the cooling starts from liquid with composition x, we have instead,

$$Reaction2 : liquid(X') + solid(\alpha) \rightarrow solid(\beta) \tag{3.2}$$

We can then apply this process to crystal growth using floating furnace:

1) The melting zone is set at a relatively high temperature by manipulating the lamp voltage. The bottom of the feed rod is therefore melted in to all liquid state (point P"). Then the voltage is gradually reduced so that it reaches P' on the liquidus line. This process needs to be done very carefully to prevent any solidifying.

2) The growth is then started with the feed rod gradually moving into the melting zone, and seed moving away from the zone, while temperature is slowly reduced. Therefore, reaction 1 is initiated along the liquidus line, which creates solid α and liquid with changing composition. solid α precipitates on the seed, and the liquid remain in the melting zone. When the temperate is lowed to T_P, the system reaches an equilibrium with liquid with composition X'. This is also why the first section of the new crystal needs to be regarded (Fig.3.3 b)).

3) The temperature then remains at T_p. New part of the feed rod goes into the T_p melting zone, deposed into solid α and liquid with composition X' (Point P). As they are gradually pushed out of the hot zone, the temperature decreased, and they changed into solid β and precipitated on the seed (reaction 2). The vertical speed of the feed rod also needs to be slow so that the liquid in the melting zone remains X'

during the whole growing process. The feed rod and seed are also usually rotating in the opposite direction to improve liquid homogeneity.

Note that, during the whole growth, the system needs to be in equilibrium. Any deviation from the liquidus line will cause the merge of some other impurity phases.

3.2 Preparing for the Growth of PLCCO

3.2.1 The Feed Rod

The polycrystalline feed rod of PLCCO is made of powder Pr_2O_3, La_2O_3, CeO_2, and CuO_2. They have melting points of 2500°C , 2315°C , 2400°C , 1201°C , respectively. To allow a thorough and homogeneous formation of polycrystalline PLCCO, the mixed powder should be sintered at a high temperature but not above melting point to assist atom diffusion. Since CuO_2 only has a relatively low melting point, 1% more CuO_2 is added to the weight in order to take account of any CuO_2 evaporation during growth. It is also due to this reason, the last portion of the crystal growth should be abandoned, because the CuO_2 maybe too significant, rendering a different crystal composition.

The procedure is described below:

1) Preheat the powder Pr_6O_11, La_2O_3, CeO_2, and CuO_2 for 12 hours at 900°C to remove any H_2O in the powders.

2) Pr_6O_11, La_2O_3, CeO_2, and CuO_2 are weighed and mixed stoichiometrically in a timely manner, because these oxides have high water absorption rates.

3) The mixed powder is calcined in furnace at 900°C for 12 hours in air.

4)Grind the mixture in alcohol and cook in furnace at 1000°C for12 hours.

5) Repeat 4) twice more.

6) Cast the powder in a pressure die, and sinter the pellet in furnace at 980°C for 12 hours.

7) Grind the pellet into fine powder again and repeat twice more.

8) Grind the pellet into fine powder, and make a cylinder rod by putting the raw material in a rubber balloon. Press the rod at a hydrostatic pressure of about 100 MPa.

9) Finally, sinter the cylinder rod in oxygen at 1190°C. The repeated sintering can make sure the mixer is homogeneous, and can increase the density of the rod to as close to the single crystal value as possible, so that the feeding material matches the precipitation.

3.2.2 The Solvent

At the beginning of the growth, a liquid region needs to be formed and connects the feed rod and the seed. Then, the liquid region has to have a composition of X" in order to have steady PLCCO single crystal precipitation. However, as shown in the diagram (Fig.3.3a), to fully melt PLCCO, it requires a higher temperature than T_P. In order to quickly form a liquid region, and prevent any possible spill, a solvent pellet consisting of CuO_2 is placed on top of the seed. Upon heating, it first melts into liquid and connects the feed rod and seed. The composition of the solvent should

has a value close to X'. But as long as it's not too far off, the liquid region will be able to automatically balance itself to X' during warming by precipitating any unwanted component as approaching equilibrium (In this case, the pink α phase in Fig.3.3b can be adjusted to α plus unwanted phase from the solvent).

3.3 The Growing Procedure of PLCCO

The growth conditions were as follows. Feed and seed shafts rotates oppositely at rates of 25 rpm. The growth rate was 1.0 mm/h. The atmosphere in the furnace was an oxygen gas under a pressure of 1.0 ? 102 kPa to prevent the vaporization of CuO from the melt.

It is important to have a good quality single crystal seed, since the precipitation will follow the structure of seed. However, the seed cannot be perfect, and may have two or more domains, beside the dominant direction. We usually start the growth at half of its normal rate, creating a "neck" on the single crystal (Fig. 3.4b), before go back to its original growing speed. This process can help eliminate other domains presented in the seed. The growing direction is not fixed, but always has $(0, 0, L)$ vertical to the feed rod moving direction (therefore within the cross section of the cylinder), and the $(H, H, 0)$ direction 30° 50° off the cylinder axis.

Figure 3.5 shows 25 g of aligned PLCCO crystal rods grown following the above procedures. As we can see, the crystals have different angles, meaning they don't render the same direction all the time. The quality of the crystals and alignment are

checked by neutron diffraction (ISIS, ALF). It shows the $(0, 0, L)$ direction has an other crystalline a few degrees away from the main peak, and the alignment was done with the main crystal direction (Fig.3.6).

3.4 Flux Method

Another important growing method is the flux method, and it is widely used to grow iron based superconductors. TSFZ method is out of the question here, because rather than the as grown cuprates, which are insulators, iron based superconductors are bad metals. It will be impossible to have a focused melting region, and a temperature gradient along the crystal, both of which are required for TSFZ.

Flux method is a solution method. Opposite to melting growth where the crystal solidifies from its own melt, in solution growth, the compounds are dissolved in a suitable solvent, and then crystallized due to supersaturation.

Fig.3.7 shows an array of single crystal $Ba_{1.9}Ni_{0.1}Fe_2As_2$ grown using flux method[Chen et al., 2011]. As we can see, the size of the crystals are considerably smaller than PLCCO.

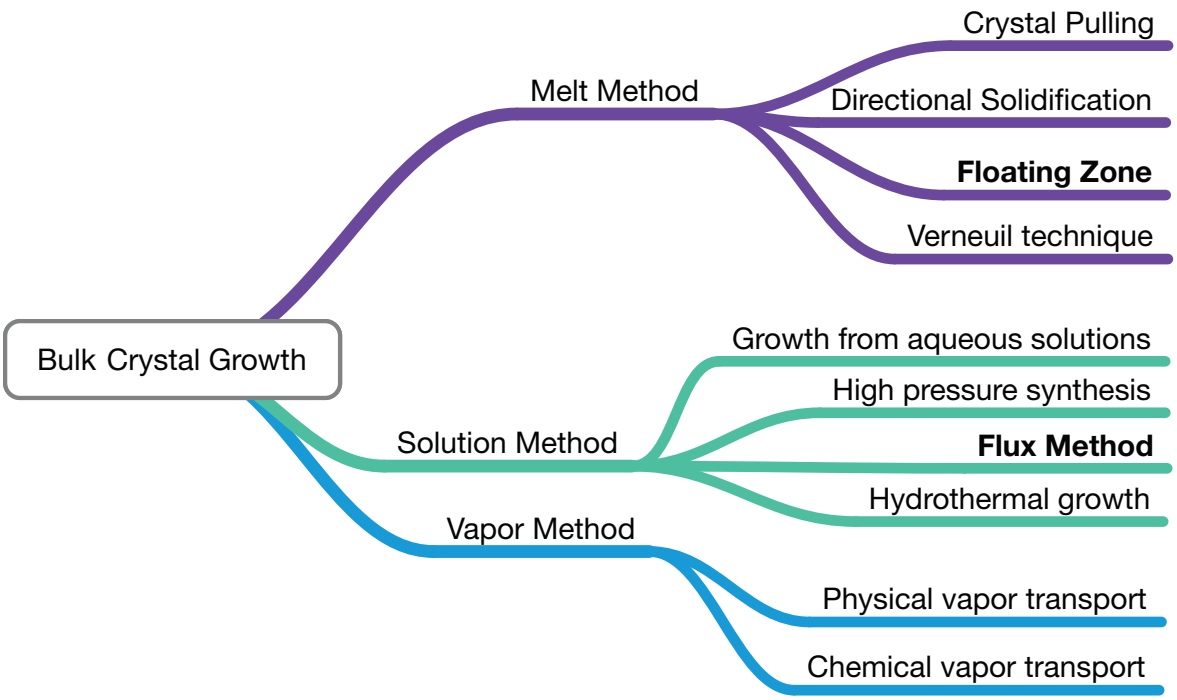

Figure 3.1: Overview of different methods of crystal growth reproduced from [Müller and Friedrich, 2005], with the two main method in growing high T_C superconductors in bold.

a)

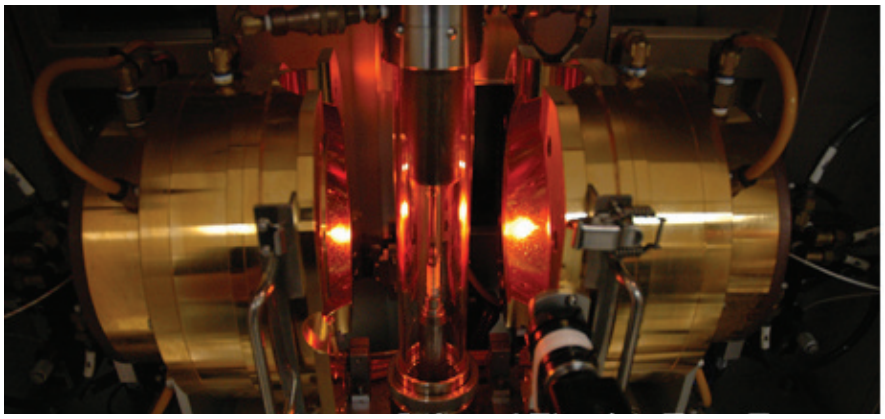

b)

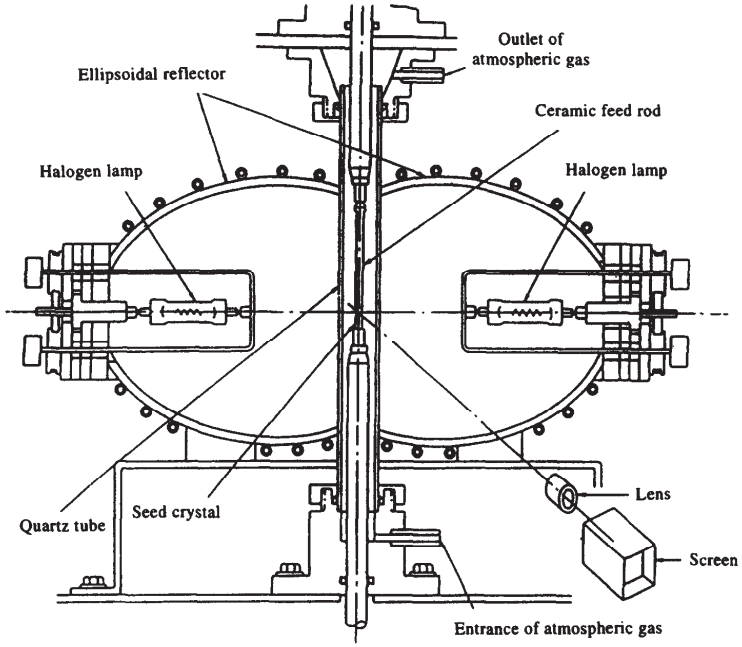

Figure 3.2: a) Floating zone furnace at the University of Tennessee which is used for the growth of PLCCO. b) Principles of operating the furnace[Revcolevschi and Jegoudez, 1997].

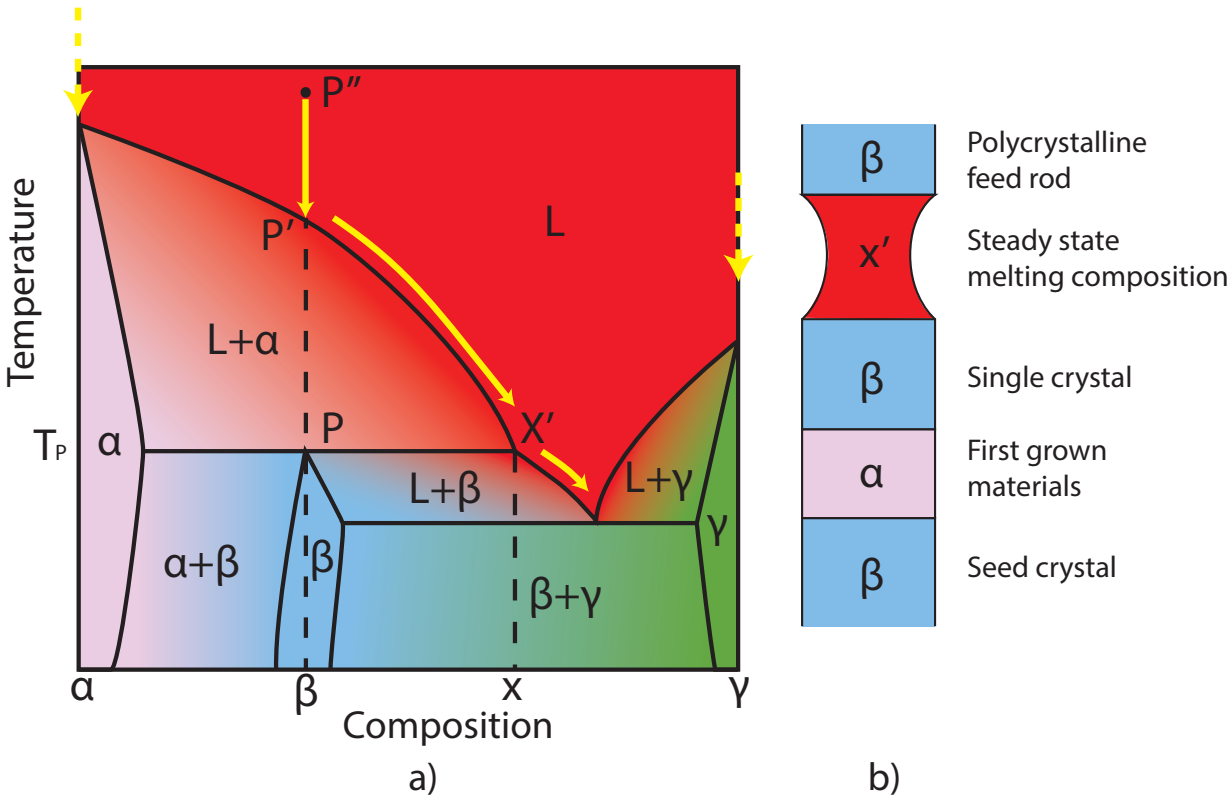

Figure 3.3: a) A hypothetical binary phase diagram of peritectic crystal growth of β, reproduced from[Revcolevschi and Jegoudez, 1997]. b) A schematic plot showing the steady state growth conditions and the compositional variations throughout the growing process.

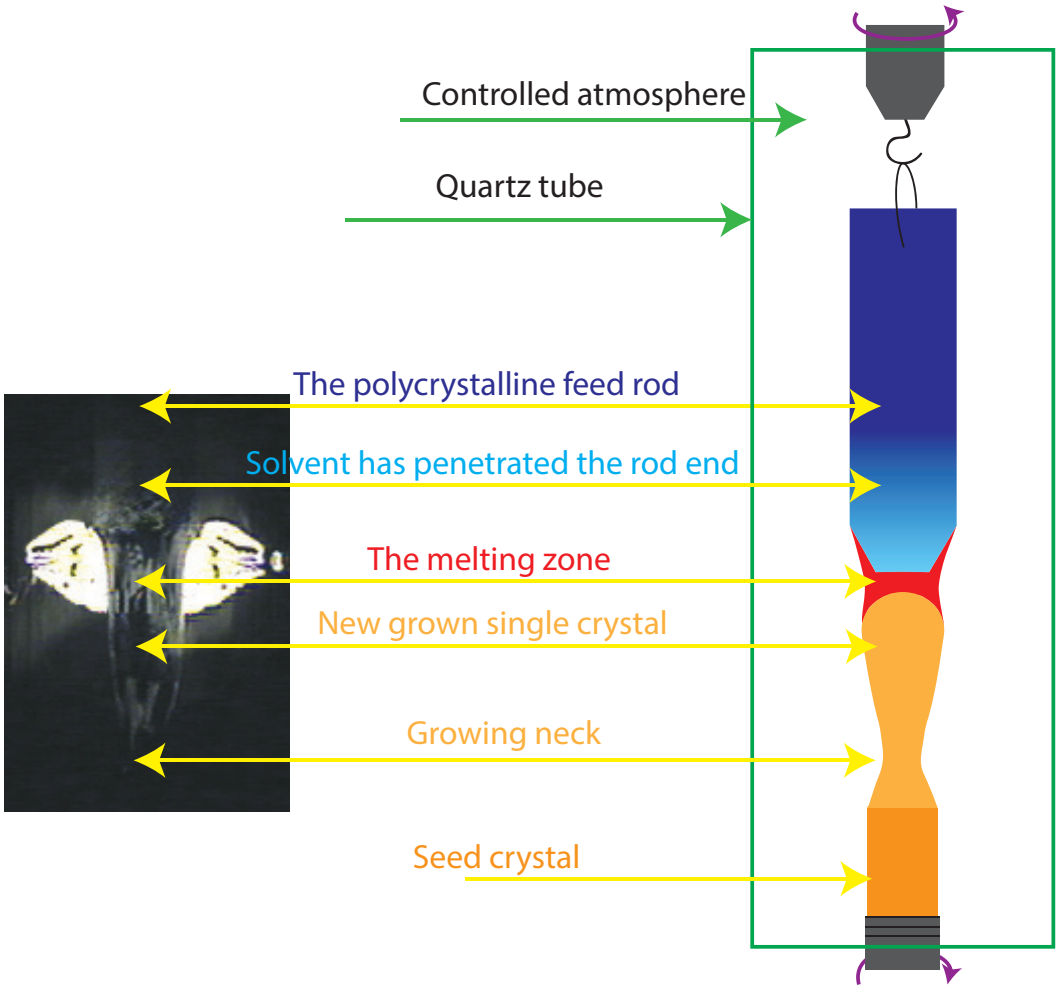

Figure 3.4: On the left is a photo taken during the growth of a PLCCO crystal using the floating zone at the University of Tennessee; On the right is a schematic plot of different parts of a growing crystal.

Figure 3.5: An array of aligned PLCCO single crystals, with total mass 25g.

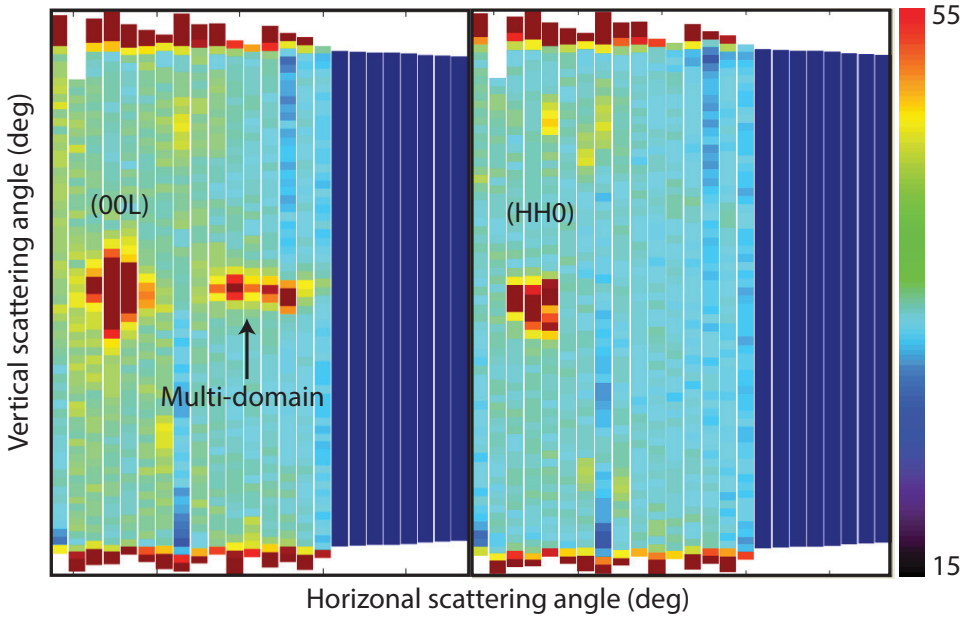

Figure 3.6: Neutron diffraction pattens of the aligned PLCCO shown in Fig.5 (Data taken at ALF, ISIS). The left shows the (0,0,L) Bragg peak, with a satellite peak to its right; The right shows the (H,H,0) Bragg peak, corresponding to the main (0,0,L) Bragg peak.

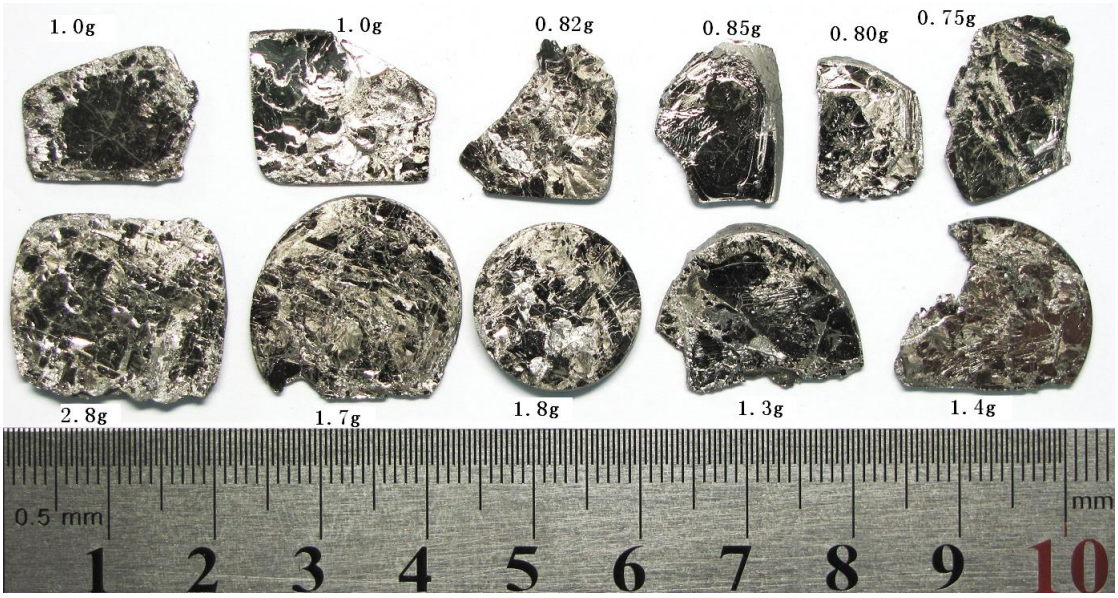

Figure 3.7: An array of $Ba_{1.9}Ni_{0.1}Fe_2As_2$ single crystals grown at IOP, Beijing [Chen et al., 2011].

Chapter 4

Magnetic Excitations in Optimal Doped $BaFe_{1.9}Ni_{0.1}As_2$

Since the discovery of the metallic antiferromagnetic (AF) ground state near superconductivity in iron-pnictide superconductors [Kamihara et al., 2008; de la Cruz et al., 2008b; Paglione and Greene, 2010], a central question has been whether magnetism in these materials arises from weakly correlated electrons [Mazin et al., 2008; Dong et al., 2008], as in the case of spin-density-wave in pure chromium [Fawcett, 1988], requires strong electron correlations [Haule et al., 2008], or can even be described in terms of localized electrons [Si and Abrahams, 2008; Xu et al., 2008] such as the AF insulating state of copper oxides [Lee and Wen, 2006]. Here we use inelastic neutron scattering to determine the absolute intensity of the magnetic excitations throughout the Brillouin zone in electron-doped superconducting $BaFe_{1.9}Ni_{0.1}As_2$ (T_c = 20 K), which allows us to obtain the size of the fluctuating

magnetic moment $\langle m^2 \rangle$, and its energy distribution [Inosov et al., 2009; Lester et al., 2010]. We find that superconducting $BaFe_{1.9}Ni_{0.1}As_2$ and AF $BaFe_2As_2$ [Harriger et al., 2011] both have fluctuating magnetic moments $\langle m^2 \rangle \approx 3.2\ \mu_B^2$ per Fe(Ni), which are similar to those found in the AF insulating copper oxides [Headings et al., 2010; Hayden et al., 1996]. The common theme in both classes of high temperature superconductors is that magnetic excitations have partly localized character, thus showing the importance of strong correlations for high temperature superconductivity [Basov and Chubukov, 2011].

4.1 Introduction

In the undoped state, iron pnictides such as $BaFe_2As_2$ form a metallic low-temperature orthorhombic phase with the AF structure as shown in Fig. 1a [Huang et al., 2008]. Inelastic neutron scattering measurements have mapped out spin waves throughout the Brioullion zone in the AF orthorhombic and paramagnetic tetragonal phases [Harriger et al., 2011]. Upon Co- and Ni-doping to induce optimal superconductivity via electron doping, the orthorhombic structural distortion and static AF order in $BaFe_2As_2$ are suppressed and the system becomes tetragonal and paramagnetic at all temperatures [Lester et al., 2009]. In previous inelastic neutron scattering experiments on optimally electron-doped $Ba(Fe,Co,Ni)_2As_2$ superconductors [Inosov et al., 2009; Lester et al., 2010; Lumsden et al., 2009; Chi et al., 2009; Wang et al., 2010; Li et al., 2010], spin excitations up to $\sim$120 meV were observed. However, the lack

of spin excitations data at higher energies in absolute units precluded a comparison with spin waves in undoped $BaFe_2As_2$. Only the absolute intensity measurements in the entire Brillouin zone can reveal the effect of electron-doping on the overall spin excitations spectra and allow a direct comparison with the results in the AF insulating copper oxides [Headings et al., 2010; Hayden et al., 1996]. For the experiments, we chose to study well-characterized electron-doped $BaFe_{1.9}Ni_{0.1}As_2$ [Chi et al., 2009; Wang et al., 2010] because large single crystals were available [Chen et al., 2011] and their properties are similar to Co-doped $BaFe_2As_2$ [Inosov et al., 2009; Lester et al., 2010; Lumsden et al., 2009; Li et al., 2010; Nandi et al., 2010].

Our $BaFe_{2-x}Ni_xAs_2$ electron-doped samples were grown using self flux method as described before [Chen et al., 2011]. Since the electronic and superconducting properties of Co and Ni-doping of $BaFe_2As_2$ near optimal superconducting transition temperatures are almost identical [Bud'ko et al., 2009], we chose to study spin excitations in optimally doped $BaFe_{1.9}Ni_{0.1}As_2$ with $T_c = 20$ K.

4.2 Experimental Results

Our experiments were carried out on the MERLIN time-of-flight chopper spectrometer at the Rutherford-Appleton Laboratory, UK [Bewley et al., 2006]. We co-aligned 28 g of single crystals of $BaFe_{1.9}Ni_{0.1}As_2$ (with in-plane mosaic of 2.5° and out-of-plane mosaic of 4°). The incident beam energies were $E_i = 20, 25, 30, 80, 250, 450, 600$ meV, and mostly with E_i parallel to the c-axis. To facilitate easy comparison with spin

waves in $BaFe_2As_2$ [Harriger et al., 2011], we defined the wave vector Q at (q_x, q_y, q_z) as $(H, K, L) = (q_x a/2\pi, q_y b/2\pi, q_z c/2\pi)$ reciprocal lattice units (rlu) using the orthorhombic unit cell, where $a = b = 5.564$ Å, and $c = 12.77$ Å. The data are normalized to absolute units using a vanadium standard [Harriger et al., 2011], which may have a systematic error up to 20% due to differences in neutron illumination of vanadium and sample, and time-of-flight instruments.

Figure 1 and figure 2 summarize the key findings for the electron-doped iron arsenide superconductor $BaFe_{1.9}Ni_{0.1}As_2$ and the comparison with the spin waves in $BaFe_2As_2$. The data points in Figs. 1c and 1d show the dispersion of spin excitations for optimal doped $BaFe_{1.9}Ni_{0.1}As_2$ along $[1, K]$ and $[H, 0]$, and the solid lines show the fit of $BaFe_2As_2$ spin waves to an effective Heisenberg $J_{1a} - J_{1b} - J_2$ model with $J_{1a} \neq J_{1b}$ [Harriger et al., 2011]. Figure 2 shows the local dynamic susceptibility per formula unit (f.u.), which contains two Fe(Ni) atoms, in absolute units, defined as $\chi''(\omega) = \int \chi''(\mathbf{q}, \omega) d\mathbf{q} / \int d\mathbf{q}$ [Lester et al., 2010], where $\chi''(\mathbf{q}, \omega) = (1/3) tr(\chi''_{\alpha\beta}(\mathbf{q}, \omega))$, at different energies for $BaFe_2As_2$ and $BaFe_{1.9}Ni_{0.1}As_2$. It is clear that electron doping on $BaFe_2As_2$ only affects the low-energy spin excitations by broadening the spin waves below 80 meV, but has no impact on spin waves above 100 meV (see supplementary information). The quasiparticles that form within the spin-density-wave gap are sensitive to the Fermi surface change upon doping $BaFe_2As_2$, and hence the resulting low energy itinerant spin excitations substantially change, while the higher energy spin excitations are hardly affected.

Constant-Energy/wave vector (Q) dependence of the spin excitations and dynamic spin-spin correlation lengths for $BaFe_{1.9}Ni_{0.1}As_2$ and $BaFe_2As_2$. (a)-(d) Constant-Q cuts at $Q = (1, 0.05), (1, 0.2), (1, 0.35)$, and $(1, 0.5)$, respectively, at $T = 5$ (solid red circles) and 150 K (yellow filled circles) with background at $Q = (2, 0)$ subtracted. The negative scattering in the data are due to over subtraction of the phonon background. The solid lines are identical cuts from spin waves in $BaFe_2As_2$. For excitations below 100 meV, the intensity of the scattering of $BaFe_{1.9}Ni_{0.1}As_2$ is suppressed compared to that of $BaFe_2As_2$. For energies above 100 meV, the magnetic scattering is virtually identical between the parent and superconductor.

To substantiate the key conclusions from the data and calculations presented in Figure 1 and Figure 2, we show in Figure 3 the two-dimensional constant-energy (E) images of spin excitations of $BaFe_{1.9}Ni_{0.1}As_2$ in the (H, K) scattering plane for several Brillouin zones at 5 K. In the undoped phase, spin waves in $BaFe_2As_2$ exhibits an anisotropy spin gap of $\Delta = 9.8$ meV [Matan et al., 2009]. On doping, the anisotropy spin gap disappears and spin excitations form transversely elongated ellipses that decrease in intensity with increasing energy [Lester et al., 2010; Li et al., 2010]. For energy transfers of $E = 10 \pm 3$ (Fig. 3a), 33 ± 3 (Fig. 3b), 43 ± 3 (Fig. 3c), 60 ± 10 (Fig. 3d), and 81 ± 10 meV (Fig. 3e), spin excitations are peaked at the AF wave vector $Q = (1, 0)$ in the center of the Brillouin zone shown as dashed square boxes. As the energy increases to $E = 113 \pm 10$ (Fig. 2f) and 135 ± 10 meV (Fig. 2g), spin excitations start to split along the K-direction and form a ring around the Γ point.

Finally, spin excitations near the zone boundary at $E = 157 \pm 10$ and 214 ± 10 meV form four blobs centered at $Q = (1, 1)$.

In order to determine the dispersion of spin excitations for $BaFe_{1.9}Ni_{0.1}As_2$, we cut through the two-dimensional images similar to Fig. 3 along the $[1, K]$ and $[H, 0]$ directions. Figures 4a-4f show constant-energy cuts along the $[1, K]$ direction for $E = 25\pm5$, 55 ± 5, 95 ± 10, 125 ± 10, 150 ± 10, and 210 ± 10 meV. The scattering becomes dispersive for spin excitation energies above 95 meV. Figures 4g-4i show similar constant-energy cuts along the $[H, 0]$ direction. The solid lines in the Figure show identical spin wave cuts for $BaFe_2As_2$ [Harriger et al., 2011]. Since both measurements were taken in absolute units, we can compare the impact of electron-doping on the spin waves in $BaFe_2As_2$. At $E = 25 \pm 5$ meV, spin excitations in superconducting $BaFe_{1.9}Ni_{0.1}As_2$ are considerably broader in momentum space and weaker in intensity than spin waves (Figs. 4a and 4g). Upon increasing the excitation energy to 55 ± 5 meV, the dispersive spin waves in $BaFe_2As_2$ become weaker and broader (Figs. 3b and 3h). For energies above 95 meV, spin excitations in $BaFe_{1.9}Ni_{0.1}As_2$ are almost indistinguishable from spin waves in $BaFe_2As_2$ in both the linewidths and intensity (Figs. 4c-4f, and 4i). Based on these constant-energy cuts, we show in Figs. 1c and 1d the comparison of spin excitation dispersions of $BaFe_{1.9}Ni_{0.1}As_2$ (filled circles and horizontal bars) with those of spin waves in $BaFe_2As_2$ (solid lines). Inspection of Figs. 1-4 reveals that electron-doping to $BaFe_2As_2$ only broadens and suppresses low energy spin excitations and has no influence for spin waves above 100 meV (see supplementary information).

To reveal further the effect of electron doping on spin waves of $BaFe_2As_2$, we show in Figures 5a-5d constant-Q cuts at different wave vectors along the $[1, K]$ direction for spin excitations in $BaFe_{1.9}Ni_{0.1}As_2$. Near the Brillouin zone center at $Q = (1, 0.05)$ and $(1, 0.2)$, well-defined spin excitations are observed near $E = 40$, and 60 meV as shown in Figs. 5a and 5b, respectively. The intensity of the scattering from the spin excitations in $BaFe_{1.9}Ni_{0.1}As_2$ is, however, much lower than that of $BaFe_2As_2$ shown as solid lines in the Figures. On increasing the wave vectors to $Q = (1, 0.35)$ and $(1, 0.5)$, the magnetic scattering peak near $E = 100$, and 120 meV, and are essentially indistinguishable from spin waves in $BaFe_2As_2$ as shown in Figs. 5c and 5d. Furthermore, spin excitations have virtually no temperature dependence between 5 K and 150 K (Fig. 5b).

Finally, we show in Figs. 5e and 5f temperature dependence of spin excitations at energies near the neutron spin resonance $E = 9$ meV [Chi et al., 2009; Wang et al., 2010] and at $E = 90 \pm 5$ meV, respectively. While the intensity of the resonance at $E = 9$ meV increases dramatically below T_c, consistent with earlier work [Wang et al., 2010; Chi et al., 2009], spin excitations at 90 ± 5 meV are identical on cooling from 150 K to 5 K. We note that high-energy spin waves in $BaFe_2As_2$ are also weakly temperature dependent [Harriger et al., 2011]. Figure 6 shows the energy dependence of the dynamic spin-spin correlation lengths, which are about $\xi \approx 14$ Å and excitation energy independent. For comparison, the dynamic spin-spin correlation length (the solid line in Fig. 6) in $BaFe_2As_2$ decreases with increasing energy and becomes similar to that of $BaFe_{1.9}Ni_{0.1}As_2$ for excitation energies above 100 meV. To further compare

spin excitations in $BaFe_2As_2$ and $BaFe_{1.9}Ni_{0.1}As_2$, we show in Figure 7 spin excitations of these two materials at different energies. Consistent with data shown in Figs. 2-6, we see that the effect of electron-doping is to mostly modify spin excitations below 80 meV.

4.3 Theoretical Calculation

Our theoretical method for computing the magnetic excitation spectrum employs abinitio full potential DFT+DMFT method, as implemented in Ref. [Haule et al., 2010], which is based on the commercial DFT code of Wien2k . The DMFT method requires solution of the generalized quantum impurity problem, which is here solved by the numerically exact continuous-time quantum Monte Carlo method (CTQMC) [Haule, 2007; Werner et al., 2006]. The Coulomb interaction matrix for electrons on iron atom was determined by the self-consistent GW method in Ref. [Kutepov et al., 2010], giving $U = 5\,\mathrm{eV}$ and $J = 0.8\,\mathrm{eV}$ for the local basis functions within the all electron approach employed in our DFT+DMFT method.

The dynamical magnetic susceptibility $\chi(\mathbf{q}, \omega)$ is computed from the *ab initio* perspective by extracting the two-particle vertex functions of DFT+DMFT solution Γ^{irr}_{loc}. The polarization bubble χ^0 is computed from the fully interacting one particle Greens function. The full susceptibility is computed from χ^0 and the two-particle irreducible vertex function Γ^{irr}_{loc}, which is assumed to be local in the same basis in

which the DMFT self-energy is local, implemented here by the projector to the muffin-tin sphere [Haule et al., 2010]. In order to extract Γ^{irr}_{loc}, we employ the Bethe-Salpeter equation (see Figure 8) which relates the local two-particle Green's function (χ_{loc}), sampled by CTQMC, with both the local polarization function (χ^0_{loc}) and Γ^{irr}_{loc}:

$$\Gamma^{irr}_{loc\,\substack{\alpha_1\sigma_1,\alpha_2\sigma_2\\ \alpha_3\sigma_3,\alpha_4\sigma_4}}(i\nu, i\nu')_{i\omega} = \frac{1}{T}[(\chi^0_{loc})^{-1}_{i\omega} - \chi^{-1}_{loc}]. \tag{4.1}$$

Γ^{irr}_{loc} depends on three Matsubara frequencies ($i\nu$, $i\nu'$; $i\omega$), and both the spin (σ_{1-4}) and the orbital (α_{1-4}) indices, which run over $3d$ states on the iron atom. T is the temperature.

Once the irreducible vertex Γ^{irr}_{loc} is obtained, the momentum dependent two-particle Green's function is constructed again using the Bethe-Salpeter equation (Figure 8) by replacing the local polarization function χ^0_{loc} by the non-local one $\chi^0_{\mathbf{q},i\omega}$:

$$\chi_{\substack{\alpha_1\sigma_1,\alpha_2\sigma_2\\ \alpha_3\sigma_3,\alpha_4\sigma_4}}(i\nu, i\nu')_{\mathbf{q},i\omega} = [(\chi^0)^{-1}_{\mathbf{q},i\omega} - T\cdot\Gamma^{irr}_{loc}]^{-1}. \tag{4.2}$$

Finally, the dynamic magnetic susceptibility $\chi(\mathbf{q}, i\omega)$ is obtained by closing the two particle green's function with the magnetic moment $\mu = \mu_B(\mathbf{L} + 2\mathbf{S})$ vertex, and summing over all internal degrees of freedom, i.e., orbitals (α_{1-4}), spins (σ_{1-4}) and frequencies ($i\nu$,$i\nu'$), on the four external legs

$$\chi(\mathbf{q}, i\omega) = T\sum_{i\nu,i\nu'}\sum_{\substack{\alpha_1\alpha_2\\ \alpha_3\alpha_4}}\sum_{\substack{\sigma_1\sigma_2\\ \sigma_3\sigma_4}} \mu^z_{\substack{\alpha_1\sigma_1\\ \alpha_3\sigma_3}}\mu^z_{\substack{\alpha_2\sigma_2\\ \alpha_4\sigma_4}}\ \chi_{\substack{\alpha_1\sigma_1,\alpha_2\sigma_2\\ \alpha_3\sigma_3,\alpha_4\sigma_4}}(i\nu, i\nu')_{\mathbf{q},i\omega} \tag{4.3}$$

We note that the same abinitio methodology which is here used to compute the magnetic excitation spectra, was previously shown to describe the photoemission, the optical spectra and the magnetic moments of this material [Yin et al., 2011] in excellent agreement with experiment.

To check if spin excitations in the AF $BaFe_2As_2$ and superconducting $BaFe_{1.9}Ni_{0.1}As_2$ can be understood in an itinerant picture, we calculate the local susceptibility $\chi''(\omega)$ using the random phase approximation (RPA) based on realistic Fermi surfaces and band structures [Park et al., 2011]. Within RPA, the polarization bubble χ^0 is computed from the density function theory (DFT) Kohn-Sham Green's functions while the irreducible vertex Γ^{irr} is approximated by the screened Coulomb parameters $\widetilde{U}$ and $\widetilde{J}$. Using $\widetilde{U} = 1.3\,\mathrm{eV}$ and $\widetilde{J} = 0.4\,\mathrm{eV}$ and performing calculations above T_N [Park et al., 2011], we find that the RPA estimated $\chi''(\omega)$ for $BaFe_2As_2$ and $BaFe_{1.9}Ni_{0.1}As_2$ (solid and dashed lines in Fig. 1b) increases approximately linearly with energy and has absolute values about a factor of three smaller than the observation (Fig. 2). Although the RPA calculation depends on Coulomb parameters used, we note that the 5-orbital Hubbard model calculation using $\widetilde{U} = 0.8\,\mathrm{eV}$ and $\widetilde{J} = 0.2\,\mathrm{eV}$ produces essentially similar local magnetic spectra [Graser et al., 2010]. Therefore, a pure RPA type itinerant model underestimates the absolute spectral weight of the magnetic excitations in iron pnictides.

The solid blue and red lines in Fig. 1b show the calculated local susceptibility using a combined DFT and DMFT in the paramagnetic state. Within DFT+DMFT, $\chi''(\mathbf{q}, \omega)$ is computed by the Bethe-Salpeter equation using the polarization function

χ^0 and the two-particle local irreducible vertex function Γ^{irr} [Park et al., 2011]. χ^0 is computed from the interacting one-particle Green's function determined by the charge self-consistent full potential DFT+DMFT method and Γ^{irr} is extracted from the two particle vertex function of the auxiliary impurity problem. The latter is defined by the DMFT procedure using projection of all electronic states to the d character within the iron muffin-tin sphere. By comparing DFT+DMFT and RPA calculations in Fig. 1b with data in Fig. 2, we see that the former is much closer to the observation. Note that the calculation is done in the paramagnetic state, hence the low energy modifications of the spectra due to the long range AF order is not captured in this calculation. RPA can describe only the itinerant part of the electron spectra, while DFT+DMFT captures the essential aspects of both the quasiparticles and the iron local moments formed by strong Hunds coupling (see supplementary information for more detailed discussion). The improved agreement of DFT+DMFT thus suggest that both the quasiparticles and the local moment aspects of the iron electrons are needed to obtain the correct intensity and energy distribution of neutron scattering spectra [Park et al., 2011].

One way to quantitatively compare spin excitations in iron pnictides with those in copper oxides is to estimate their total fluctuating moments, defined as $\langle m^2 \rangle = (3\hbar/\pi) \int \chi''(\omega) d\omega / (1 - \exp(-\hbar\omega/kT))$ [Lester et al., 2010]. Based on Fig. 1e, we find that $\langle m^2 \rangle = 3.17 \pm 0.16$ and $3.2 \pm 0.16\ \mu_B^2$ per Fe(Ni) for $BaFe_2As_2$ and $BaFe_{1.9}Ni_{0.1}As_2$, respectively. Using the formula for magnetic moment of a spin $\langle m^2 \rangle = (g\mu_B)^2 S(S+1)$ (where $g = 2$) [Lorenzana et al., 2005], we find an effective iron spin S of about

1/2, similar to that of $CaFe_2As_2$ [Zhao et al., 2009]. These results also show that superconductivity in electron-doped system hardly changes the total size of the fluctuating moment. In the fully localized (insulating) case, the formal Fe^{2+} oxidation state in $BaFe_2As_2$ would give a $3d^6$ electronic configuration. Hund's rules would yield $S = 2$ and $\langle m^2 \rangle = 24\ \mu_B^2$ per Fe. This is considerable more than the observed values suggesting that significant hybridization of Fe $3d$ with pnictide p orbitals and among themselves, which leads to a metallic state where the Hund's coupling is less important than in the atomic limit [Cvetkovic and Tesanovic, 2009]. For comparison, we note that $\langle m^2 \rangle > 1.9\ \mu_B^2$ per Cu for the AF insulating La_2CuO_4 measured over a similar energy range [Headings et al., 2010; Hayden et al., 1996]. From Fig. 1e, we see that the large fluctuating moment $\langle m^2 \rangle$ in iron pnictides arises mostly from high-energy spin excitations that is essentially temperature [Harriger et al., 2011] and electron-doping independent within the errors of our measurements (Fig. 1). Since there are currently no high-energy spin excitation data in absolute units for optimally hole-doped $Ba_{0.67}K_{0.33}Fe_2As_2$ [Zhang, 2011], it is unclear how hole-doping $BaFe_2As_2$ modifies the spin-wave spectra.

The DFT+DMFT calculation suggests that both the band structure and the local moment aspects (e.g. Hunds coupling) of the iron electrons are needed to obtain a good description of the magnetic response in $BaFe_2As_2$ and $BaFe_{1.9}Ni_{0.1}As_2$. The weak electron-doping dependence of the fluctuating moment is consistent with the Hund's metal picture, where electron filling associated with the Fe $3d^6$ electrons by Ni-doping is not expected to drastically affect the local moments. What is surprising is that

the similarities in the local susceptibilities of the iron pnictides studied here and the parents of the cuprate superconductors. The large fluctuating moment, arising from Hund's rule coupling, and concentrated at higher energy in iron pnictides, nevertheless gives an imprint on the massive and anisotropic low-energy quasiparticles [Yin et al., 2011], which form Cooper pairs at low energy. This physics is different from the physics of doped charge transfer insulators appropriate for copper oxides [Lee and Wen, 2006], hence the electron correlations in iron pnictides and copper oxides have different microscopic origins, although they are important for understanding the magnetism and superconductivity for both materials.

4.4 Conlusion

By comparing spin excitations in $BaFe_{1.9}Ni_{0.1}As_2$ and $BaFe_2As_2$ throughout the Brillouin zone, we were able to probe how electron-doping and superconductivity affect the overall spin excitations spectra. We demonstrate that while the low-energy spin excitations are affected, the high-energy excitations show a very weak temperature and doping dependence. Comparison of our results with various theories suggests that neither a fully itinerant nor a localized picture explains the magnetic excitation spectrum. However, a combination of density functional theory (DFT) and dynamic mean field theory (DMFT) provides a natural way to improve on both these pictures.

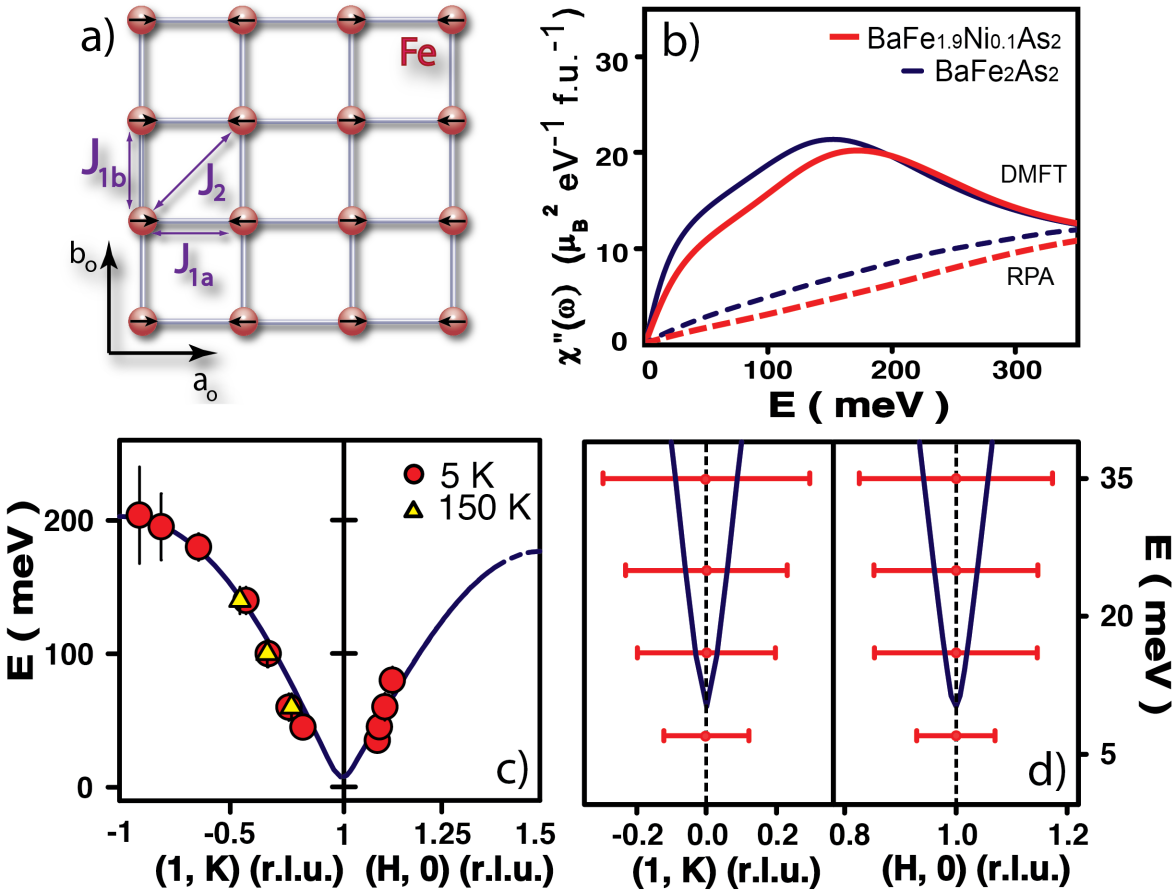

Figure 4.1: (a) AF spin structure of $BaFe_2As_2$ with Fe spin ordering. The effective magnetic exchange couplings along different directions are depicted. (b) RPA and LDA+DMFT calculations of $\chi''(\omega)$ in absolute units for $BaFe_2As_2$ and $BaFe_{1.9}Ni_{0.1}As_2$. (c) The solid lines show spin awave dispersions of $BaFe_2As_2$ for $J_{1a} \neq J_{1b}$ along the $[1, K]$ and $[H, 0]$ directions obtained in Ref. [Harriger et al., 2011]. The filled circles and upper triangles are spin excitation dispersions of $BaFe_{1.9}Ni_{0.1}As_2$ at 5 K and 150 K, respectively. (d) The solid line shows low energy spin waves of $BaFe_2As_2$. The horizontal bars show the full-width-half-maximum of spin excitations in $BaFe_{1.9}Ni_{0.1}As_2$.

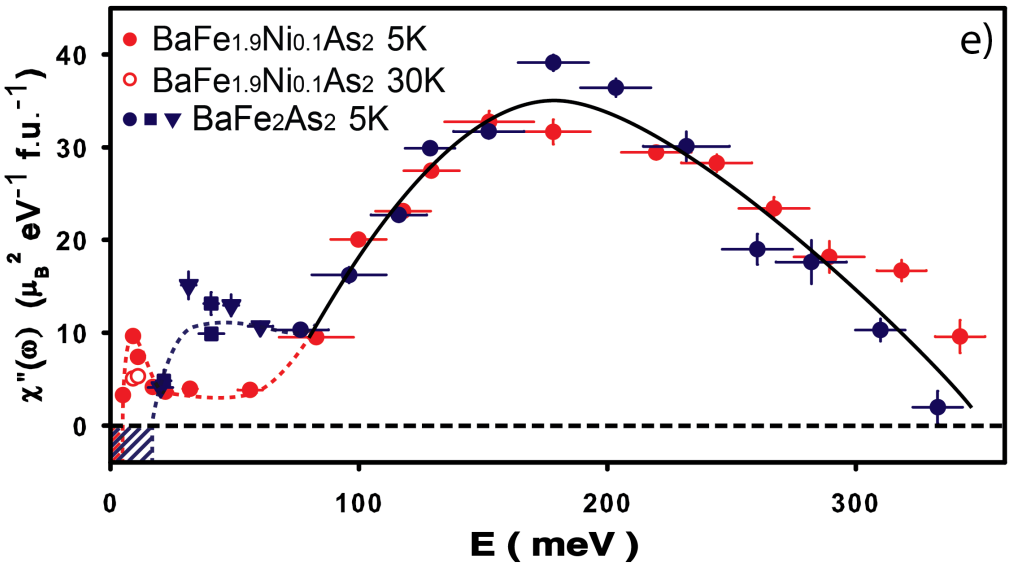

Figure 4.2: Energy dependence of $\chi''(\omega)$ for $BaFe_2As_2$ (filled blue circles) and $BaFe_{1.9}Ni_{0.1}As_2$ below (filled red circles) and above (open red circles) T_c. The solid and dashed lines are guide to the line. The vertical error bars indicate the statistical errors of one standard deviation. The horizontal error bars in (e) indicate energy integration range.

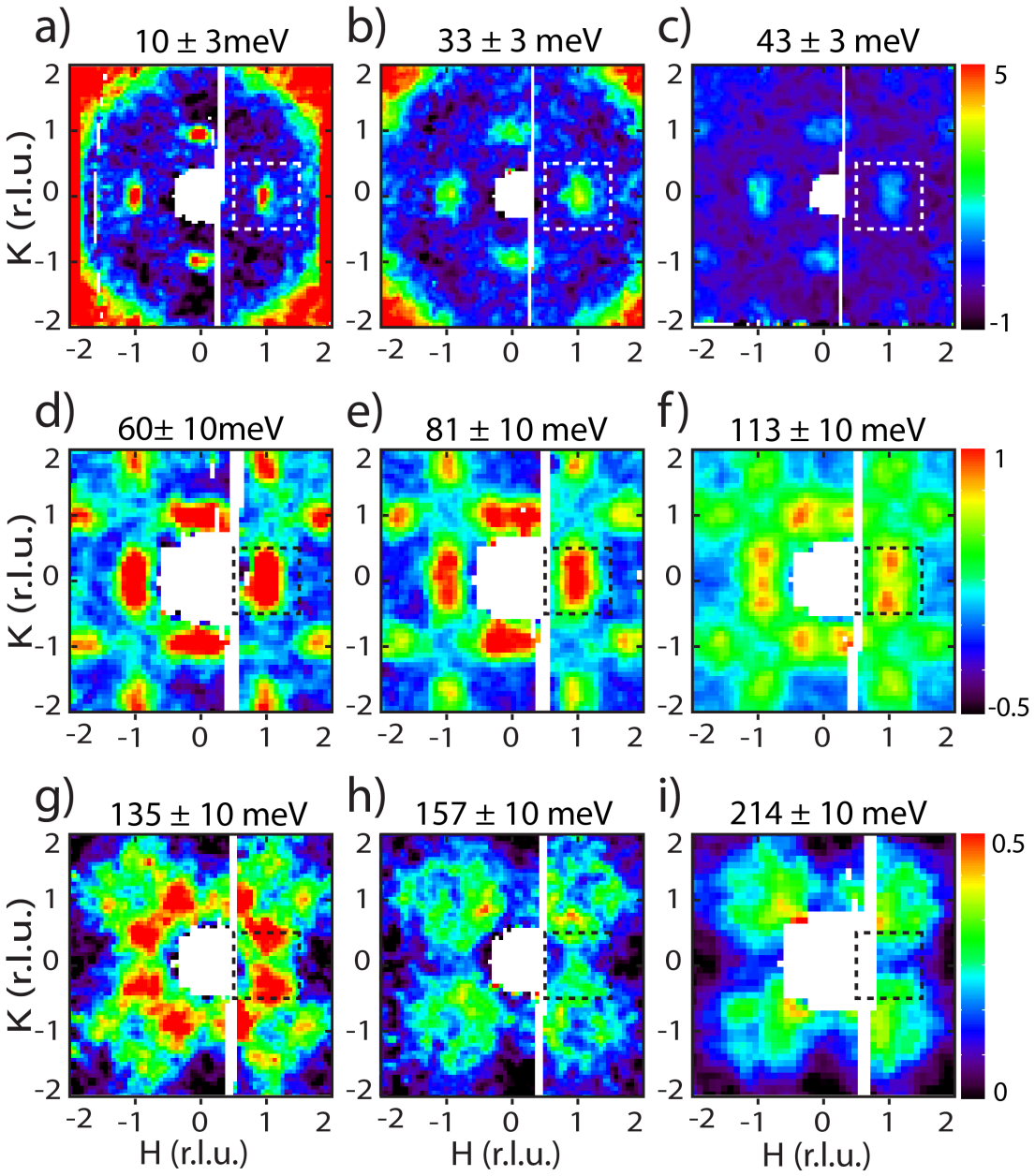

Figure 4.3: Constant-energy slices through the magnetic excitations of $BaFe_{1.9}Ni_{0.1}As_2$ at different energies in several Brillouin zones. The images were obtained after subtracting the background integrated from $1.8 < H < 2.2$ and $-0.2 < K < 0.2$. The color bars represent the vanadium normalized absolute spin excitation intensity in the units of mbarn/sr/meV/f.u and the dashed boxes indicate AF zone boundaries for a single FeAs layer. Two dimensional images of spin excitations at (a) $E = 10 \pm 3$, (b) 33 ± 3, (c) 43 ± 3, (d) 60 ± 10, (e) 81 ± 10, (f) 113 ± 10, (g) 135 ± 10, (h) 157 ± 10, and (i) 214 ± 10 meV.

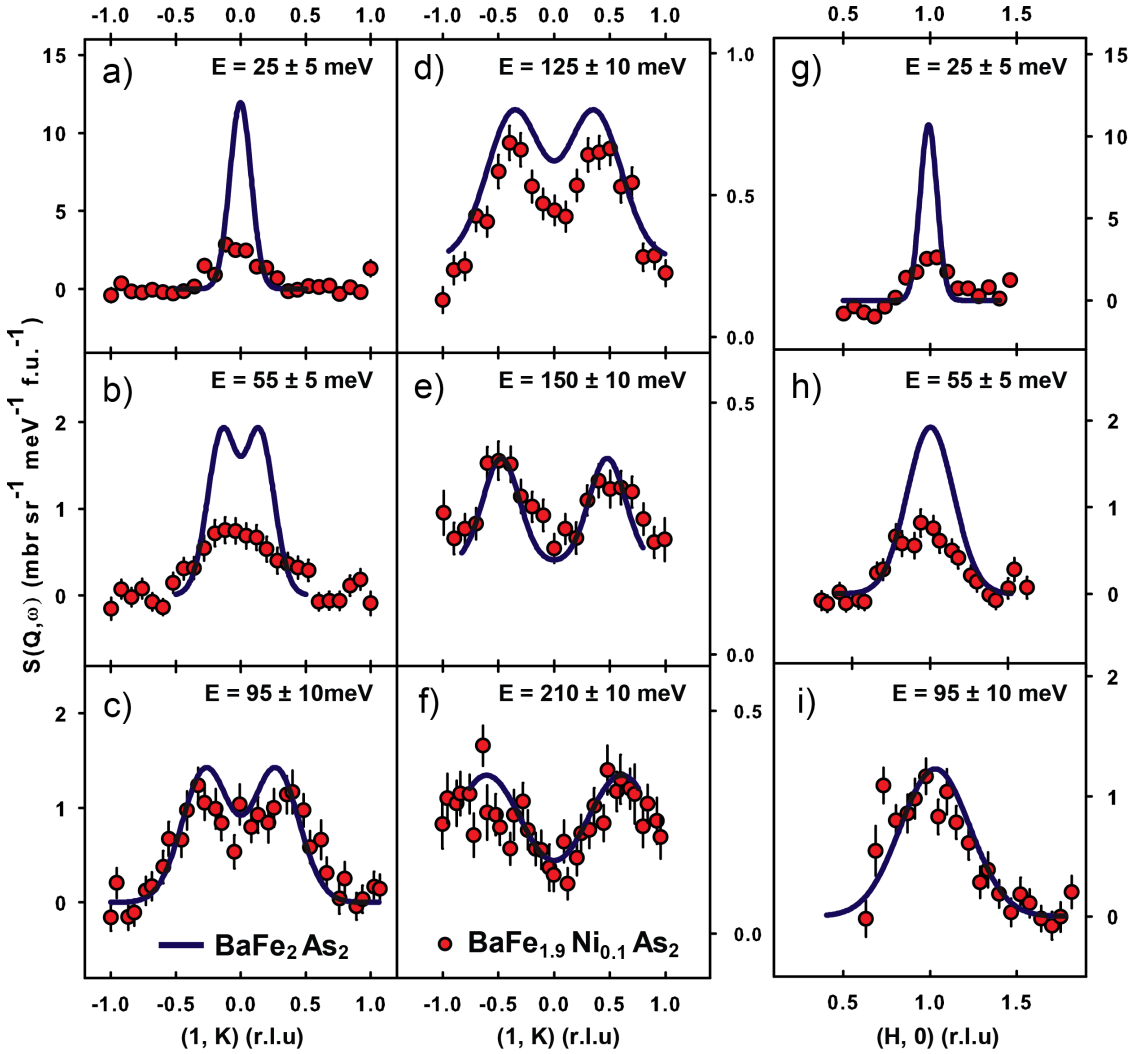

Figure 4.4: Constant-energy cuts of the spin excitation dispersion as a function of increasing energy along the $[1, K]$ and $[H, 0]$ directions for $BaFe_{1.9}Ni_{0.1}As_2$. The solid lines show identical cuts for spin waves of $BaFe_2As_2$ in absolute units. (a) Constant-energy cut along the $[1, K]$ direction at $E = 25 \pm 5$, (b) 55 ± 5, (c) 95 ± 10, (d) 125 ± 10, (e) 150 ± 10, and (f) 210 ± 10 meV. (g) Constant-energy cut along the $[H, 0]$ direction at $E = 25 \pm 5$, (h) 55 ± 5, and 95 ± 10 meV. The error bars indicate the statistical errors of one standard deviation.

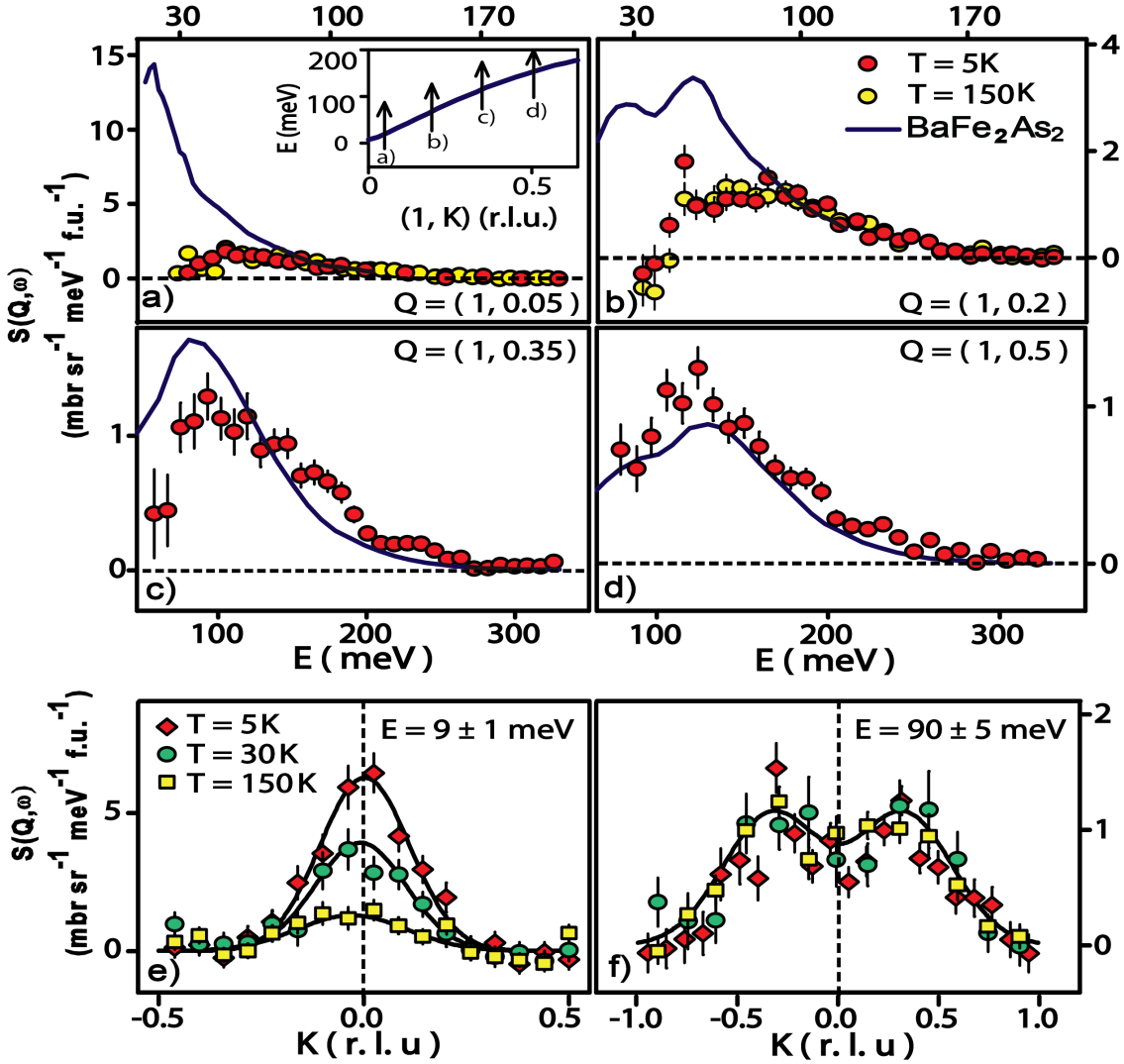

Figure 4.5: (e) Constant-energy cuts at the neutron spin resonance energy of $E = 9 \pm 1$ meV [Chi et al., 2009] below and above T_c. The solid lines are Gaussian fits on linear backgrounds. (f) Temperature dependence of spin excitations at $E = 90 \pm 5$ meV. (g) Energy dependence of the dynamic spin-spin correlation lengths (ξ) at 5 K obtained by Fourier transform of constant-energy cuts similar to those in Fig. 3a-f and Fig. 4e,f.

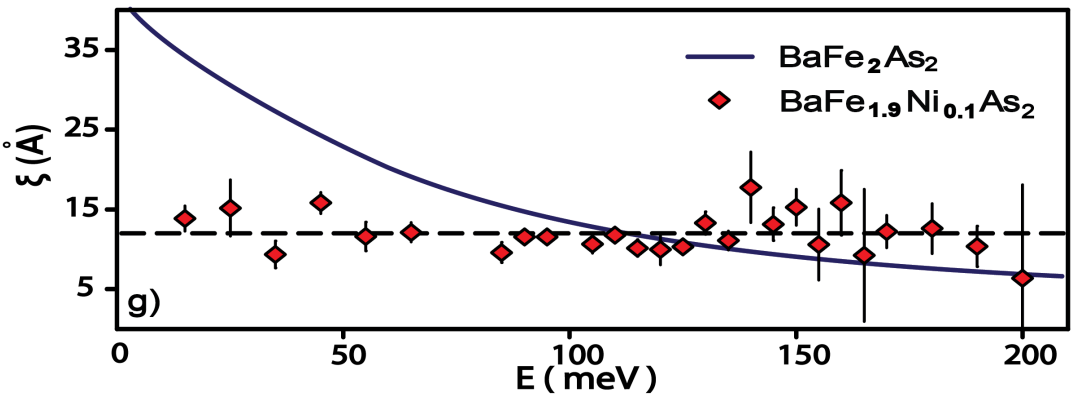

Figure 4.6: For all excitation energies probed ($10 \leq E \leq 200$ meV), the dynamic spin-spin correlation lengths are independent of energy. The solid line shows energy dependence of ξ for $BaFe_2As_2$. The error bars indicate the statistical errors of one standard deviation.

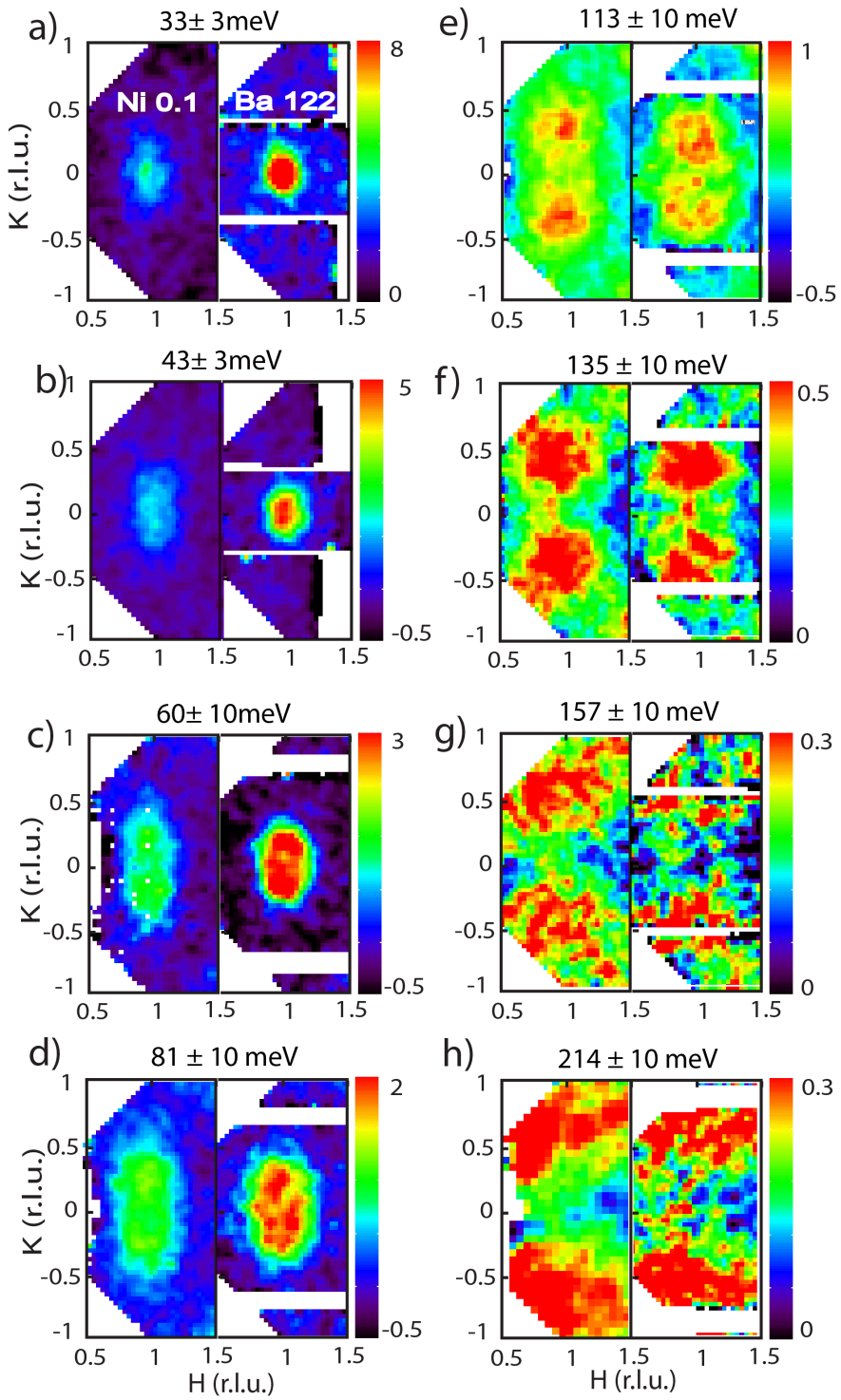

Figure 4.7: Constant-energy images of the spin excitations as a function of increasing energy for $BaFe_{1.9}Ni_{0.1}As_2$ and $BaFe_2As_2$ in units of mbarns/sr/meV/f.u. (a) $E = 33 \pm 3$, (b) 43 ± 3, (c) 60 ± 10, (d) 81 ± 10, (e) 113 ± 10, (f) 135 ± 10, (g) 157 ± 10, and (h) 214 ± 10 meV.

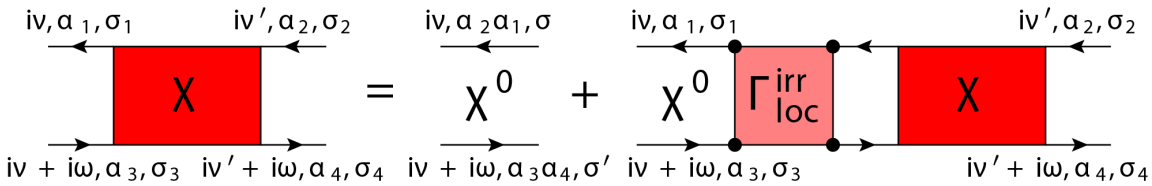

Figure 4.8: The Feynman diagrams for the Bethe-Salpeter equation. It relates the two-particle Green's function (χ) with the polarization (χ^0) and the local irreducible vertex function (Γ^{irr}_{loc}). The non-local two-particle Green's function is obtained by replacing the local propagator by the non-local propagator.

Chapter 5

Magnetic Excitations in Overdoped $BaFe_{1.85}Ni_{0.15}As_2$

We use polarized inelastic neutron scattering to study low-energy spin excitations and their spatial anisotropy in electron-overdoped superconducting $BaFe_{1.85}Ni_{0.15}As_2$ ($T_c = 14$ K). In the normal state, the imaginary part of the dynamic susceptibility, $\chi''(Q, \omega)$, at the antiferromagnetic (AF) wave vector $Q = (0.5, 0.5, 1)$ increases linearly with energy for $E \leq 13$ meV. Upon entering the superconducting state, a spin gap opens below $E \approx 3$ meV and a broad neutron spin resonance appears at $E \approx 7$ meV. Our careful neutron polarization analysis reveals that $\chi''(Q, \omega)$ is isotropic for the in-plane and out-of-plane components in both the normal and superconducting states. A comparison of these results with those of undoped $BaFe_2As_2$ and optimally electron-doped $BaFe_{1.9}Ni_{0.1}As_2$ ($T_c = 20$ K) suggests that the spin anisotropy observed in $BaFe_{1.9}Ni_{0.1}As_2$ is likely due to its proximity to the undoped $BaFe_2As_2$. Therefore,

the neutron spin resonance is isotropic in the overdoped regime, consistent with a singlet to triplet excitation.

5.1 Introduction

Understanding the role of spin excitations in the superconductivity of iron arsenides [Kamihara et al., 2008; Rotter et al., 2008; Li et al., 2009a] is important for developing a microscopic theory of superconductivity in these materials [Mazin et al., 2008; Korshunov and Eremin, 2008; Maier et al., 2009; Maier and Scalapino, 2008; Seo et al., 2009]. Like copper oxide superconductors, superconductivity in iron pnictides arises when electrons or holes are doped into their antiferromagnetically-ordered parent compounds [de la Cruz et al., 2008a]. For electron-doped $BaFe_{2-x}T_xAs_2$ (T =Co, Ni) [Li et al., 2009a], the antiferromagnetic (AF) and superconducting phase diagrams as a function of Co(Ni)-doping have been determined by neutron scattering experiments (Figure 1) [Lester et al., 2009; Luo et al., 2012b]. Near the optimally electron-doped superconductor $BaFe_{2-x}Ni_xAs_2$ at $x = 0.1$ ($T_c = 20$ K), the static AF order is suppressed [Chi et al., 2009]. However, short-range spin excitations persist and couple directly to superconductivity via a collective magnetic excitation termed the neutron spin resonance [Chi et al., 2009; Lumsden et al., 2009; Li et al., 2009b; Inosov et al., 2009; Wang et al., 2010; Park et al., 2010]. As a function of Ni-doping, the energy of the resonance is associated with both the superconducting electronic gap Δ and k_BT_c, thus indicating its direct connection with superconductivity [Inosov et al., 2009].

Although the resonance appears to be a common feature amongst different classes of unconventional superconductors including high-T_c copper oxides [Rossat-Mignod et al., 1991; Mook et al., 1993; Fong et al., 1996; Dai et al., 2001; Wilson et al., 2006c], heavy Fermions [Metoki et al., 1998; Stock et al., 2008], and iron-based materials [Chi et al., 2009; Lumsden et al., 2009; Li et al., 2009b; Inosov et al., 2009; Wang et al., 2010; Park et al., 2010; Mook et al., 2010; Qiu et al., 2009; Tanatar et al., 2012], much remains unknown about its microscopic origin. Assuming that the resonance is a spin-1 singlet-to-triplet excitation of the Cooper pairs [Eschrig, 2006], it should be possible to split it into three peaks under the influence of a magnetic field via the Zeeman effect by an amount $\Delta E = \pm g\mu_B B$, where $g = 2$ is the Lande factor and B is the magnitude of the field [Dai et al., 2000; Wen et al., 2010; Li et al., 2011; Stock et al., 2012]. Although there have been attempts to split the resonance for copper oxide [Dai et al., 2000] and iron-based superconductors [Wen et al., 2010; Li et al., 2011] in this way, the results are inconclusive and it has not been possible determine if the mode is indeed a singlet-to-triplet excitation. In a very recent neutron experiment performed on the heavy Fermion superconductor $CeCoIn_5$, the resonance was shown to be a doublet excitation [Stock et al., 2012], thus casting doubt on its direct connection with superconducting Cooper pairs [Zhao et al., 2010].

Alternatively, one can use neutron polarization analysis to determine the nature of the resonance and the effect of superconductivity on spin excitations. If the resonance is an isotropic triplet excitation of the singlet superconducting ground state, one expects that the degenerate triplet would be isotropic in space. Utilizing

neutron polarization analysis, one can conclusively separate the magnetic signal from lattice scattering and determine the spatial anisotropy of the magnetic excitations [Moon et al., 1969]. For the optimally hole-doped copper oxide superconductor $YBa_2Cu_3O_{6.9}$ [Rossat-Mignod et al., 1991; Mook et al., 1993; Fong et al., 1996; Dai et al., 2001], recent polarized neutron scattering experiments reveal that while the resonance at $E = 41$ meV is isotropic in space, magnetic excitations below the resonance ($10 \leq E \leq 30$ meV) exhibit large anisotropy with the excitations polarized along the c-axis being suppressed [Headings et al., 2011]. These results suggest that while the resonance itself is consistent with a spin-1 singlet-to-triplet excitation. In the case of iron-based superconductors, the situation is more complicated. For optimally electron-doped $BaFe_{1.9}Ni_{0.1}As_2$, polarized neutron scattering experiments indicate that while the magnetic scattering is essentially isotropic in the normal state, a large spin anisotropy develops below T_c. Excitations polarized along the c-axis are larger than those in the plane for energies $2 \leq E \leq 6$ meV, i.e. below the weakly anisotropic resonance [Lipscombe et al., 2010]. On the other hand, similar measurements on superconducting $FeSe_{0.5}Te_{0.5}$ reveal an anisotropic resonance with the in-plane component slightly larger than the out-of-plane component [Babkevich et al., 2011]. However, the spin excitations are isotropic for energies below and above the resonance [Babkevich et al., 2011]. Finally, recent neutron polarization analysis of spin waves in the undoped AF $BaFe_2As_2$ [Qureshi et al., 2012] indicate that the magnetic single-ion anisotropy induced spin-wave gaps [Zhao et al., 2008b; Matan et al., 2009] are strongly anisotropic, with the in-plane component of the spin-wave

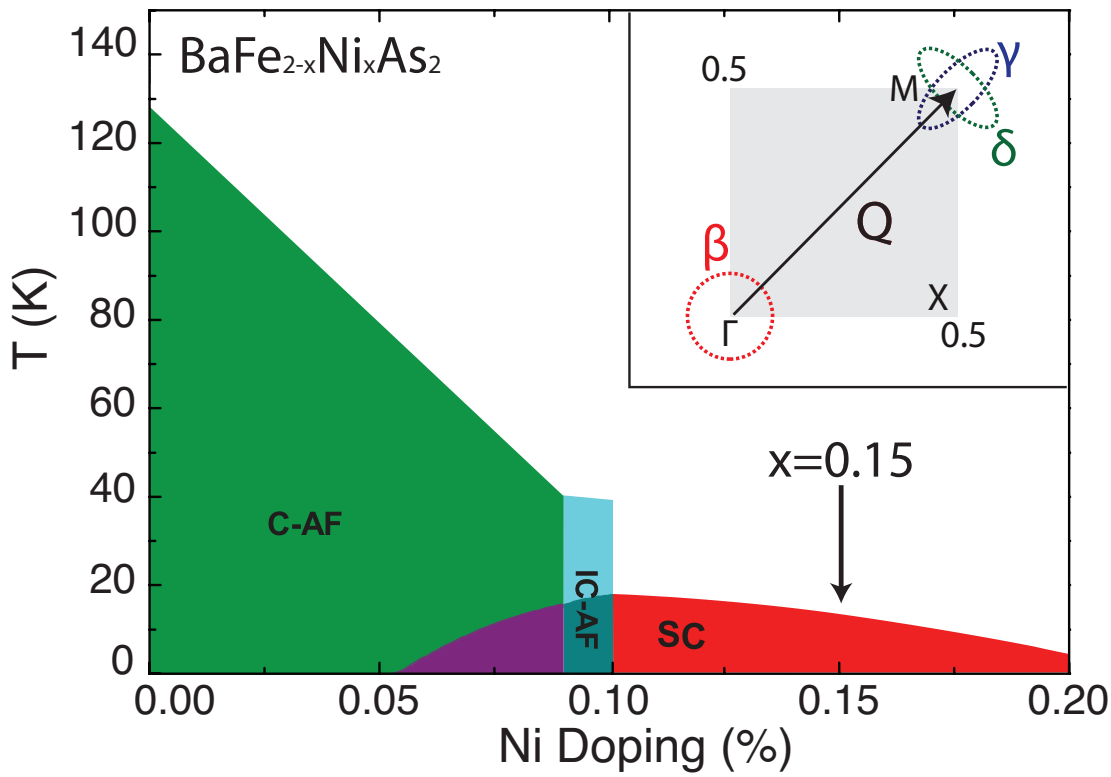

Figure 5.1: (Color online) (a) The schematic antiferromagnetic and superconducting phase diagram of $BaFe_{2-x}Ni_xAs_2$ as determined from neutron diffraction experiments [Luo et al., 2012b]. The present composition is highlighted with an arrow. The inset shows an illustration of quasiparticle excitations from the hole Fermi pocket at the Γ point to the electron pocket at the M point as predicted by Fermi surface nesting theories. (b) The three neutron polarization directions (x, y and z) oriented in the (H, H, L) plane of the reciprocal space.

gap much larger than that of the c-axis component. Therefore, it costs more energy to rotate a spin within the orthorhombic a-b plane than rotating it perpendicular to the FeAs layers in the AF ordered state of $BaFe_2As_2$ [Qureshi et al., 2012].

Given the current confusing experimental situation on the anisotropy of spin excitations in undoped and optimally electron-doped $BaFe_{2-x}Ni_xAs_2$ [Lipscombe et al., 2010; Qureshi et al., 2012], it would be interesting to carry out similar polarized neutron scattering measurements for electron overdoped $BaFe_{2-x}Ni_xAs_2$.

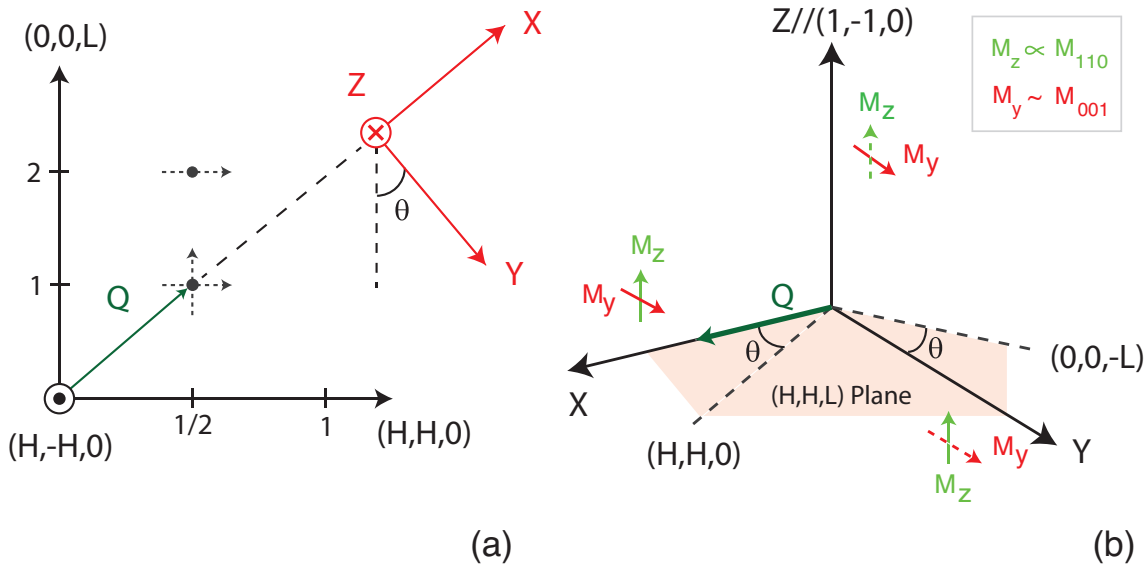

Figure 5.2: The relationship between magnetic components M_y and M_z measured by polarized neutron scattering and in-plane (M_{110}) and out-of-plane (M_{001}) dynamic spin susceptibility. The solid arrow denotes the measured magnetic component in a SF channel and the dashed arrow denotes the component measured in a NSF channel. In this geometry, we have $M_z \propto M_{1\bar{1}0} = M_{110}$, due to tetragonal symmetry; and $M_y \sim M_{001}$, given that θ is a small value.

From the electronic phase diagram of $BaFe_{2-x}Ni_xAs_2$ in Figure1 [Luo et al., 2012b], we see that samples in the overdoped regime are far from the AF and superconductivity co-existence region, and thus avoid possible influence of the local magnetic anisotropy present in undoped $BaFe_2As_2$ [Qureshi et al., 2012]. For our neutron experiments, we prepared over-doped $BaFe_{1.85}Ni_{0.15}As_2$ with $T_c = 14$ K (Fig. 1(a)). In this article, we describe polarized neutron scattering studies of energy and momentum dependence of the magnetic excitations in $BaFe_{1.85}Ni_{0.15}As_2$ below and above T_c. We find that the spin excitations at or near the resonance energy are spatially isotropic. By comparing these results with previous work on undoped $BaFe_2As_2$ and optimally doped $BaFe_{1.9}Ni_{0.1}As_2$ [Lipscombe et al., 2010; Qureshi et al., 2012], we conclude that the strong in-plane single-ion anisotropy in antiferromagnetically-ordered orthorhombic $BaFe_2As_2$ extends to the paramagnetic tetragonal $BaFe_{1.9}Ni_{0.1}As_2$, giving rise to the large out-of-plane component of the low-energy spin excitations for the superconducting $BaFe_{1.9}Ni_{0.1}As_2$. Therefore, the resonance in optimally and overdoped $BaFe_{2-x}Ni_xAs_2$ ($x = 0.1, 0.15$) is mostly isotropic in space, consistent with the singlet-to-triplet excitation scenario.

5.2 Experimental Details

We grew large single crystals of the overdoped iron arsenide superconductor $BaFe_{1.85}Ni_{0.15}As_2$ using a self-flux method [Chen et al., 2011]. $BaFe_{1.85}Ni_{0.15}As_2$ has a T_c of 14 K, and is far away from the AF phase of the undoped $BaFe_2As_2$ (Figure 1). As a function

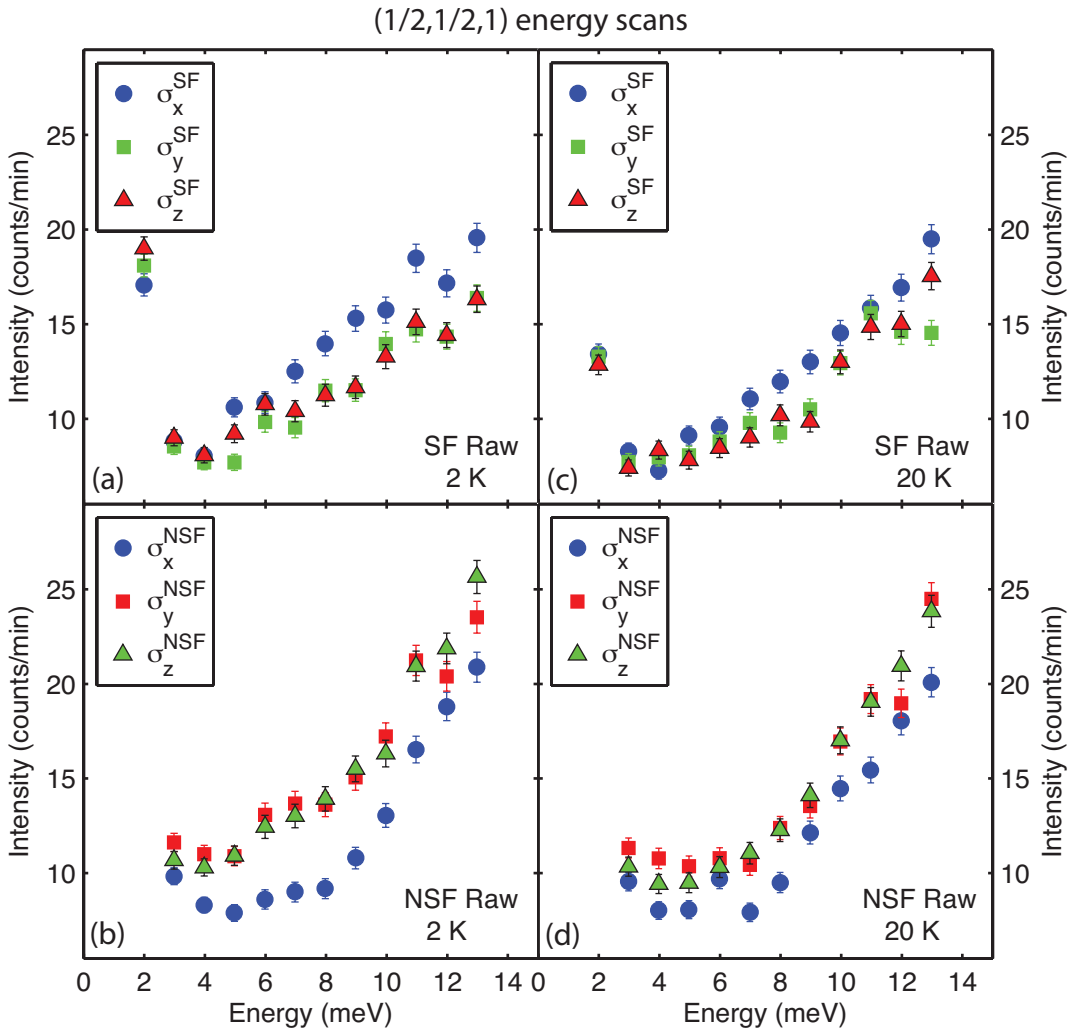

Figure 5.3: (Color online) Constant-Q scans at $\mathbf{Q} = (0.5, 0.5, 1)$ below and above T_c. Using polarized neutrons, we can measure six independent scattering cross sections: incoming neutrons polarized along the x, y or z directions, with outgoing neutrons flipped (SF), or not flipped (NSF). (a) The raw data for SF scattering at 2 K, denoted as $\sigma^{\mathrm{SF}}_{x,y,z}$; (b) Identical scans in NSF channel, or $\sigma^{\mathrm{NSF}}_{x,y,z}$; (c) SF scattering $\sigma^{\mathrm{SF}}_{x,y,z}$ at 20 K, and (d) NSF scattering $\sigma^{\mathrm{NSF}}_{x,y,z}$ at 20 K.

of increasing Ni-doping x, the low-temperature crystal structure of $BaFe_{2-x}Ni_xAs_2$ changes from orthorhombic to tetragonal with $a = b$ for $x \geq 0.1$ [Luo et al., 2012b; Chi et al., 2009]. For this experiment, we coaligned ~ 15 g single crystals of $BaFe_{1.85}Ni_{0.15}As_2$ in the (H, H, L) scattering plane (with mosaicity 3° at full width half maximum) with a tetragonal unit cell for which $a = b = 3.96$ Å, and $c = 12.77$ Å. In this notation, the vector $\mathbf{Q}$ in three-dimensional reciprocal space in Å^{-1} is defined as $\mathbf{Q} = H\mathbf{a}^* + K\mathbf{b}^* + L\mathbf{c}^*$, where H, K, and L are Miller indices and $\mathbf{a}^* = \hat{\mathbf{a}}2\pi/a, \mathbf{b}^* = \hat{\mathbf{b}}2\pi/b, \mathbf{c}^* = \hat{\mathbf{c}}2\pi/c$ are reciprocal lattice vectors.

We carried out polarized inelastic neutron scattering experiments at the IN20 triple-axis spectrometer at the Institut Laue-Langevin in Grenoble, France. We used the Cryopad capability of the IN20 spectrometer in order to ensure that the sample was in a strictly zero magnetic field environment. This avoids errors due to flux inclusion and field expulsion in the superconducting phase of the sample. Polarized neutrons were produced using a focusing Heusler monochromator and analyzed using a focusing Heusler analyzer with a fixed final wave vector at $k_f = 2.662$Å^{-1}. To facilitate easy comparison with previous polarized neutron scattering results [Lipscombe et al., 2010], we define neutron polarization directions as x, y, z, with x parallel to $\mathbf{Q}$ and y and z both perpendicular to $\mathbf{Q}$ as shown in Figure 2(a). Since neutron scattering is only sensitive to those magnetic scattering components perpendicular to the momentum transfer $\mathbf{Q}$, magnetic responses within the $y - z$ plane (M_y and M_z) can be measured. At a specific momentum and energy transfer, incident neutrons can be polarized along the x, y, and z directions, and the scattered

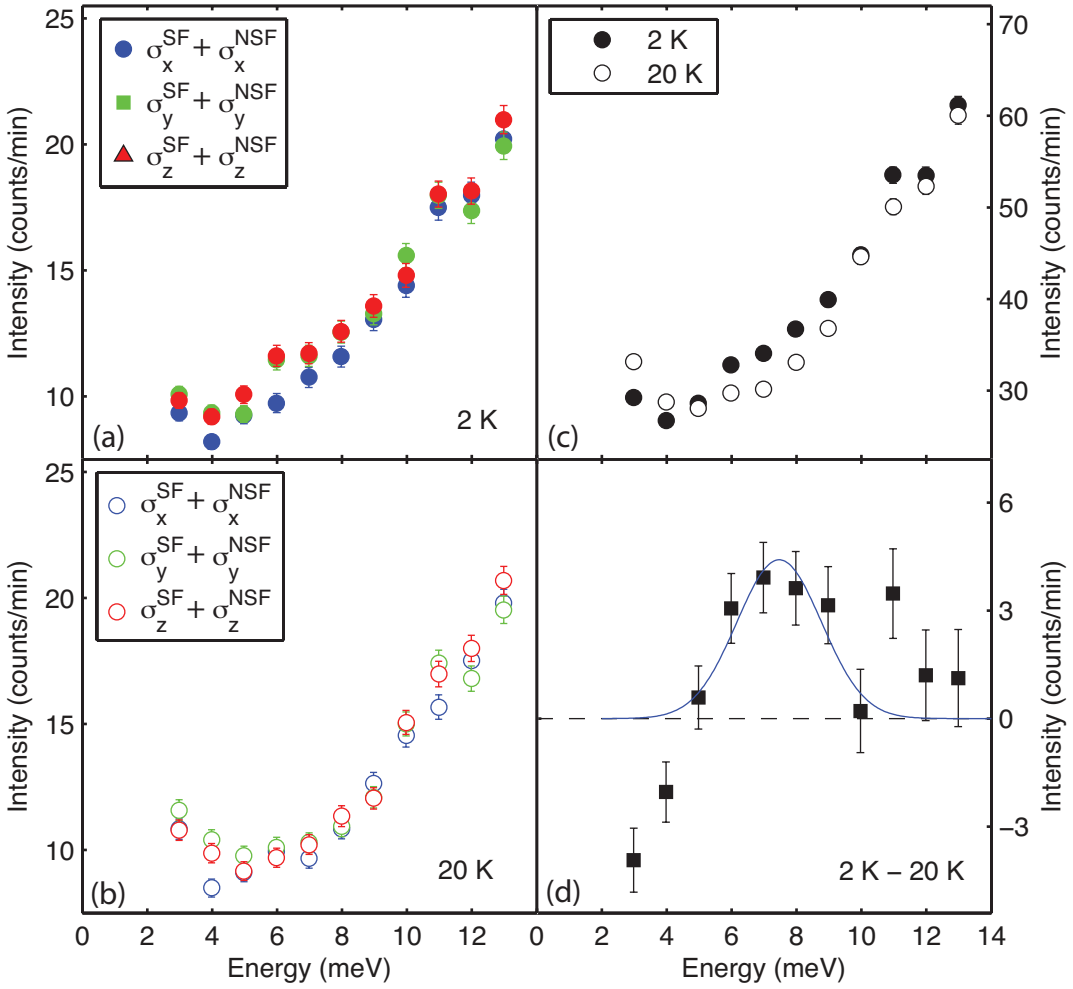

Figure 5.4: (Color online) (a) Simulation of unpolarized energy scans using $\sigma_\alpha^{\mathrm{SF}} + \sigma_\alpha^{\mathrm{NSF}}$ with $\alpha = x, y, z$ at 2 K and (b) 20 K. The wave vector is fixed at $\mathbf{Q} = (0.5, 0.5, 1)$. (c) Unpolarized energy scan at $(1/2, 1/2, 1)$ below and above T_c obtained by adding all six channels together. (d) Temperature difference plot between 2 K and 20 K reveals a neutron spin resonance at $E = 7$ meV and negative scattering below 4 meV, very similar to the earlier unpolarized measurements on the same Ni-doping level [Wang et al., 2010].

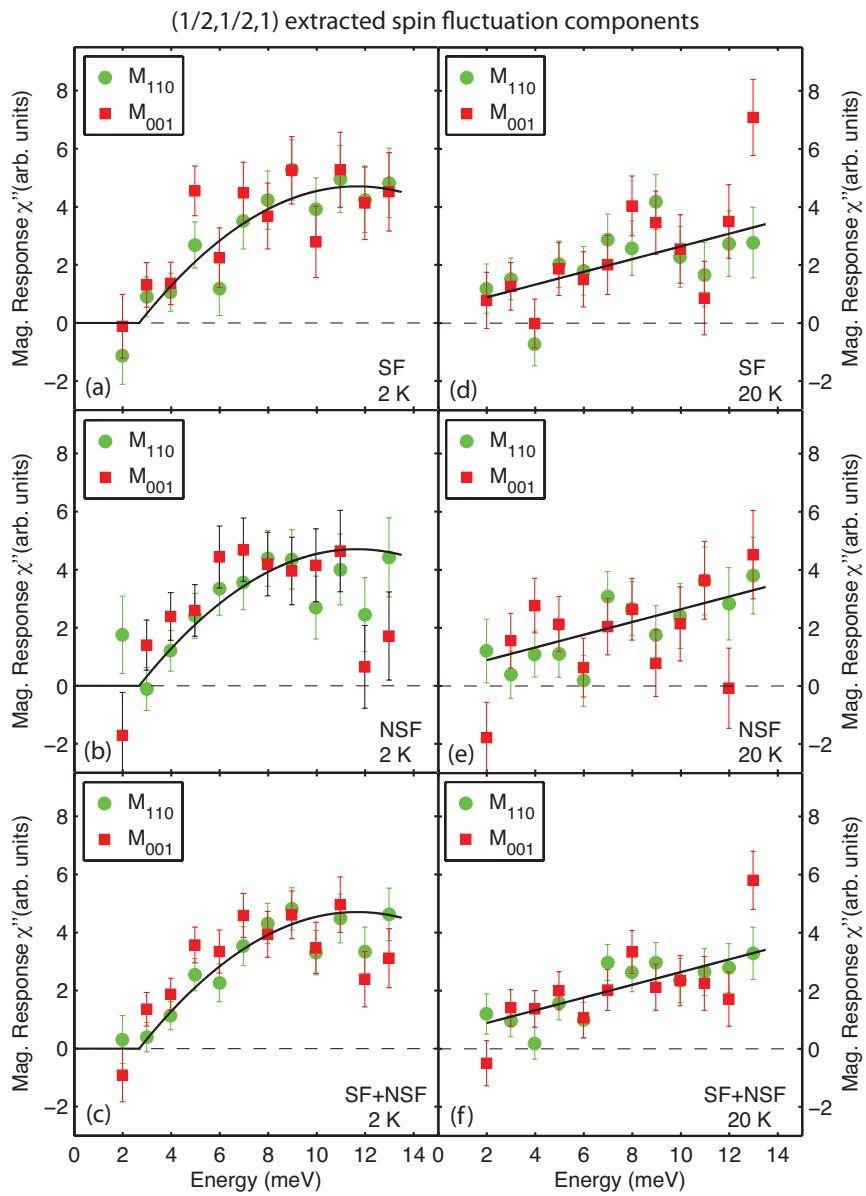

Figure 5.5: (Color online) Neutron polarization analysis used to extract the in-plane (M_{110}) and out-of-plane M_{001} components of spin excitations in $BaFe_{1.85}Ni_{0.15}As_2$ from SF and NSF data in Fig. 2. M_{110} and M_{001} at 2 K are extracted from (a) SF, and (b) NSF data in Figure 3. (d,e) M_{110} and M_{001} at 20 K. The above analysis is based on the assumption that the background scattering for the x, y, and z spin polarizations are different (see eqs. (2) and (3)). However, if we assume that backgrounds are identical for different spin polarizations, we would obtain higher magnetic scattering intensity in the NSF channel compared with that of the SF channel at all measured temperatures and energies. At present, the microscopic origin of such a difference is unclear. (c) The combination of SF and NSF data at 2K. (f) The combination of SF and NSF data at 20K. These data reveal isotropic paramagnetic scattering at the probed energies and temperatures.

neutrons can have polarizations either parallel (neutron nonspin flip or NSF, ↑↑) or antiparallel (neutron spin flip or SF, ↑↓) to the incident neutrons. Therefore, the six neutron scattering cross sections can be written as $\sigma_\alpha^{\mathrm{NSF}}$ and $\sigma_\alpha^{\mathrm{SF}}$, where $\alpha = x, y, z$ [Moon et al., 1969; Lipscombe et al., 2010]. If we use M_α and N to denote the magnetic response and nuclear scattering, respectively, the neutron scattering cross sections $\sigma_\alpha^{\mathrm{NSF}}$ and $\sigma_\alpha^{\mathrm{SF}}$ are related to M_α and N via Eq. (1):

$$\begin{pmatrix} \sigma_x^{\mathrm{SF}} \\ \sigma_y^{\mathrm{SF}} \\ \sigma_z^{\mathrm{SF}} \\ \sigma_x^{\mathrm{NSF}} \\ \sigma_y^{\mathrm{NSF}} \\ \sigma_z^{\mathrm{NSF}} \end{pmatrix} = \begin{pmatrix} 1 & 1 & 0 \\ 0 & 1 & 0 \\ 1 & 0 & 0 \\ 0 & 0 & 1 \\ 1 & 0 & 1 \\ 0 & 1 & 1 \end{pmatrix} \times \begin{pmatrix} M_y \\ M_z \\ N \end{pmatrix} \tag{5.1}$$

In a real experiment, neutron polarization is not 100% and there are also neutron spin independent backgrounds (nuclear-spin incoherent scattering and general instrumental background). Since neutron SF and NSF scattering processes have identical instrumental setups and only the spin directions of the incident neutrons are changed, we assume constant backgrounds of B_1, B_2, B_3 for neutron polarizations in the x, y, and z directions, respectively. We have measured the neutron flipping ratios R for all three neutron polarizations, and found them to be independent of neutron polarization directions within the errors of our measurements. By considering finite flipping ratio

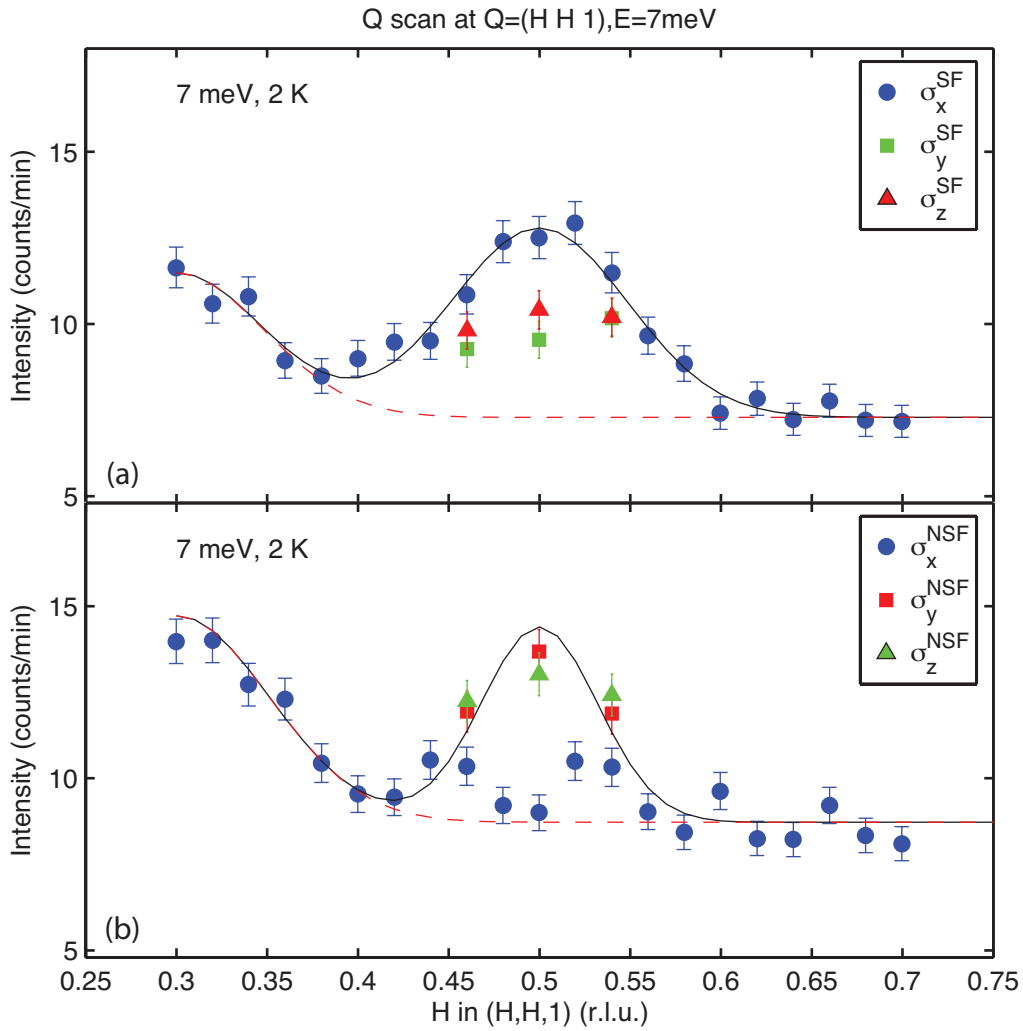

Figure 5.6: (Color online) Constant-energy scans along the $[H, H, 1]$ direction at the resonance energy of $E = 7$ meV at 2 K for different neutron polarization directions. (a) Neutron SF scattering cross sections for the x, y, and z polarization directions. (b) NSF scattering cross sections. A clear peak is seen at $\mathbf{Q} = (0.5, 0.5, 1)$ in the σ_x^{SF} channel that is absent in the σ_x^{NSF} channel, thus confirming the magnetic nature of the resonance.

and assume that instrumental backgrounds for different neutron polarizations are slightly different, we have

$$\begin{pmatrix} \sigma_x^{\mathrm{SF}} - B_1 \\ \sigma_y^{\mathrm{SF}} - B_2 \\ \sigma_z^{\mathrm{SF}} - B_3 \\ \sigma_x^{\mathrm{NSF}} - B_1 \\ \sigma_y^{\mathrm{NSF}} - B_2 \\ \sigma_z^{\mathrm{NSF}} - B_3 \end{pmatrix} = \frac{1}{R+1} \begin{pmatrix} R & R & 1 \\ 1 & R & 1 \\ R & 1 & 1 \\ 1 & 1 & R \\ R & 1 & R \\ 1 & R & R \end{pmatrix} \times \begin{pmatrix} M_y \\ M_z \\ N \end{pmatrix}, \tag{5.2}$$

where the flipping ratio R is measured by the leakage of NSF nuclear Bragg peaks into the magnetic SF channel $R = \sigma_{Bragg}^{\mathrm{NSF}}/\sigma_{Bragg}^{\mathrm{SF}} \approx 14$. The magnetic moments M_y and M_z can be extracted from Eq.(2) via

$$\begin{cases} \sigma_x^{\mathrm{SF}} - \sigma_y^{\mathrm{SF}} + B_1 = \sigma_y^{\mathrm{NSF}} - \sigma_x^{\mathrm{NSF}} - B_1 = cM_y, \\ \\ \sigma_x^{\mathrm{SF}} - \sigma_z^{\mathrm{SF}} + B_2 = \sigma_z^{\mathrm{NSF}} - \sigma_x^{\mathrm{NSF}} - B_2 = cM_z \end{cases} \tag{5.3}$$

where $c = (R-1)/(R+1)$, and B_1, B_2 are constant backgrounds. By measuring all six NSF and SF neutron scattering cross sections, we can unambiguously determine M_y and M_z. To estimate the in-plane and out-of-plane components of the magnetic scattering M_{110} and M_{001}, we note that $M_{110} = M_{1\bar{1}0} \equiv M_z$ due to the tetragonal symmetry of the system. Therefore, M_{001} can be calculated using $M_y = M_{110}\sin^2\theta +$

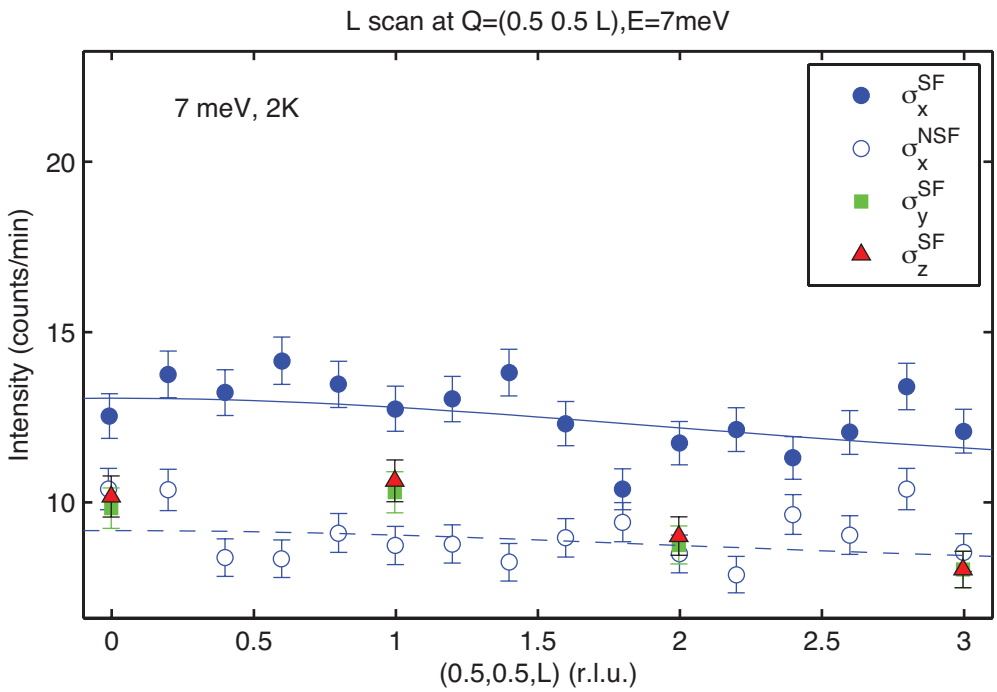

Figure 5.7: (Color online) Constant-energy scans along $(0.5, 0.5, L)$ at the resonance energy of $E = 7$ meV. The σ_x^{SF} and σ_x^{NSF} data show no L dependence. The solid and dashed lines show the expected magnetic scattering intensity assuming an Fe^{2+} form factor.

$M_{001} \cos^2 \theta$. This allows a complete determination of the temperature and energy dependence of M_{110} and M_{001}.

5.3 Experimental Results

In previous polarized neutron scattering experiments performed on optimally doped $BaFe_{1.9}Ni_{0.1}As_2$ [Lipscombe et al., 2010], the in-plane (M_{110}) and out-of-plane (M_{001}) magnetic fluctuations are gapless and approximately isotropic in the normal state above T_c. Upon entering the superconducting state, the M_{110} spectra re-arrange with a spin gap below $E = 2$ meV and a resonance peak near $E = 7$ meV. On the other

hand, the M_{001} spectra peak near $E = 4$ meV and have a smaller spin gap (Figure 4 in Ref. [Lipscombe et al., 2010]). Figures 3(a)-3(d) show all six constant-$\mathbf{Q}$ scattering cross sections $\sigma^{\mathrm{SF}}_{x,y,z}$ and $\sigma^{\mathrm{NSF}}_{x,y,z}$ taken at the AF wave vector $\mathbf{Q} = (1/2, 1/2, 1)$ below and above T_c. For SF scattering, σ^{SF}_y is approximately equal to σ^{SF}_z at 2 K and 20 K, but both σ^{SF}_y and σ^{SF}_z are smaller than σ^{SF}_x (Figs. 3(a) and 3(c)). For the NSF scattering, the situation is similar except that σ^{NSF}_x is smaller than σ^{NSF}_y and σ^{NSF}_z (Figures 3(b) and 3(d)). These results indicate the presence of paramagnetic scattering, since for purely nuclear scattering there would be no difference between the scattering from different neutron polarizations ($\sigma^{\mathrm{SF}}_x = \sigma^{\mathrm{SF}}_y = \sigma^{\mathrm{SF}}_z$) [Moon et al., 1969].

In a previous unpolarized neutron scattering experiment performed on $BaFe_{1.85}Ni_{0.15}As_2$, a neutron spin resonance was observed near $E = 6$ meV in the superconducting state, found by taking a temperature difference between constant-$\mathbf{Q}$ scans at $(0.5, 0.5, 1)$ r.l.u. [Wang et al., 2010]. Before determining the possible magnetic anisotropy from neutron polarization analysis, we note from Eq. (2) that $\sigma^{\mathrm{SF}}_x + \sigma^{\mathrm{NSF}}_x = M_y + M_z + N + 2B_1$, $\sigma^{\mathrm{SF}}_y + \sigma^{\mathrm{NSF}}_y = M_y + M_z + N + 2B_2$, and $\sigma^{\mathrm{SF}}_z + \sigma^{\mathrm{NSF}}_z = M_y + M_z + N + 2B_3$ are the scattering cross sections for an unpolarized neutron scattering experiment. Assuming the background scattering has no temperature dependence across T_c, the temperature difference data of $\sigma^{\mathrm{SF}}_\alpha + \sigma^{\mathrm{NSF}}_\alpha$ should recover unpolarized neutron scattering results [Wang et al., 2010]. Figures 4(a) and 4(b) show the sum of the raw data $\sigma^{\mathrm{SF}}_\alpha + \sigma^{\mathrm{NSF}}_\alpha$ above and below T_c, respectively for $\alpha = x$, y and z. Figure 4(c) plots the sum of all six scattering cross sections $\sigma^{\mathrm{SF}}_{x,y,z}$ and $\sigma^{\mathrm{NSF}}_{x,y,z}$ at $\mathbf{Q} = (1/2, 1/2, 1)$ below and

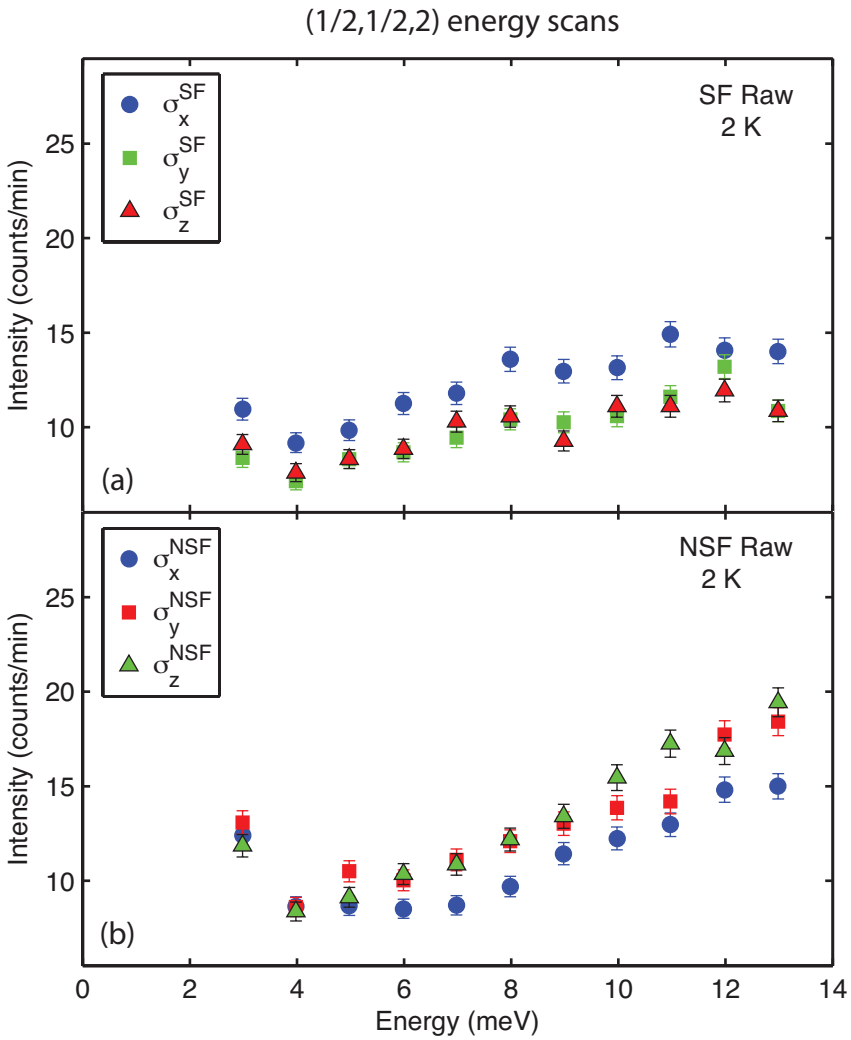

Figure 5.8: (Color online) Constant-Q scans at $\mathbf{Q} = (0.5, 0.5, 2)$ at 2 K. (a) The three neutron SF scattering energy scans below T_c, marked as $\sigma^{\mathrm{SF}}_{x,y,z}$. (b) Identical scans in the neutron NSF channel, marked as $\sigma^{\mathrm{NSF}}_{x,y,z}$.

above T_c. The temperature difference in Fig. 4(d) clearly shows a resonant feature at $E = 7$ meV, consistent with earlier unpolarized neutron scattering results [Wang et al., 2010].

To extract any possible anisotropy of the resonance and normal state spin excitations, we use $\sigma_\alpha^{\rm SF}$ and $\sigma_\alpha^{\rm NSF}$ with Eq. (3) to independently determine M_y and M_z. Since M_z is equal to M_{110} and $M_y = M_{110}\sin^2\theta + M_{001}\cos^2\theta$, M_{110} and M_{001} can be independently calculated from either $\sigma_\alpha^{\rm SF}$ or $\sigma_\alpha^{\rm NSF}$. One can then calculate the imaginary part of the dynamic susceptibility $\chi''(Q,\omega)$ via $\chi''(Q,\omega) = [1-\exp(-\hbar\omega/k_BT)]S(Q,\omega)$, where $S(Q,\omega) = M_{110}$ or M_{001}, and $E = \hbar\omega$. Figures 5(a)-5(d) summarize results for $\chi''_{110}(Q,\omega)$ and $\chi''_{001}(Q,\omega)$ at the AF wave vector $Q = (0.5, 0.5, 1)$ in the superconducting and normal states, respectively. The $\chi''_{110}(Q,\omega)$ and $\chi''_{001}(Q,\omega)$ results in Figures 5(a) and 5(b) are obtained using $\sigma_\alpha^{\rm SF}$, while the similar results shown in Figures 5(c) and 5(d) are independent calculations using $\sigma_\alpha^{\rm NSF}$. These results are identical to within the errors of the measurements. Figures 5(c) and 5(d) show combined SF+NSF results for $\chi''_{110}(Q,\omega)$ and $\chi''_{001}(Q,\omega)$ to improve the statistics. In the normal state at 20 K, $\chi''_{110}(Q,\omega)$ and $\chi''_{001}(Q,\omega)$ are identical and increase linearly with increasing energy (Figure 5(f)). At low temperatures ($T = 2$ K, a spin gap is present below $E \approx 3$ meV and a broad resonance is apparent near $E \approx 7$ meV. $\chi''_{110}(Q,\omega)$ and $\chi''_{001}(Q,\omega)$ are again identical to within the errors of our measurements. Therefore, there is no observable magnetic anisotropy of the spin excitations of overdoped $BaFe_{1.85}Ni_{0.15}As_2$ in both the normal and superconducting states at $\mathbf{Q} = (0.5, 0.5, 1)$.

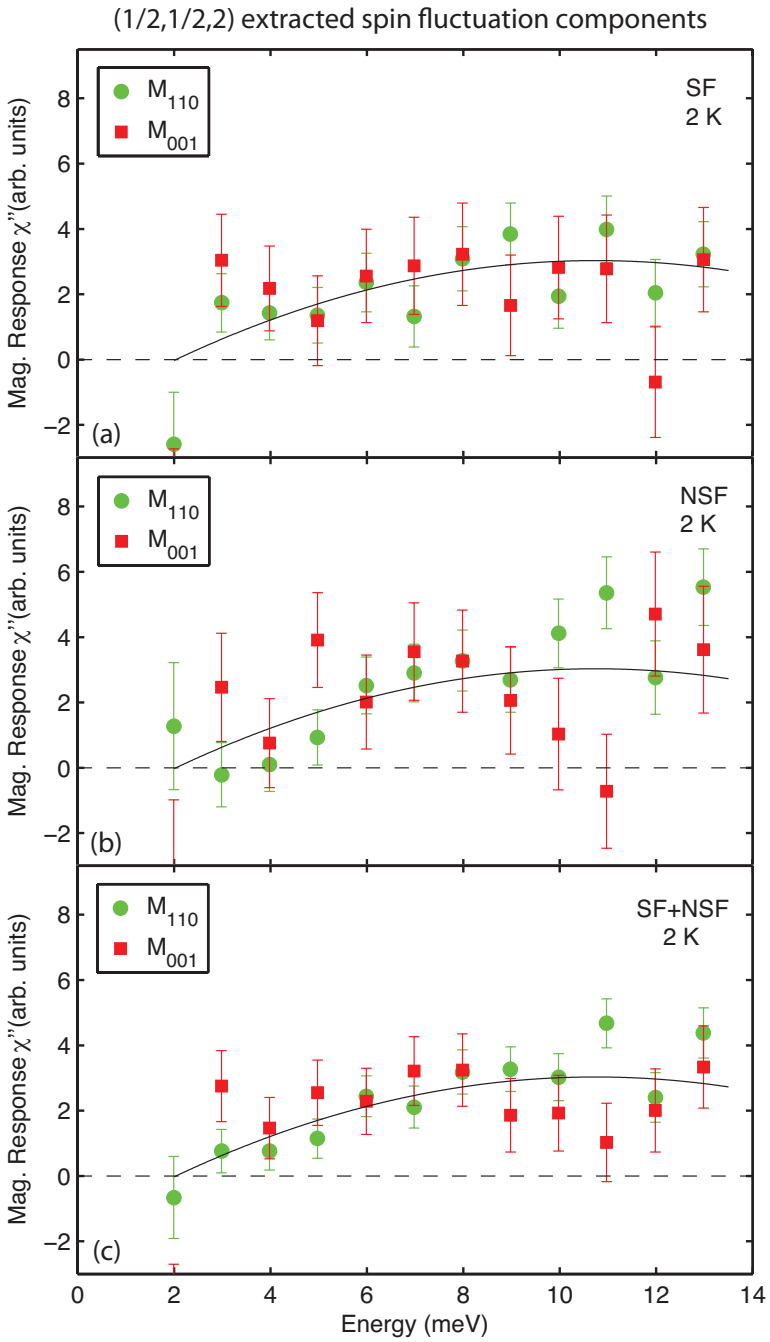

Figure 5.9: (Color online) Constant-Q scans at $\mathbf{Q} = (0.5, 0.5, 2)$ at 2 K. The in-plane (M_{110}) and out-of-plane (M_{001}) magnetic response extracted from the (a) SF data, and (b) NSF data, respectively; (c) The combination of SF and NSF data at 2 K shows no difference between the two magnetic moment components, indicating isotropic paramagnetic scattering.

Figures 6(a) and 6(b) show constant-energy scans at the resonance energy along $(H, H, 1)$ for $\sigma_\alpha^{\rm SF}$ and $\sigma_\alpha^{\rm NSF}$. While the SF scattering $\sigma_x^{\rm SF}$ shows a clear peak centered at the AF wave vector $\mathbf{Q} = (0.5, 0.5, 1)$ (Figure 6(a)), the NSF scattering $\sigma_x^{\rm NSF}$ (Figure 6(b)) is featureless near $\mathbf{Q} = (0.5, 0.5, 1)$. This suggests that the resonance peak above the background in Figure 6(a) is entirely magnetic in origin. If the resonance is purely isotropic paramagnetic scattering, one would expect $\sigma_x^{\rm SF} - B_1 \approx 2(\sigma_y^{\rm SF} - B_2) \approx 2(\sigma_z^{\rm SF} - B_3)$ and $(\sigma_y^{\rm NSF} - B_2) \approx (\sigma_z^{\rm NSF} - B_3)$. Inspection of Figures 6(a) and 6(b) reveal that this is indeed the case, thus confirming the isotropic nature of the magnetic resonance.

To determine whether the spin excitations at the resonance energy exhibit any c-axis modulation in intensity, we carried out constant-energy scans along $(0.5, 0.5, L)$ in the superconducting state at $E = 7$ meV. As one can see in Figure 7, the magnetic scattering intensity decreases smoothly with increasing L, consistent with the expected magnetic intensity reduction due to the Fe^{2+} form factor (solid line). There is no evidence for a L-axis modulation of the magnetic scattering.

Finally, to see whether the isotropic magnetic scattering near the AF wave vector $\mathbf{Q} = (0.5, 0.5, 1)$ is independent of the c-axis momentum transfer, we carried out $\sigma_\alpha^{\rm SF}$ and $\sigma_\alpha^{\rm NSF}$ constant-Q scans in the superconducting state at $\mathbf{Q} = (0.5, 0.5, 2)$ (Figure 8). Similar to the data in Figure 3, the SF scattering $\sigma_x^{\rm SF}$ is larger than $\sigma_y^{\rm SF}$ and $\sigma_z^{\rm SF}$ (Figure 8(a)), while the NSF scattering $\sigma_x^{\rm NSF}$ is smaller than $\sigma_y^{\rm NSF}$ and $\sigma_z^{\rm NSF}$. Using this raw data shown in Figure 8, we are able to obtain the energy dependence of $\chi''_{110}(Q, \omega)$ and $\chi''_{001}(Q, \omega)$ at $\mathbf{Q} = (0.5, 0.5, 2)$ as shown in Figures 9(a)

and 9(b). Consistent with the constant-Q scans at $\mathbf{Q} = (0.5, 0.5, 1)$, we find isotropic magnetic scattering at $\mathbf{Q} = (0.5, 0.5, 2)$. Figure 9(c) shows the energy dependence of $\chi''_{110}(Q, \omega)$ and $\chi''_{001}(Q, \omega)$ obtained by combining the SF and NSF scattering data in Figures 9(a) and 9(b). Similar to Figure 5(c), a spin gap is present below $E = 3$ meV and $\chi''_{110}(Q, \omega)$ and $\chi''_{001}(Q, \omega)$ increase with increasing energy. Therefore, spin excitations in overdoped $BaFe_{1.85}Ni_{0.15}As_2$ are isotropic below and above T_c at all energies probed.

5.4 Discussion and Conclusions

In previous polarized neutron scattering experiments on optimally electron-doped $BaFe_{1.9}Ni_{0.15}As_2$, $\chi''_{110}(Q, \omega)$ and $\chi''_{001}(Q, \omega)$ at $\mathbf{Q} = (0.5, 0.5, 1)$ were found to have peaks near $E = 7$ and 4 meV, respectively, in the superconducting state [Lipscombe et al., 2010]. These results were interpreted as being due to the presence of spin-orbital/lattice coupling [Lipscombe et al., 2010]. In a recent polarized neutron scattering work on the AF parent compound $BaFe_2As_2$, it was found that in-plane polarized magnons exhibit a larger single iron anisotropy gap than the out-of-plane polarized ones [Qureshi et al., 2012]. This means that $\chi''_{110}(Q, \omega)$ has a larger gap than $\chi''_{001}(Q, \omega)$ at $\mathbf{Q} = (0.5, 0.5, 1)$ in the AF ordered state, where the Fe moments are locked to the a-axis of the orthorhombic structure [Huang et al., 2008; Zhao et al., 2008a; Goldman et al., 2008][along the [110] direction in our tetragonal notation].

From the electronic phase diagram of $BaFe_{2-x}Ni_xAs_2$ in Figure 1, we see that although the optimally electron-doped $BaFe_{1.9}Ni_{0.1}As_2$ has tetragonal structure with no static AF order [Chi et al., 2009], it is very close to that region of the phase diagram where incommensurate static AF order coexists with superconductivity [Luo et al., 2012b]. This suggests that the observed anisotropy between the in-plane ($\chi''_{110}(Q,\omega)$) and out-of-plane ($\chi''_{001}(Q,\omega)$) dynamic susceptibility in tetragonal superconducting $BaFe_{1.9}Ni_{0.1}As_2$ [Lipscombe et al., 2010] may have the same microscopic origin as the spin wave anisotropy gaps in the AF orthorhombic $BaFe_2As_2$ [Qureshi et al., 2012]. If this is indeed the case, the resonance is only weakly anisotropic near optimal superconductivity, and becomes isotropic in the electron over-doped $BaFe_{1.9}Ni_{0.15}As_2$. Therefore, these results suggest that the resonance in electron over-doped $BaFe_{2-x}Ni_xAs_2$ is mostly consistent with the singlet-triplet excitations of electron Cooper pairs. The observed spin excitation anisotropy in optimally doped $BaFe_{2-x}Ni_xAs_2$ is likely due to single iron anisotropy of spin waves in the parent compound, and suggests that such anisotropy is present even for samples with tetragonal structure. Thus, the strong spin-orbital-lattice coupling in electron-doped $BaFe_{1.9}Ni_{0.1}As_2$ is important for samples up to optimal superconductivity, and becomes less important for the overdoped regime.

Chapter 6

Magnetic Excitations in Optimally Hole-doped $Ba_{0.67}K_{0.33}Fe_2As_2$

We use polarized inelastic neutron scattering (INS) to study spin excitations of optimally hole-doped superconductor $Ba_{0.67}K_{0.33}Fe_2As_2$ ($T_c = 38$ K). In the normal state, the imaginary part of the dynamic susceptibility, $\chi''(Q, \omega)$, shows magnetic anisotropy for energies below $\sim$7 meV with c-axis polarized spin excitations larger than that of the in-plane component. Upon entering into the superconducting state, previous unpolarized INS experiments have shown that spin gaps at $\sim$5 and 0.75 meV open at wave vectors $Q = (0.5, 0.5, 0)$ and $(0.5, 0.5, 1)$, respectively, with a broad neutron spin resonance at $E_r = 15$ meV. Our neutron polarization analysis reveals that the large difference in spin gaps is purely due to different spin gaps in the c-axis and in-plane polarized spin excitations, resulting resonance with different energy widths for the c-axis and in-plane spin excitations. The observation of spin anisotropy

in both opitmally electron and hole-doped $BaFe_2As_2$ is due to their proximity to the AF ordered $BaFe_2As_2$ where spin anisotropy exists below T_N.

6.1 Introduction

Neutron polarization analysis has played an important role in determining the magnetic structure and excitations of solids [Moon et al., 1969]. For high-transition temperature (High-T_c) copper oxide superconductors derived from hole or electron-doping from their antiferromagnetic (AF) parent compounds, neutron polarization analysis have conclusively shown that the collective magnetic excitation coupled to superconductivity at the AF wave vector of the parent compounds, termed neutron spin resonance [Rossat-Mignod et al., 1991], has a magnetic origin [Mook et al., 1993; Fong et al., 1996; Dai et al., 2001; Headings et al., 2011; Wilson et al., 2006c; Zhao et al., 2011; Eschrig, 2006]. Furthermore, by carrying out neutron polarization analysis with a spin-polarized incident neutron beam along the scattering wave vector $\mathbf{Q} = \mathbf{k}_i - \mathbf{k}_f$ (where $\mathbf{k}_i$ and $\mathbf{k}_f$ are the incident and final wave vectors of the neutron, respectively), $\hat{\mathbf{x}}||\mathbf{Q}$; perpendicular to $\mathbf{Q}$ but in the scattering plane, $\hat{\mathbf{y}}\perp\mathbf{Q}$; and perpendicular to $\mathbf{Q}$ and the scattering plane, $\hat{\mathbf{z}}\perp\mathbf{Q}$, one can use neutron spin flip (SF) scattering cross sections $\sigma_{xx}^{\mathrm{SF}}, \sigma_{yy}^{\mathrm{SF}}$, and $\sigma_{zz}^{\mathrm{SF}}$ to determine the spatial anisotropy of spin excitations [Moon et al., 1969]. If the resonance is an isotropic triplet excitation of the singlet superconducting ground state, one expects that the degenerate triplet would be isotropic in space as pure paramagnetic scattering

[Eschrig, 2006]. For optimally hole-doped copper oxide superconductor $YBa_2Cu_3O_{6.9}$ ($T_c = 93$ K), neutron polarization analysis reveals that spin excitations in the normal state are spatially isotropic and featureless for energies $10 \leq E \leq 60$ meV, consistent with pure paramagnetic scattering. Upon entering into the superconducting state, a quasi-isotropic spin resonance occurs at $E_r = 40$ meV to within the precision of the measurements and a spin anisotropy develops in the lower energy $10 \leq E \leq 30$ meV, resulting in a clear spin gap below 22 meV for the c-axis polarized dynamic susceptibility χ''_c and in-plane $\chi''_{a/b}$ for $E \geq 10$ meV [Headings et al., 2011]. The low-energy spin anisotropy is likely due to spin-orbit coupling in the system. For optimally electron-doped copper oxide superconductor $Pr_{0.88}LaCe_{0.12}CuO_{4-\delta}$, spin excitations are isotropic both above and below T_c [Zhao et al., 2011]. Therefore, the spin anisotropy in the superconducting state of hole-doped $YBa_2Cu_3O_{6.9}$ is unrelated to the normal state paramagnetic scattering.

Like copper oxide superconductors, superconductivity in iron pnictides also arises when electrons or holes are doped into their AF parent compounds [Kamihara et al., 2008; Rotter et al., 2008; Li et al., 2009a; de la Cruz et al., 2008b; Dai et al., 2012]. Furthermore, unpolarized neutron scattering experiments have shown that both hole and electron-doped iron pnictides exhibits a neutron spin resonance similar to copper oxide superconductors [Christianson et al., 2008; Zhang et al., 2011; Lumsden et al., 2009; Chi et al., 2009; Inosov et al., 2009; Luo et al., 2012a]. In the initial polarized neutron scattering experiment on optimally electron-doped superconductor $BaFe_{1.9}Ni_{0.1}As_2$ ($T_c = 20$ K), χ''_c was found to be much larger than $\chi''_{a/b}$ for energies

$2 \leq E \leq 6$ meV below T_c , while the resonance at $E_r = 7$ meV is only weakly anisotropic [Lipscombe et al., 2010]. In a subsequent polarized neutron scattering measurement on undoped AF parent compound $BaFe_2As_2$ [Qureshi et al., 2012], isotropic paramagnetic scattering at low-energy ($E = 10$ meV) were found to become anisotropic spin waves below the Néel temperature T_N with a much larger in-plane ($\chi''_{a/b}$) spin gap than that of the out-of-plane gap (χ''_c). These results indicate a strong single-ion anisotropy and spin-orbit coupling, suggesting that more energy is needed to rotate a spin within the orthorhombic *a*-*b* plane than rotating it to the *c*-axis [Qureshi et al., 2012]. However, similar polarized neutron experiments on electron-overdoped $BaFe_{1.85}Ni_{0.15}As_2$ ($T_c = 14$ K), which is far away from the AF ordered phase, reveal isotropic paramagnetic scattering both above and below T_c [Liu et al., 2012b]. Very recently, Steffens *et al.* report evidence for two resonance-like excitations in the superconducting state of optimally electron-doped $BaFe_{1.88}Co_{0.12}As_2$ ($T_c = 24$ K). In addition to an isotropic resonance at $E = 8$ meV with weak dispersion along the *c*-axis, there is a resonance at $E = 4$ meV polarized only along the *c*-axis with strong intensity variation along the *c*-axis [Steffens et al., 2012]. In the normal state, there are isotropic paramagnetic scattering at AF wave vectors with $L = 0$ and weak anisotropic scattering with a larger *c*-axis polarized intensity at $L = 1$ [Steffens et al., 2012].

If the observed anisotropic magnetic scattering in the superconducting state of optimally electron-doped $BaFe_{1.9}Ni_{0.1}As_2$ [Lipscombe et al., 2010] and $BaFe_{1.88}Co_{0.12}As_2$ [Steffens et al., 2012] are indeed associated with the anisotropic spin waves in

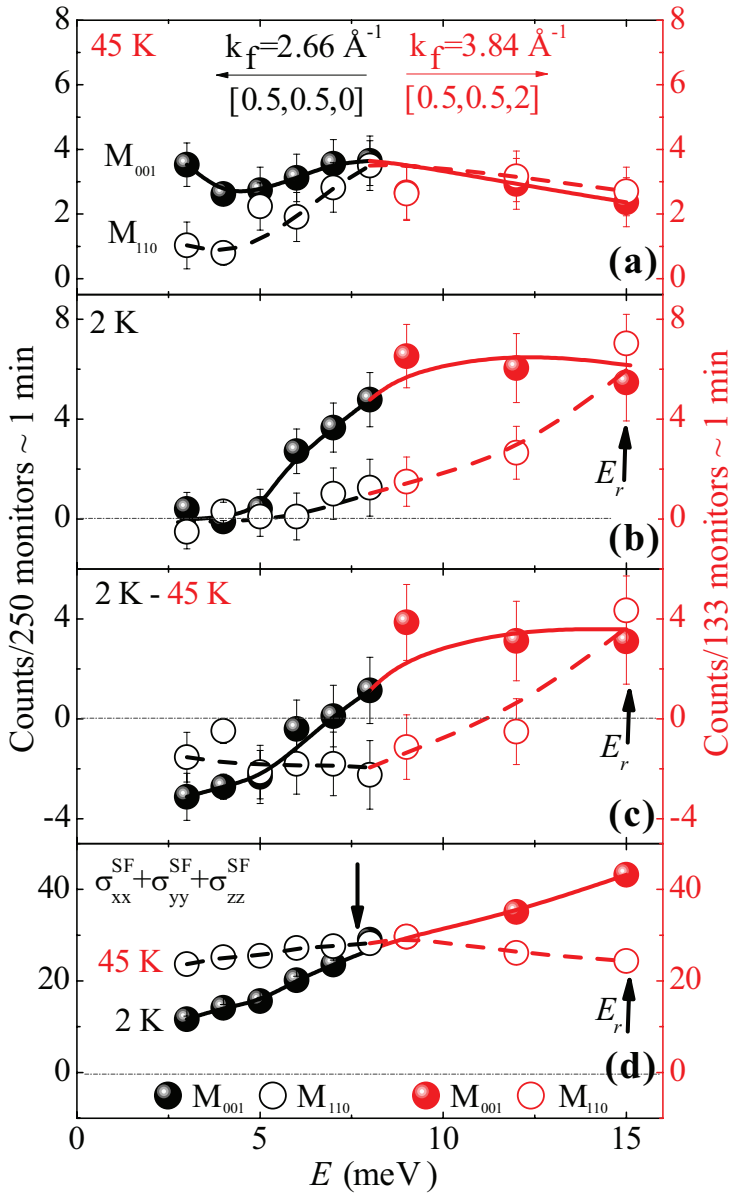

Figure 6.1: (Color online) Neutron polarization analysis determined c-axis ($\chi''_c \propto M_{001}$) and in-plane ($\chi''_{a/b} \propto M_{110}$) components of spin excitations in $Ba_{0.67}K_{0.33}Fe_2As_2$ from raw SF constant-Q scans at $\mathbf{Q} = (0.5, 0.5, 0)$ and and $(0.5, 0.5, 2)$. To extract M_{001} and M_{110}, we use methods described in Ref. [Liu et al., 2012b] and assume $M_{1\bar{1}0} = M_{110}$ in the tetragonal crystal. (a) Energy dependence of M_{001} and M_{110} at $T = 45$ K. (b) Identical scans at $T = 2$ K. (c) The solid and open circles show the temperature difference (2 K−45 K) for M_{001} and M_{110}, respectively. (d) The sum of $\sigma^{\rm SF}_{xx} + \sigma^{\rm SF}_{yy} + \sigma^{\rm SF}_{zz}$ at 45 and 2 K. Since background scattering is not expected to change between these temperatures [Zhang et al., 2011], such a procedure will increase statistics of magnetic scattering. The black data points are collected at $\mathbf{Q} = (0.5, 0.5, 0)$ with $k_f = 2.66$ Å^{-1}, while the red data points are at $\mathbf{Q} = (0.5, 0.5, 1)$ with $k_f = 3.84$ Å^{-1}. The solid and dashed lines are guided to the eyes.

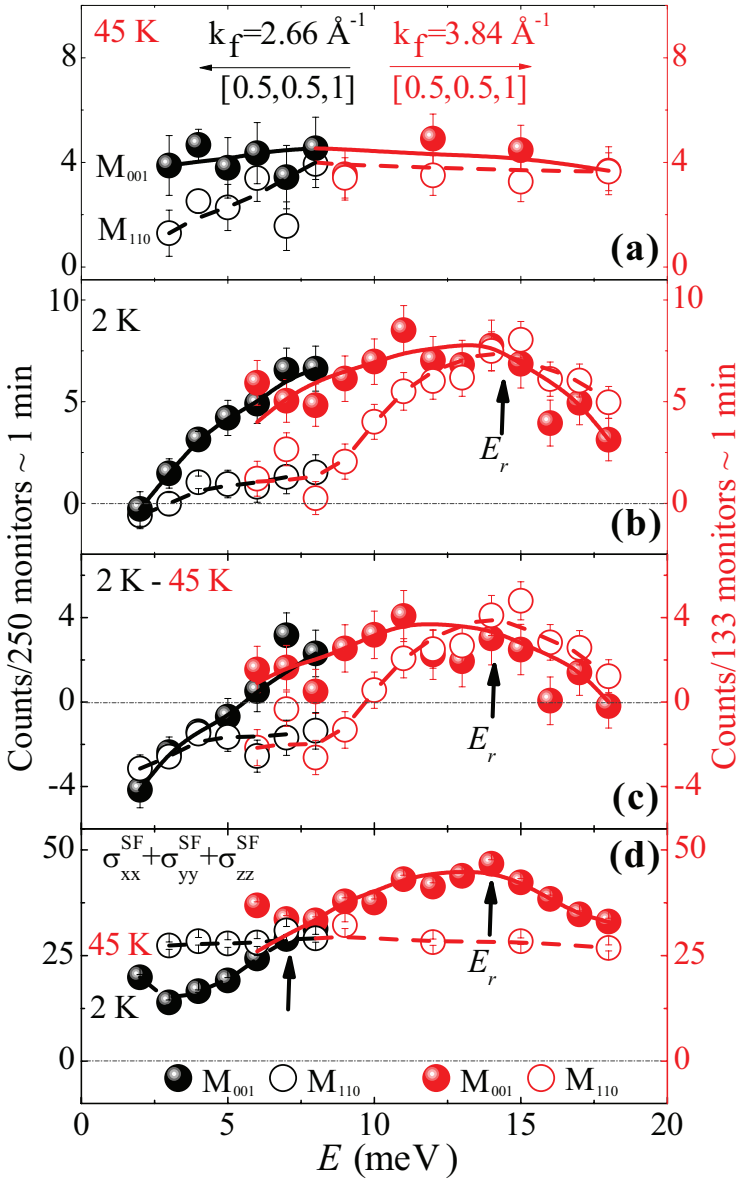

Figure 6.2: (Color online) Constant-Q scans at $\mathbf{Q} = (0.5, 0.5, 1)$ below and above T_c. (a) Energy dependence of M_{001} and M_{110} at $T = 45$ K and (b) at 2 K. The superconductivity-induced spin gaps are at ≤ 2 and 7 meV for M_{001} and M_{110}, respectively. At resonance energy of $E_r = 15$ meV, the scattering is isotropic. (c) The solid and open circles show the temperature difference (2 K$-$45 K) for M_{001} and M_{110}, respectively. (d) The sum of $\sigma_{xx}^{\mathrm{SF}} + \sigma_{yy}^{\mathrm{SF}} + \sigma_{zz}^{\mathrm{SF}}$ at 45 and 2 K. The solid and dashed lines are guided to the eyes.

$BaFe_2As_2$ [Qureshi et al., 2012], one would expect similar anisotropic spin excitations in hole-doped materials not too far away from the parent compound. In this chapter, we use neutron polarization analysis on spin excitations of the optimally hole-doped superconducting $Ba_{0.67}K_{0.33}Fe_2As_2$. From the previous unpolarized INS work on the same sample, we know that spin excitations in the superconducting state have a resonance at $E_r = 15$ meV, a small spin gap ($E_g \approx 0.75$ meV) at $\mathbf{Q} = (0.5, 0.5, 0)$ and a large gap ($E_g = 5$ meV) at $(0.5, 0.5, 1)$ [Zhang et al., 2011]. In the normal state, spin excitations at both wave vectors are gapless and increase linearly with increasing energy [Zhang et al., 2011]. Our polarized INS experiments reveal that the persistent low-energy spin excitations at the AF wave vector $(0.5, 0.5, 1)$ below T_c are entirely c-axis polarized. Although there is also superconductivity-induced spin anisotropy similar to optimally electron-doped $BaFe_{1.9}Ni_{0.1}As_2$ [Lipscombe et al., 2010] and $BaFe_{1.88}Co_{0.12}As_2$ [Steffens et al., 2012], the low-energy c-axis polarized spin excitations do not change across T_c and therefore cannot have the same microscopic origin as the spin isotropic resonance at $E_r = 15$ meV. We suggest that the persistent c-axis polarized spin excitations in the superconducting state of optimally hole and electron-doped iron pnictide superconductors is due to their proximity to the AF ordered parent compound. Their coupling to superconductivity may arise from different contributions of Fe $3d_{X^2-Y^2}$ and $3d_{XZ/YZ}$ orbitals to superconductivity [Malaeb et al., 2012].

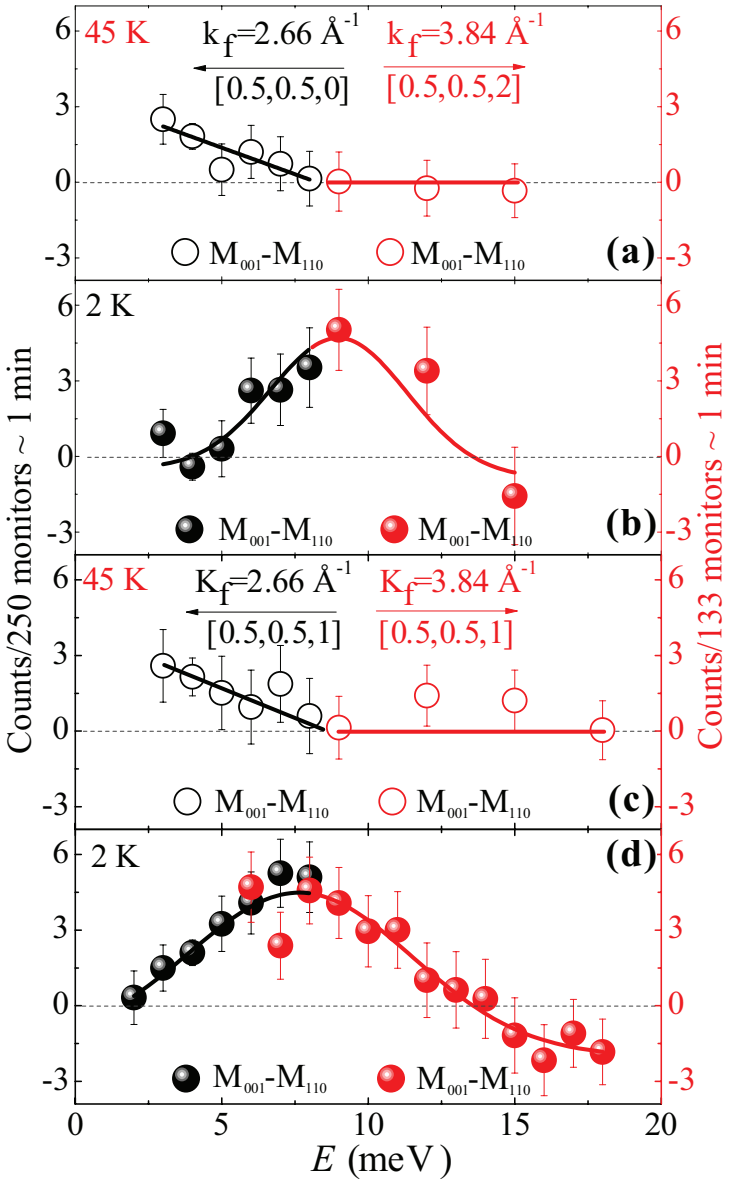

Figure 6.3: (Color online) Energy dependence of spin anisotropy as determined by the difference between $M_{001} - M_{110}$ for temperatures (a) 45 K and (b) 2 K at wave vector $\mathbf{Q} = (0.5, 0.5, 0)$ and $\mathbf{Q} = (0.5, 0.5, 2)$. Similar differences above (c) and below (d) T_c at $\mathbf{Q} = (0.5, 0.5, 1)$. The energy width is broader in (d) compared with (b). The solid and dashed lines are guided to the eyes.

6.2 Experimental Details

Single crystals of $Ba_{0.67}K_{0.33}Fe_2As_2$ are grown by a self-flux method [Zhang et al., 2011]. About 10 grams of single crystals are coaligned in the $[H, H, L]$ scattering plane (with mosaicity 3° at full width half maximum) with a tetragonal unit cell for which $a = b = 3.93$ Å, and $c = 13.29$ Å. In this notation, the vector $\mathbf{Q}$ in three-dimensional reciprocal space in Å^{-1} is defined as $\mathbf{Q} = H\mathbf{a}^* + K\mathbf{b}^* + L\mathbf{c}^*$, where H, K, and L are Miller indices and $\mathbf{a}^* = \hat{\mathbf{a}}2\pi/a, \mathbf{b}^* = \hat{\mathbf{b}}2\pi/b, \mathbf{c}^* = \hat{\mathbf{c}}2\pi/c$ are reciprocal lattice vectors. Our polarized INS experiments were carried out on the IN22 triple-axis spectrometer with Cryopad capability at the Institut Laue-Langevin in Grenoble, France. The fixed final neutron wave vectors were set at $k_f = 2.66$ Å^{-1} and $k_f = 3.84$ Å^{-1} in order to close the scattering triangles. To compare with previous polarized INS results on iron pnictides [Lipscombe et al., 2010; Qureshi et al., 2012; Liu et al., 2012b; Steffens et al., 2012], we converted the measured neutron SF scattering cross sections $\sigma_{xx}^{\mathrm{SF}}$, $\sigma_{yy}^{\mathrm{SF}}$, and $\sigma_{zz}^{\mathrm{SF}}$ into c-axis (M_{001}) and in-plane (M_{110}) components of the magnetic scattering [Liu et al., 2012b].

Figure 1 shows energy scans above and below T_c at wave vectors $\mathbf{Q} = (0.5, 0.5, 0)$ and $(0.5, 0.5, 2)$. We chose these two equivalent wave vectors with different fixed final neutron energies to satisfy the kinematic condition for the large covered energy range. Since the iron magnetic form factors, geometrical factors, and instrumental resolutions are different at these two wave vectors, we use left and right scales for $\mathbf{Q} = (0.5, 0.5, 0)$ and $(0.5, 0.5, 2)$, respectively. In the normal state (45 K), spin

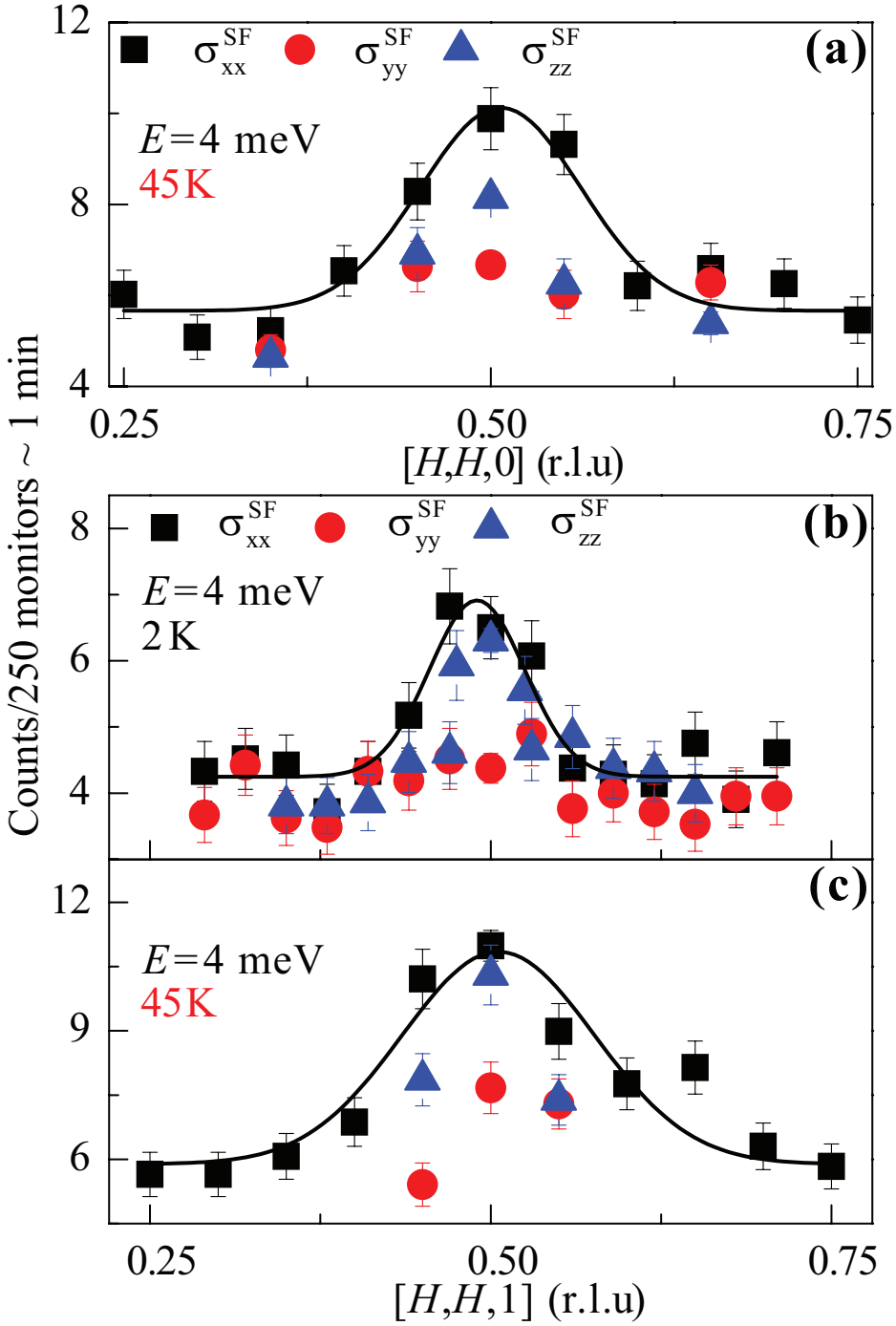

Figure 6.4: (Color online) Constant-energy scans along the $[H, H, 0]$ and $[H, H, 1]$ directions at an energy transfer of $E = 4$ meV for different neutron polarization directions. (a) Neutron SF scattering cross sections $\sigma^{\rm SF}_{xx}$, $\sigma^{\rm SF}_{yy}$, and $\sigma^{\rm SF}_{zz}$ at 45 K along the $[H, H, 0]$ direction. Similar scans along the $[H, H, 1]$ direction at (b) 2 K and (c) 45 K. All data are obtained with $k_f = 2.66$ Å^{-1}. The solid lines are fit by Gaussian.

anisotropy for energies below $E \approx 7$ meV is clear with M_{001} (χ''_c) larger than M_{110} ($\chi''_{a/b}$) [Fig. 1(a)]. For $E > 7$ meV, spin excitations are nearly isotropic. This is different from electron-doped $BaFe_{1.88}Co_{0.12}As_2$, where paramagnetic scattering at $\mathbf{Q} = (0.5, 0.5, 0)$ is isotropic above T_c [Steffens et al., 2012]. In the superconducting state (2 K), M_{001} and M_{110} in $Ba_{0.67}K_{0.33}Fe_2As_2$ vanish below 5 meV, consistent with opening of a superconductivity-induced spin gap [Fig. 1(b)] [Zhang et al., 2011]. From $E = 5$ meV to the resonance energy at $E_r = 15$ meV, both M_{001} and M_{110} increase with increasing energy, but with different slope resulting significant spin anisotropy ($M_{001} > M_{110}$) appearing near $E \approx 8$ meV [Fig. 1(b)]. This is similar to the spin anisotropy in $BaFe_{1.88}Co_{0.12}As_2$ [Steffens et al., 2012]. Figure 1(c) shows the temperature difference of magnetic scattering, revealing net intensity gains for M_{001} and M_{110} only above ∼7 and 10 meV, respectively. Figure 1(d) shows the sum of the SF magnetic scattering intensities for three different neutron polarizations, which improve the statistics, above and below T_c. Consistent with Fig. 1(c), the superconductivity-induced net magnetic intensity gain appears only above ∼7 meV, forming a resonance at $E_r = 15$ meV.

Figure 2 summarizes the identical scans as that of Fig. 1 at the AF wave vector $\mathbf{Q} = (0.5, 0.5, 1)$ above and below T_c. At $T = 45$ K, we see clear spin anisotropy below $E \approx 7$ meV with $M_{001} > M_{110}$ similar to the spin excitations at $\mathbf{Q} = (0.5, 0.5, 0)$ [Fig. 2(a)]. Upon cooling to 2 K, a large spin gap opens below $E \approx 7$ meV in M_{110}, but there is still magnetic scattering in M_{001} extending to at least 2 meV. Therefore, the low-energy signal above ∼1 meV at $\mathbf{Q} = (0.5, 0.5, 1)$ reported in the earlier unpolarized

neutron measurements [Zhang et al., 2011] are entirely c-axis polarized magnetic scattering. The neutron spin resonance at $E_r = 15$ is isotropic. The temperature difference plots between 2 and 45 K display a broad and narrow peak for M_{001} and M_{110}, respectively [Fig. 2(c)]. Fig. 2(d) shows the sum of SF magnetic scattering below and above T_c. Consistent with unpolarized work [Zhang et al., 2011], we see net intensity gain of the resonance in the superconducting state for energies above $E \approx 7$ meV, different from that of $BaFe_{1.88}Co_{0.12}As_2$ where the magnetic intensity starts to gain above $E = 4$ meV in the superconducting state [Fig. 4(b) in [Steffens et al., 2012]].

To further illustrate the effect of spin anisotropy, we plot in Figs. 3(a)-3(d) the differences of $(M_{001} - M_{110})$ above and below T_c at wave vectors $\mathbf{Q} = (0.5, 0.5, 0)$ and $(0.5, 0.5, 1)$. In the normal state, we see clear magnetic anisotropy with $M_{001} > M_{110}$ for energies below $\sim$7 meV [Figs. 3(a) and 3(c)]. In the superconducting state, the $(M_{001} - M_{110})$ differences reveal similar intensity peaks centered around $\sim$7 meV at $\mathbf{Q} = (0.5, 0.5, 0)$ and $(0.5, 0.5, 1)$, but with a much broader width for $\mathbf{Q} = (0.5, 0.5, 1)$ [Figs. 3(b) and 3(d)]. Since there are essentially no intensity gain in M_{001} across T_c near $\sim$7 meV [Figs. 1(c) and 2(c)], the apparent peaks in $(M_{001} - M_{110})$ arise from different responses of M_{001} and M_{110} across T_c. While the intensity of M_{001} across T_c is suppressed below $\sim$7 meV and enhanced above it, similar cross over energy occurs around 10 meV in M_{110}, thus resulting peaks near 7 meV in $(M_{001} - M_{110})$ at 2 K [Figs. 3(b) and 3(d)]. Therefore, the differences in superconductivity-induced

spin gaps in M_{001} and M_{110} at $\mathbf{Q} = (0.5, 0.5, 0)$ and $(0.5, 0.5, 1)$ are causing peaks in $(M_{001} - M_{110})$.

Finally, to confirm the low-energy spin anisotropy discussed in Figs. 1-3, we show in Figs. 4(a)-4(c) constant-energy scans with three different neutron polarizations at $E = 4$ meV along the $[H, H, 0]$ and $[H, H, 1]$ directions. In the normal state, $\sigma_{xx}^{\mathrm{SF}}$ shows clear peaks at $\mathbf{Q} = (0.5, 0.5, 0)$ and $(0.5, 0.5, 1)$ [Figs. 4(a) and 4(c)]. In both cases, we also find $\sigma_{xx}^{\mathrm{SF}} \geq \sigma_{zz}^{\mathrm{SF}} > \sigma_{yy}^{\mathrm{SF}}$, thus confirming the anisotropic nature of the magnetic scattering with $M_{001} > M_{110}$. In the superconducting state, while $\sigma_{xx}^{\mathrm{SF}}$ and $\sigma_{zz}^{\mathrm{SF}}$ are peaked at $(0.5, 0.5, 1)$, $\sigma_{yy}^{\mathrm{SF}}$ is featureless. These results again confirm the presence of a larger superconductivity-induced spin gap in M_{110} than that in M_{001} [Fig. 2(b)].

6.3 Experimental Results

From Figs. 1-4, we see anisotropic spin susceptibility in both the normal and superconducting state of $Ba_{0.67}K_{0.33}Fe_2As_2$, different from optimally electron-doped $BaFe_{1.88}Co_{0.12}As_2$ where the anisotropy is believed to emerge only with the opening of the superconducting gap [Steffens et al., 2012]. Furthermore, our data reveal that large differences in the superconductivity-induced spin gaps at $\mathbf{Q} = (0.5, 0.5, 0)$ and $(0.5, 0.5, 1)$ [Zhang et al., 2011] arise from the differences in spin gaps of c-axis polarized spin excitations. These results are similar to the previous work on electron-doped $BaFe_{1.9}Ni_{0.1}As_2$ [Lipscombe et al., 2010] and $BaFe_{1.88}Co_{0.12}As_2$

[Steffens et al., 2012], suggesting that the influence of a strong spin anisotropy in undoped parent compound $BaFe_2As_2$ [Qureshi et al., 2012] extends to both optimally electron and hole-doped iron pnictide superconductors. For comparison, we note that spin excitations in superconducting iron chalcogenides are different, having slightly anisotropic resonance with isotropic spin excitations below the resonance [Prokeš et al., 2012; Babkevich et al., 2011].

6.4 Conlusion

In Ref. [Steffens et al., 2012], it was suggested that the observed spin anisotropy in $BaFe_{1.88}Co_{0.12}As_2$ can be understood as a c-axis polarized resonance whose intensity strongly varies with the c-axis wave vector. This is not the case in $Ba_{0.67}K_{0.33}Fe_2As_2$ since we find much weaker c-axis modulation of the magnetic intensity [Zhang et al., 2011]. Therefore, the spin anisotropy seen in optimally electron and hole-doped superconductors is a consequence of these materials being close to the AF ordered parent compound $BaFe_2As_2$, where spin-orbit coupling is expected to be strong [Krüger et al., 2009; Lee et al., 2009; Lv and Phillips, 2011], and is not fundamental to superconductivity of these materials. To understand how spin anisotropy in optimally hole and electron-doped iron pnictide superconductors might be coupled to superconductivity via spin-orbit interaction, we note that hole and electron-doped iron pnictides are multiband superconductors with different superconducting gaps for different orbitals. If c-axis and in-plane spin excitations arise from quasiparticle

excitations of different orbitals between hole and electron Fermi pockets [Zhang et al., 2010], the large differences in superconducting gaps for Fermi surfaces of different orbital characters might induce the observed large spin anisotropy.

Chapter 7

Magnetic Excitations in $Pr_{0.88}LaCe_{0.12}CuO_{4-\delta}$

7.1 Introduction

High-transition-temperature (high-T_c) superconductivity (SC) in cuprates is achieved by either electron or hole doping into the CuO_2 planes of the undoped Mott insulators [Kastner et al., 1998], which exhibit an antiferromagnetic (AF) order below a Néel temperature, and can be described by a spin-$\frac{1}{2}$ AF Heisenberg model [Manousakis, 1991]. Due to the proximity of the AF order and SC, magnetism is believed to play a vital role in the mechanism of high-T_c SC [Scalapino, 1999]. In the undoped state, the parent compound is an AF Mott insulator driven by superexchange[Anderson, 1987].

The most studied parent compound of cuprates are La_2CuO_4, Nd_2CuO_4, and Pr_2CuO_4. While T structured La_2CuO_4 is usually hole doped with Sr or Ba, the T′ Nd_2CuO_4 and Pr_2CuO_4 is typically electron doped with Ce in order to induce SC. These less complicated undoped systems can provide valuable information on which Hamiltonians best quantitatively describe the cuprates. Of these parent insulators, La_2CuO_4 is the most thoroughly studied [Bourges et al., 1997; Hayden et al., 1991; Coldea et al., 2001; Headings et al., 2010]. Taking account only a nearest-neighbor spin (S= $\frac{1}{2}$), the conventional spin wave Hamiltonian, $H = \sum_{ij} JS_i \cdot S_j$, yields $J = 136 \pm 5meV$ for La_2CuO_4 [Hayden et al., 1991]. A decade later, [Coldea et al., 2001] demonstrated that the previous nearest-neighbor-only Heisenberg model must be supplemented by a number of additional terms. Almost another decade later, [Headings et al., 2010] found that while the lower energy excitations are well described by spin-wave theory, the high-energy spin waves are strongly damped near the $(1/2, 0)$ and merge into a momentum dependent continuum, which indicates the decay of spin waves into other exotic excitations, possibly unbound spinon pairs. Nd_2CuO_4 and Pr_2CuO_4 are less studied partly due to the existing of multiple strong crystal field excitations arising from the Nd^{3+} and Pr^{3+} ions, especially near the top of the band [Boothroyd et al., 1992].

Upon hole doping, spin excitations are significantly modified by the presence of charge carriers. The spin wave of the parent compound evolves into an "hour-glass" dispersion. The dispersion also slightly softens with doping, which is characterized by a dropping in its effective exchange constant J. For lightly-doped $La_{2-x}Sr_xCuO_4$

(x= 0.005), an exchange coupling of $J = 108 \pm 6$ meV was found, and there is a significant spectra weight redistribution to the low energy range, which then decreases rapidly with increasing energy [Goka et al., 2003]. For underdoped $La_{2-x}Sr_xCuO_4$ (x= 0.085), $J = 87 \pm 4$ meV [Lipscombe et al., 2009], which is substantially smaller than La_2CuO_4 [Headings et al., 2010]. Also, the enhanced low energy weight in x= 0.005 is suppressed upon entering the SC region. For overdoped $La_{2-x}Sr_xCuO_4$ (x= $0.25, 0.30$), $\chi''(\omega)$ is severely diminished over the whole energy range [Wakimoto et al., 2007]. Therefore, the role of hole doping in La_2CuO_4 is to cause a softening of the dispersion, and a gradual decrease of the magnetic moment as they move away from the AF phase. Similar results can also be found in $YBa_2Cu_3O_{6+x}$ [Kivelson et al., 2003; Regnault et al., 1995; Reznik et al., 2008], suggesting that this is a universal trend in hole-doped cuprates.

There are recently intense studies on hole-doped cuprates using the resonant magnetic x-ray scattering (RIXS) technique, which can detect momentum and energy resolved information on spin and charge dynamics in a wide energymomentum range not accessible by neutrons [Hill et al., 2008; Braicovich et al., 2010; Ellis et al., 2010; Le Tacon et al., 2011; Dean et al., 2013]. The evolution of the magnetic excitations in $La_{2-x}Sr_xCuO_4$ across the entire phase diagram are probed, and spin-wave-like dispersive magnetic excitations are found around ~ 300 meV for all doping levels, with spectral weights comparable to the undoped parent compounds. These excitations broaden with doping, but persist with a similar dispersion and comparable intensity all the way to the non-SC, heavily overdoped metallic phase. This indicates that

the destruction of SC with overdoping does not originate from the disappearance or softening of magnetic excitations. Other factors like the influence of the low-energy magnetic excitations, which are known to change dramatically in the overdoped cuprates, or the redistribution of spectral weight may instead play a role in SC.

While the evolution of spin excitations in hole-doped superconductors has become increasingly clear, it is important to determine the evolution of spin excitations in electron-doped materials, as the particle-hole symmetry between doping with electrons or holes has important theoretical implications as most models implicitly assume symmetry. For underdoped $Pr_{0.88}LaCe_{0.12}CuO_{4-\delta}$ (T_C = 21K, T_N = 40K), [Wilson et al., 2006b] found J= 162$\pm$13 meV, which is larger than both La_2CuO_4 and Pr_2CuO_4. They find that the effect of electron doping into the AF insulating PLCCO is to cause a wave vector broadening in the low-energy (E $<$ 80 meV) commensurate magnetic excitations at (0.5, 0.5). And at high energies (E $>$ 100 meV), the excitations are spin-wave-like rings, but with a dispersion steeper than that of the undoped Pr_2CuO_4 [Bourges et al., 1997], and a significant reduction in the spectral weight of the local dynamical spin susceptibility $\chi''(\omega)$. However, this result was challenged by[Fujita et al., 2006], who did not observe any spin-wave-like dispersion up to 180 meV in optimally electron-doped $Pr_{0.89}LaCe_{0.11}CuO_{4-\delta}$ (T_C = 25.5K). In a recent RIXS experiment [Lee et al., 2013] on $Nd_{2-x}Ce_xCuO_4$ (NCCO) confirms the hardening of the dispersion upon electron doping found by Wilson, as well as

a highly dispersive mode in superconducting NCCO that is undetected in the hole-doped compounds. This hardening of magnetic excitations found in electron doped PLCCO and NCCO is in stark contrast with hole-doped cuprates.

Electron-doped cuprates differ from hole-doped cuprates in that the as-grown compounds are non-SC, and SC can only be achieved after reducing a tiny amount of oxygen[Takagi et al., 1989; Tokura et al., 1989]. This reduction has dramatic consequences for its conducting and magnetic properties, changing the electron-doped cuprates from AF to coexistence of AF and SC until optimal SC (Fig.1(a)). By far, the comparisons in electron-doped cuprates are all among different doping levels. It will be especially beneficial to study the magnetic excitation evolutions in electron-doped cuprates with the same doping level but different conducting and magnetic properties controlled by annealing, to see how the onset of SC by annealing will affect the dispersion and overall magnetic excitation spectra.

In this Chapter, we investigate the magnetic excitations of as-grown ($T_C = 0$K, $T_N = 210$K), and optimally annealed SC ($T_C = 24$K, $T_N = 0$K) $Pr_{0.89}LaCe_{0.11}CuO_{4-\delta}$ (Fig.1(c)) for energies from 4 meV to 300 meV, and compared the results with previous results on less annealed($T_C = 21$K, $T_N = 40$K) $Pr_{0.89}LaCe_{0.11}CuO_{4-\delta}$.

7.2 Experimental details

Large single crystals of as-grown PLCCO were grown using a floating zone furnace. To obtain superconductivity, the as grown samples are annealed in vacuum, and a

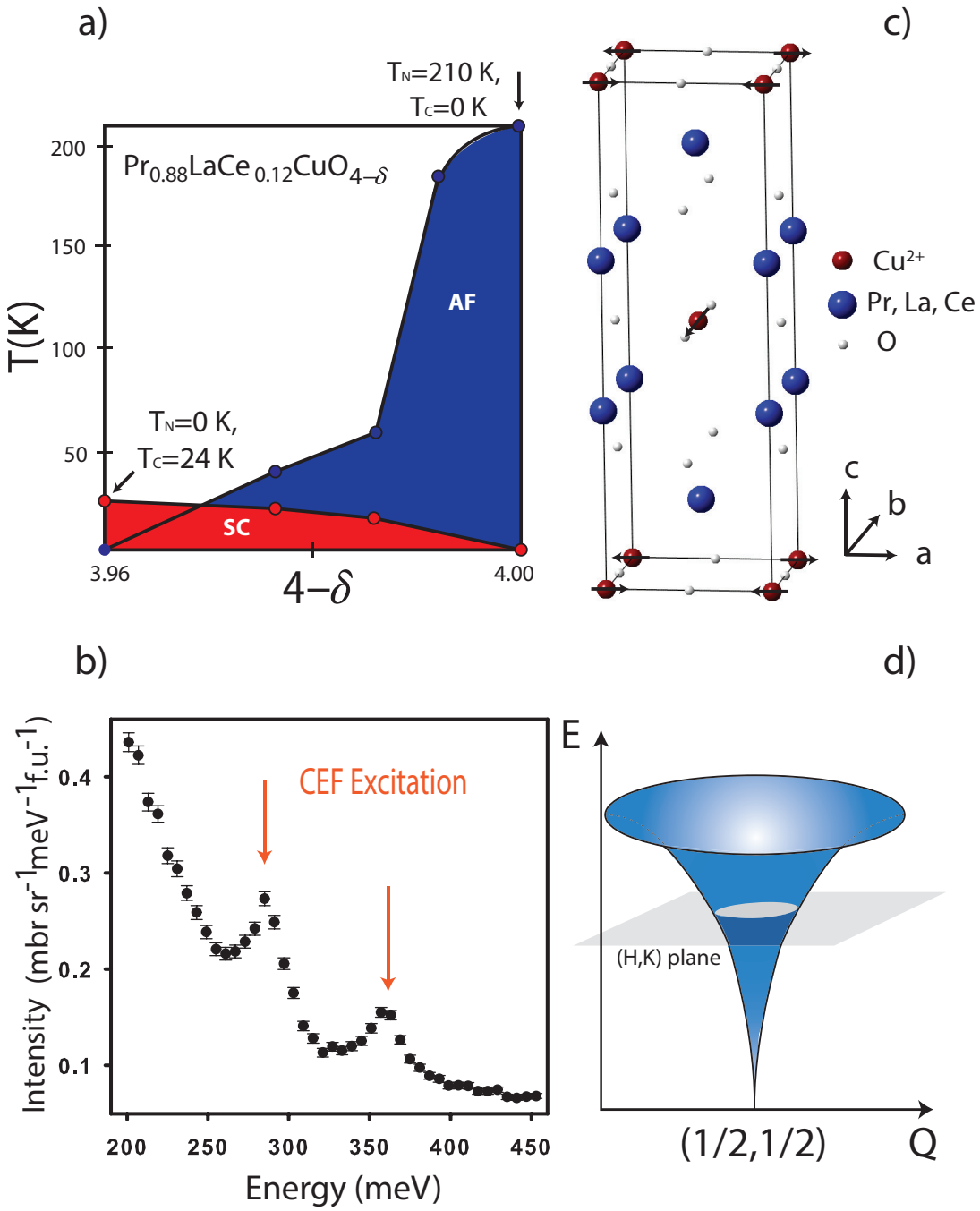

Figure 7.1: (a) Phase diagram of electron doped PLCCO. (b) Energy scans showing two crystal field levels in PLCCO. (c) antiferromagnetic spin structure of PLCCO with Cu spin ordering. (d) Pictorial representation of the dispersions of the spin excitations in a classical Heisenberg Hamiltonian.

T_C of 24K was achieved. For this experiment, we coaligned $\sim$ 25 g single crystals of as-grown and $\sim$ 20 optimal doped PLCCO in the (H, H, L) scattering plane (with mosaicity 3° at full width half maximum) in a tetragonal unit cell (space group $I4/mmm$, $a = b = 3.98$ Å, and $c = 12.27$ Å). In this notation, the vector $\mathbf{Q}$ in three-dimensional reciprocal space in Å^{-1} is defined as $\mathbf{Q} = H\mathbf{a}^* + K\mathbf{b}^* + L\mathbf{c}^*$, where H, K, and L are Miller indices and $\mathbf{a}^* = \hat{\mathbf{a}}2\pi/a, \mathbf{b}^* = \hat{\mathbf{b}}2\pi/b, \mathbf{c}^* = \hat{\mathbf{c}}2\pi/c$ are reciprocal lattice vectors.

The experiments were carried out on the MAPS and MERLIN time-of-flight chopper spectrometer at the Rutherford-Appleton Laboratory, UK. The incident beam energies were $E_i = 40, 115, 200, 400, 591$ meV for the parent sample, and $E_i = 30, 200, 400$ meV for the superconducting sample, and with E_i parallel to the c-axis. The data are normalized to absolute units using a vanadium standard, which may have a systematic error up to 20% due to differences in neutron illumination of vanadium and sample, and time-of-flight instruments.

Figure 2 shows two-dimensional constant-energy (E) images of neutron scattering intensity $S(Q, \omega)$ centered about $(0.5, 0.5)$ at $T = 7K$ in unit of $mbarns \cdot s.r.^{-1} \cdot meV^{-1} \cdot f.u.^{-1}$, without any background subtraction for as-grown (Fig.2(a)-2(f)), optimal superconducting PLCCO (Fig.2(g)-(l)). For as-grown PLCCO, at the lowest energy ($\hbar = 4 \pm 1$ meV) probed (Fig.2(a)), the scattering consists of a strong peak at $(0.5, 0.5)$ with some phonon contamination at larger wave vectors. Upon increasing energy, the peak broadens in width, and weakens in intensity (Fig. 2(b)). With

further increase in energy to $\hbar\omega = 130 \pm 10$ meV, the scattering becomes a spin-wave-like ring (Figs.2(c) - 2(e)). With more increasing energy, the ring continues to disperse outward (Fig.2(f))until magnetic scattering is no longer discernible above 240 meV due to strong crystalline electric field (CEF) excitations arising from the Pr^{+3} ions in PLCCO between 250 meV and 360 meV (Fig.1(b))[Boothroyd et al., 1992]. For optimal superconducting PLCCO, the evolution of the excitations follows a similar trend as in the as-grown sample, a strong peak at $(0.5, 0.5)$ (Fig.2(g)); gradual broadening of the peak at increased energy (Fig.3(h)-Fig.3(k)) until disappearance of noticeable magnetic signals (Fig.3(l)). Based on their intensity color bar, it is also obvious that the magnetic excitations in SC PLCCO are much weaker than in the AF as-grown PLCCO.

To compare quantitatively the as-grown and superconducting samples, we show in Figures 3(a)-10(f) constant-E cuts at different energies along the $[-H, H]$ direction for spin excitations in both as grown PLCCO and optimal superconducting PLCCO, as both measurements were taken in absolute units. As the energy transfer increases, spin excitations in both compounds become broader in momentum space and weaker in intensity. Different with what we find in Chapter 4 [Liu et al., 2012a], the spin excitation in as-grown PLCCO is higher in intensity and narrower in width than its superconducting counterpart throughout the whole energy spectra, until the magnetic scattering is no longer discernible.

Figure 4(a) summarizes the dispersion of spin excitations determined from the cuts in Figs. 3(a) 3(f) with data from [Wilson et al., 2006a] overplotted. To estimate

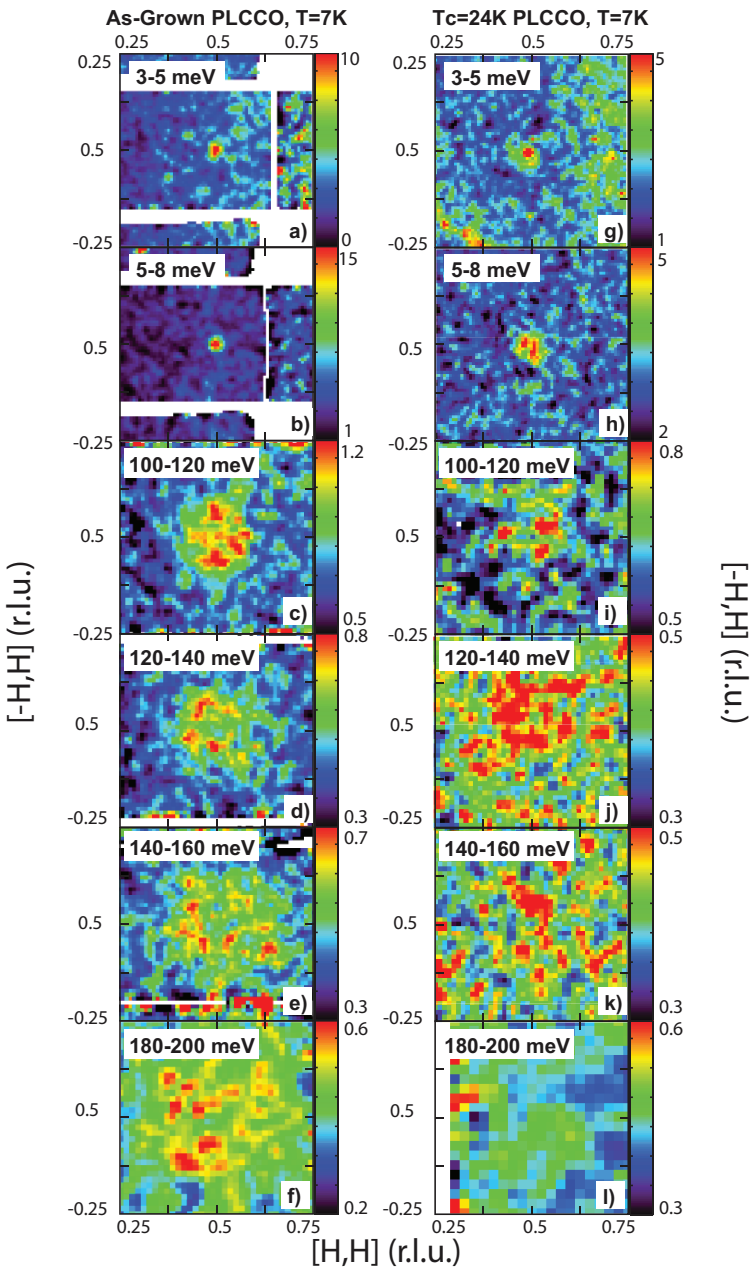

Figure 7.2: Constant-energy slices through the magnetic excitations of as grown PLCCO and optimal superconducting PLCCO (T_C = 24K) at different energies. The color bars represent the vanadium normalized absolute spin excitation intensity in the units of mbarn/sr/meV/f.u.. Two dimensional images of spin excitations at (a) $E = 4 \pm 1$ meV, (b) 6.5 ± 1.5 meV, (c) 110 ± 10 meV, (d) 130 ± 10 meV, (e) 150 ± 10 meV, (f) 190 ± 10 meV.

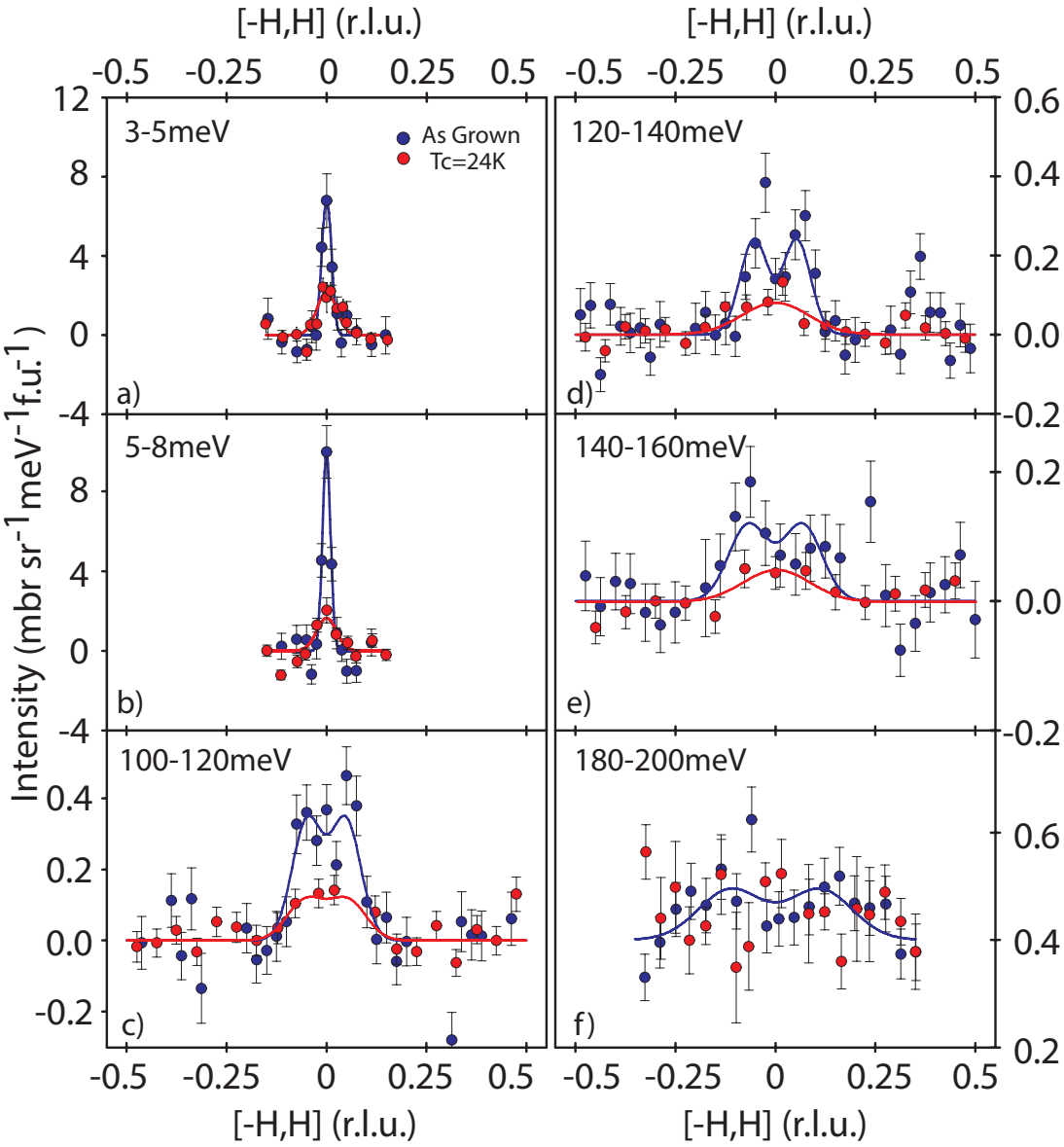

Figure 7.3: Constant-energy cuts of the spin excitation dispersion as a function of increasing energy along the $[-H, H]$ direction for both as-grown PLCCO (filled blue circles) and optimal superconducting PLCCO (filled red circles) Constant-energy cut along the $[-H, H]$ direction at (a) $E = 4 \pm 1$ meV, (b) 6.5 ± 1.5 meV, (c) 110 ± 10 meV, (d) 130 ± 10 meV, (e) 150 ± 10 meV, (f) 190 ± 10 meV.

the strength of the magnetic exchange coupling in as-grown PLCCO, we consider a two-dimensional AF Heisenberg Hamiltonian with nearest coupling (Fig.1(d)). The black solid line is with J_1 = 162meV. The solid lines represent the FWHM of a Gaussian fit with the instrument resolution deconvoluted. At low energies ($\hbar\omega < 10$ meV) (The enlarged part of the figure is shown as inset), the widths of all three compounds are considerably broader than those predicted by the linear spin-wave theory. The as-grown PLCCO has the narrowest width, and as T_C increases, the width also becomes broader. At intermediate energies ($\hbar\omega < 100$ meV), the observed scattering is still broader than spin wave, and the as-grown sample has only a slightly smaller width than the T_C = 21K PLCCO. At high energies ($\hbar\omega > 100$ meV), the calculated spin wave dispersion coincides fairly well with the data. The dispersions of as-grown and T_C = 21K PLCCO are indistinguishable, while T_C = 24K PLCCO is clearly softened. This is different from previous RIXS results on NCCO[Lee et al., 2013], where the SC sample has a much stiffer dispersion than the AF NCCO.

In addition to determining the dispersion of spin excitations in PLCCO, the absolute spin susceptibility $\chi''(Q,\omega)$ measurements in Fig.2 also allow us to calculate the energy dependence of the local susceptibility $\chi''(\omega)$. Fig.4(b) shows how $\chi''(\omega)$ varies as a function of $\hbar\omega$ for both as grown PLCCO and optimal superconducting PLCCO, as well as previous results of 12% PLCCO with $T_C = 21K$ [Wilson et al., 2006b] and 11% PLCCO with $T_C = 25.5K$ [Fujita et al., 2006]. While Energy dependence of $\chi''(\omega)$ remains relatively the same for the three superconducting

samples despite different T_C, the spectra is considerably larger throughout the whole zone for as-grown PLCCO, which is similar to hole-doped materials.

7.3 Conclusion

In summary, We use high-resolution inelastic neutron scattering to study the low-temperature magnetic excitations of as-grown 12% electron- doped PLCCO, and its annealed optimal superconducting PLCCO, in an energy range up to 250 meV. As energy increases, the magnetic signal remarkably loses its intensity and finally disappears. For energy below 100 meV, the dispersions are substantially wider than spin wave prediction, and the role of annealing or the onset of SC is to cause a broadening of spin excitations. At energies above 100meV, where spin wave theory is a good fit, the appearance of SC softens the dispersion slightly, which is consistent with hole-doped cuprates, but different from previous results in electron-doped cuprates.

Also, given the recent success of RIXS in discovering new collective excitations ~ 1 eV in cuprates, and that we already know the absolute intensity of spin excitations in both as-grown and superconducting PLCCO throughout the Brillouin zone, it is worthwhile to conduct similar measurements using RIXS and compare the results with INS. Since RIXS can detect both spin and orbital excitations in energy and momentum spaces, comparing INS and RIXS on the same sample can provide important information on the orbital contribution to spin excitations in cuprates, and the role of annealing in SC.

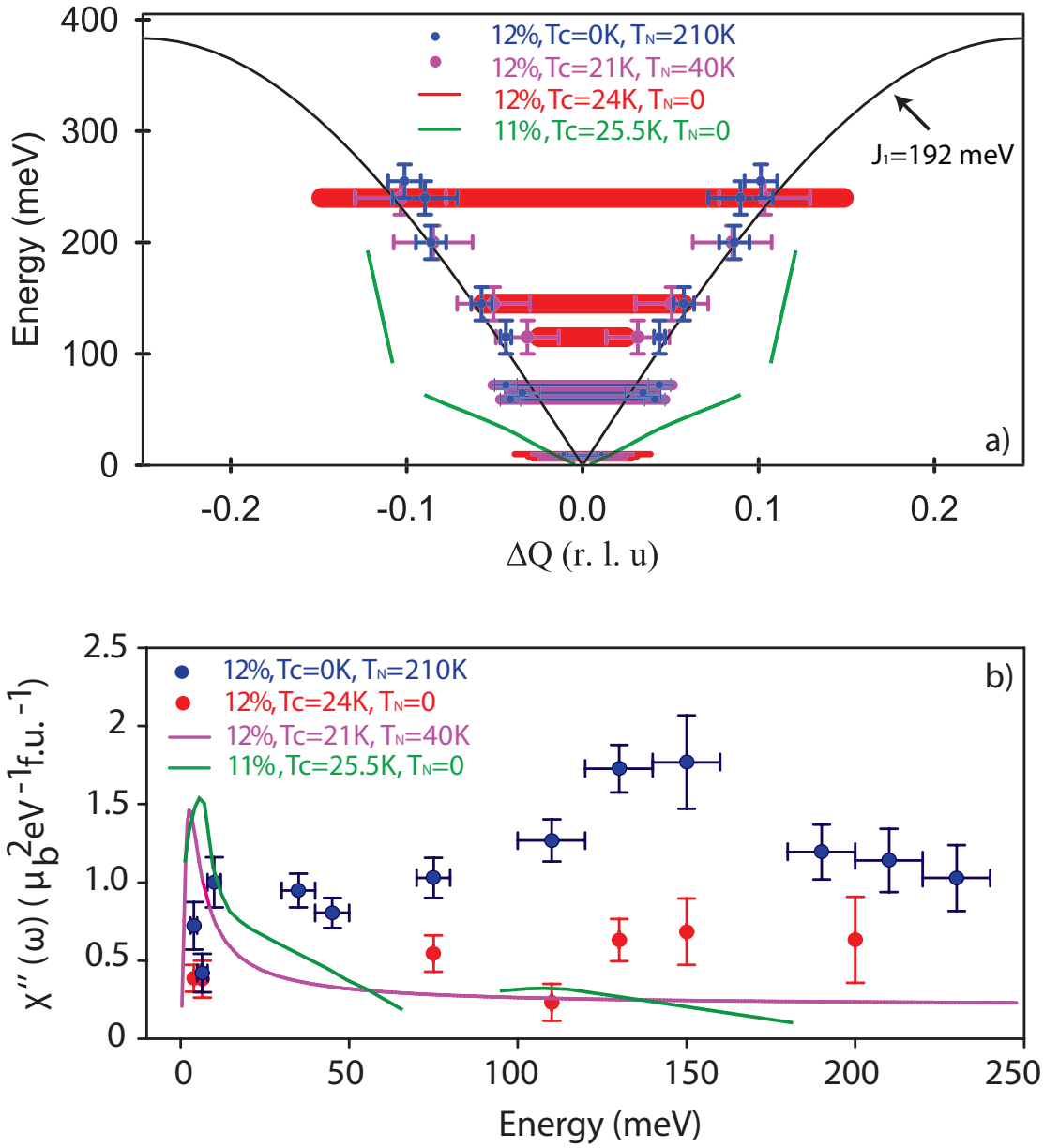

Figure 7.4: (a) The dispersion of spin excitations in PLCCO. Thick solid thick lines denote peaks centerd around (0.5, 0.5) and represent the FWHM of a Gaussian fit with the instrument resolution deconvoluted. Black solid line shows dispersion from linear spin wave fit. (b)Energy dependence of $\chi''(\omega)$ for as grown PLCCO (filled blue circles) and optimal superconducting PLCCO (filled red circles) at base temperature. The vertical error bars indicate the statistical errors of one standard deviation. The horizontal error bars indicate energy integration range. The magenta solid line is data from PLCCO with T_C=21K [Wilson et al., 2006b]. The green solid line is data from 11% PLCCO with T_C=25.5K [Fujita et al., 2006].

Bibliography

Anderson, P. W. (1987). The resonating valence bond state in La2CuO4 and superconductivity. *Science*, 235(4793):1196–1198.

Babkevich, P., Roessli, B., Gvasaliya, S. N., Regnault, L. P., Freeman, P. G., Pomjakushina, E., Conder, K., and Boothroyd, A. T. (2011). Spin anisotropy of the resonance peak in superconducting $FeSe_{0.5}Te_{0.5}$. *Physical Review B*, 83(18):180506.

Basov, D. N. and Chubukov, A. V. (2011). Manifesto for a higher Tc. *Nature Physics*, 7(4):272–276.

Bewley, R. I., Eccleston, R. S., McEwen, K. A., Hayden, S. M., Dove, M. T., Bennington, S. M., Treadgold, J. R., and Coleman, R. (2006). MERLIN, a new high count rate spectrometer at ISIS. *Physica B: Condensed Matter*, 385:1029–1031.

Boothroyd, A., Doyle, S., Paul, D., and Osborn, R. (1992). Crystal-field excitations in Nd_2CuO_4, Pr_2CuO_4, and related n -type superconductors. *Physical Review B*, 45(17):10075–10086.

Bourges, P., Casalta, H., Ivanov, A., and Petitgrand, D. (1997). Superexchange Coupling and Spin Susceptibility Spectral Weight in Undoped Monolayer Cuprates. *Physical Review Letters*, 79(24):4906–4909.

Braicovich, L., van den Brink, J., Bisogni, V., Sala, M. M., Ament, L. J. P., Brookes, N. B., De Luca, G. M., Salluzzo, M., Schmitt, T., Strocov, V. N., and Ghiringhelli, G. (2010). Magnetic Excitations and Phase Separation in the Underdoped $La_{2-x}Sr_xCuO_4$ Superconductor Measured by Resonant Inelastic X-Ray Scattering. *Physical Review Letters*, 104(7):077002.

Bud'ko, S. L., Ni, N., and Canfield, P. C. (2009). Jump in specific heat at the superconducting transition temperature in $Ba(Fe_{1x}Co_x)_2As_2$and $Ba(Fe_{1x}Ni_x)_2As_2$single crystals. *Physical Review B*, 79(22):220516.

Chen, Y., Lu, X., Wang, M., Luo, H., and Li, S. (2011). Systematic growth of $BaFe_{2-x}Ni_xAs_2$ large crystals. *Superconductor Science and Technology*, 24(6):065004.

Chi, S., Schneidewind, A., Zhao, J., Harriger, L., Li, L., Luo, Y., Cao, G., Xu, Z., Loewenhaupt, M., Hu, J., and Dai, P. (2009). Inelastic Neutron-Scattering Measurements of a Three-Dimensional Spin Resonance in the FeAs-Based $BaFe_{1.9}Ni_{0.1}As_2$ Superconductor. *Physical Review Letters*, 102(10):107006.

Christianson, A. D., Goremychkin, E. A., Osborn, R., Rosenkranz, S., Lumsden, M. D., Malliakas, C. D., Todorov, I. S., Claus, H., Chung, D. Y., Kanatzidis, M. G., Bewley, R. I., and Guidi, T. (2008). Unconventional superconductivity in Ba0.6K0.4Fe2As2 from inelastic neutron scattering. *Nature*, 456(7224):930–932.

Coldea, R., Hayden, S. M., Aeppli, G., Perring, T. G., Frost, C. D., Mason, T. E., Cheong, S. W., and Fisk, Z. (2001). Spin Waves and Electronic Interactions in La_2CuO_4. *Physical Review Letters*, 86(23):5377–5380.

Cvetkovic, V. and Tesanovic, Z. (2009). Multiband magnetism and superconductivity in Fe-based compounds. *Reports on Progress in Physics*, 85(3):37002.

Dai, P., Hu, J., and Dagotto, E. (2012). Magnetism and its microscopic origin in iron-based high-temperature superconductors. *Nature*, 8(10):709–718.

Dai, P., Mook, H., Hunt, R., and Doğan, F. (2001). Evolution of the resonance and incommensurate spin fluctuations in superconducting $YBa_2Cu_3O_{6+x}$. *Physical Review B*, 63(5):054525.

Dai, P., Mook, H. A., Aeppli, G., Hayden, S. M., and Doğan, F. (2000). Resonance as a measure of pairing correlations in the high-T c superconductor YBa2Cu3O6.6. *Nature*, 406(6799):965–968.

de la Cruz, C., Huang, Q., Lynn, J. W., Li, J., II, W. R., Zarestky, J. L., Mook, H. A., Chen, G. F., Luo, J. L., Wang, N. L., and Dai, P. (2008a). Magnetic order close to superconductivity in the iron-based layered LaO1-xFxFeAs systems. *Nature*, 453(7197):899–902.

de la Cruz, C., Huang, Q., Lynn, J. W., Li, J., Ratcliff, II, W., Zarestky, J. L., Mook, H. A., Chen, G. F., Luo, J. L., Wang, N. L., and Dai, P. (2008b). Magnetic

order close to superconductivity in the iron-based layered LaO1-xFxFeAs systems. *Nature*, 453(7197):899–902.

Dean, M. P. M., Dellea, G., Springell, R. S., Yakhou-Harris, F., Kummer, K., Brookes, N. B., Liu, X., Sun, Y.-J., Strle, J., Schmitt, T., Braicovich, L., Ghiringhelli, G., Božović, I., and Hill, J. P. (2013). Persistence of magnetic excitations in La2xSrxCuO4 from the undoped insulator to the heavily overdoped non-superconducting metal. *Nature Materials*, 12(11):1019–1023.

Dong, J., Zhang, H. J., Xu, G., Li, Z., Li, G., Hu, W. Z., Wu, D., Chen, G. F., Dai, X., Luo, J. L., Fang, Z., and Wang, N. L. (2008). Competing orders and spin-density-wave instability in $La(O_{1-x}F_x)FeAs$. *Reports on Progress in Physics*, 83(2):27006.

Ellis, D. S., Kim, J., Hill, J. P., Wakimoto, S., Birgeneau, R. J., Shvyd'ko, Y., Casa, D., Gog, T., Ishii, K., Ikeuchi, K., Paramekanti, A., and Kim, Y.-J. (2010). Magnetic nature of the 500 meV peak in $La_{2x}Sr_xCuO_4$ observed with resonant inelastic x-ray scattering at the CuK-edge. *Physical Review B*, 81(8):085124.

Eschrig, M. (2006). The effect of collective spin-1 excitations on electronic spectra in high- T csuperconductors. *Advances in Physics*, 55(1-2):47–183.

Fawcett, E. (1988). Spin-density-wave antiferromagnetism in chromium. *Reviews of Modern Physics*, 60(1):209–283.

Fong, H., Keimer, B., Reznik, D., Milius, D., and Aksay, I. (1996). Polarized and unpolarized neutron-scattering study of the dynamical spin susceptibility of $YBa_2Cu_3O_7$. *Physical Review B*, 54(9):6708–6720.

Fujita, M., Matsuda, M., Fåk, B., Frost, C. D., and Yamada, K. (2006). Novel Spin Excitations in Optimally Electron-Doped Pr 0.89LaCe 0.11CuO 4. *Journal of the Physical Society of Japan*, 75(9):093704.

Goka, H., Kuroshima, S.-i., Fujita, M., Yamada, K., Hiraka, H., Endoh, Y., and Frost, C. D. (2003). Magnetic excitations in the spin-glass phase of La2xSrxCuO4. *Physica C: Superconductivity*, 388-389:239–240.

Goldman, A., Argyriou, D., Ouladdiaf, B., Chatterji, T., Kreyssig, A., Nandi, S., Ni, N., Bud'ko, S., Canfield, P., and McQueeney, R. (2008). Lattice and magnetic instabilities in CaFe2As2: A single-crystal neutron diffraction study. *Physical Review B*, 78(10):100506.

Graser, S., Kemper, A. F., Maier, T. A., Cheng, H. P., Hirschfeld, P. J., and Scalapino, D. J. (2010). Spin fluctuations and superconductivity in a three-dimensional tight-binding model for $BaFe_2As_2$. *Physical Review B*, 81(21):214503.

Harriger, L. W., Luo, H. Q., Liu, M. S., Frost, C., Hu, J. P., Norman, M. R., and Dai, P. (2011). Nematic spin fluid in the tetragonal phase of $BaFe_2As_2$. *Physical Review B*, 84(5):054544.

Haule, K. (2007). Quantum Monte Carlo impurity solver for cluster dynamical mean-field theory and electronic structure calculations with adjustable cluster base. *Physical Review B*, 75(15):155113.

Haule, K., Shim, J. H., and Kotliar, G. (2008). Correlated Electronic Structure of $LaO_{1-x}F_xFeAs$. *Physical Review Letters*, 100(22):226402.

Haule, K., Yee, C.-H., and Kim, K. (2010). Dynamical mean-field theory within the full-potential methods: Electronic structure of $CeIrIn_5$, $CeCoIn_5$, and $CeRhIn_5$. *Physical Review B*, 81(19):195107.

Hayden, S., Aeppli, G., Mook, H., Perring, T., Mason, T., Cheong, S. W., and Fisk, Z. (1996). Comparison of the High-Frequency Magnetic Fluctuations in Insulating and Superconducting $La_{2-x}Sr_xCuO_4$. *Physical Review Letters*, 76(8):1344–1347.

Hayden, S., Aeppli, G., Osborn, R., Taylor, A., Perring, T., Cheong, S. W., and Fisk, Z. (1991). High-energy spin waves in La_2CuO_4. *Physical Review Letters*, 67(25):3622–3625.

Headings, N. S., Hayden, S. M., Coldea, R., and Perring, T. G. (2010). Anomalous High-Energy Spin Excitations in the High-T_c Superconductor-Parent Antiferromagnet La_2CuO_4. *Physical Review Letters*, 105(24):247001.

Headings, N. S., Hayden, S. M., Kulda, J., Babu, N. H., and Cardwell, D. A. (2011). Spin anisotropy of the magnetic excitations in the normal and superconducting

states of optimally doped $YBa_2Cu_3O_{6.9}$ studied by polarized neutron spectroscopy. *Physical Review B*, 84(10):104513.

Hill, J., Blumberg, G., Kim, Y.-J., Ellis, D., Wakimoto, S., Birgeneau, R., Komiya, S., Ando, Y., Liang, B., Greene, R., Casa, D., and Gog, T. (2008). Observation of a 500 meV Collective Mode in La2-xSrxCuO4 and Nd2CuO4 Using Resonant Inelastic X-Ray Scattering. *Physical Review Letters*, 100(9):097001.

Huang, Q., Qiu, Y., Bao, W., Green, M. A., Lynn, J. W., Gasparovic, Y. C., Wu, T., Wu, G., and Chen, X. H. (2008). Neutron-Diffraction Measurements of Magnetic Order and a Structural Transition in the Parent $BaFe_2As_2$ Compound of FeAs-Based High-Temperature Superconductors. *Physical Review Letters*, 101(25):257003.

Inosov, D. S., Park, J. T., Bourges, P., Sun, D. L., Sidis, Y., Schneidewind, A., Hradil, K., Haug, D., Lin, C. T., Keimer, B., and Hinkov, V. (2009). Normal-state spin dynamics and temperature-dependent spin-resonance energy in optimally doped BaFe1.85Co0.15As2. *Nature Physics*, 6(3):178–181.

Kamihara, Y., Watanabe, T., Hirano, M., and Hosono, H. (2008). Iron-Based Layered Superconductor La[$O_{1-x}F_x$]FeAs (x= 0.050.12) with Tc= 26 K. *Journal of the American Chemical Society*, 130(11):3296–3297.

Kastner, M., Birgeneau, R., Shirane, G., and Endoh, Y. (1998). Magnetic, transport, and optical properties of monolayer copper oxides. *Reviews of Modern Physics*,

70(3):897–928.

Kivelson, S. A., Bindloss, I. P., Oganesyan, V., Tranquada, J. M., Kapitulnik, A., and Howald, C. (2003). How to detect fluctuating stripes in the high-temperature superconductors. *Reviews of Modern Physics*, 75(4):1201–1241.

Korshunov, M. and Eremin, I. (2008). Theory of magnetic excitations in iron-based layered superconductors. *Physical Review B*, 78(14):140509.

Krüger, F., Kumar, S., Zaanen, J., and van den Brink, J. (2009). Spin-orbital frustrations and anomalous metallic state in iron-pnictide superconductors. *Physical Review B*, 79(5):054504.

Kutepov, A., Haule, K., Savrasov, S. Y., and Kotliar, G. (2010). Self-consistent GW determination of the interaction strength: Application to the iron arsenide superconductors. *Physical Review B*, 82(4):045105.

Le Tacon, M., Ghiringhelli, G., Chaloupka, J., Sala, M. M., Hinkov, V., Haverkort, M. W., Minola, M., Bakr, M., Zhou, K. J., Blanco-Canosa, S., Monney, C., Song, Y. T., Sun, G. L., Lin, C. T., De Luca, G. M., Salluzzo, M., Khaliullin, G., Schmitt, T., Braicovich, L., and Keimer, B. (2011). Intense paramagnon excitations in a large family of high-temperature superconductors. *Nature Physics*, 7(9):725–730.

Lee, C.-C., Yin, W.-G., and Ku, W. (2009). Ferro-Orbital Order and Strong Magnetic Anisotropy in the Parent Compounds of Iron-Pnictide Superconductors. *Physical Review Letters*, 103(26):267001.

Lee, P. A. and Wen, X.-G. (2006). Doping a Mott insulator: Physics of high-temperature superconductivity. *Reviews of Modern Physics*, 78(1):17–85.

Lee, W. S., Lee, J. J., Nowadnick, E. A., Tabis, W., Huang, S. W., Strocov, V. N., Motoyama, E. M., Yu, G., Moritz, B., Greven, M., Schmitt, T., Shen, Z. X., and Devereaux, T. P. (2013). Asymmetry of collective excitations in electron and hole doped cuprate superconductors. *Arxiv*.

Lester, C., Chu, J.-H., Analytis, J., Capelli, S. C., Erickson, A., Condron, C., Toney, M., Fisher, I., and Hayden, S. (2009). Neutron scattering study of the interplay between structure and magnetism in $Ba(Fe_{1x}Co_x)_2As_2$. *Physical Review B*, 79(14):144523.

Lester, C., Chu, J.-H., Analytis, J. G., Perring, T. G., Fisher, I. R., and Hayden, S. M. (2010). Dispersive spin fluctuations in the nearly optimally doped superconductor $Ba(Fe_{1x}Co_x)_2As_2$ (x=0.065). *Physical Review B*, 81(6):064505.

Li, H. F., Broholm, C., Vaknin, D., Fernandes, R. M., Abernathy, D. L., Stone, M. B., Pratt, D. K., Tian, W., Qiu, Y., Ni, N., Diallo, S. O., Zarestky, J. L., Bud'ko, S. L., Canfield, P. C., and McQueeney, R. J. (2010). Anisotropic and quasipropagating spin excitations in superconducting $Ba(Fe_{0.926}Co_{0.074})_2As_2$. *Physical Review B*, 82(14):140503.

Li, L. J., Luo, Y. K., Wang, Q. B., Chen, H., Ren, Z., Tao, Q., Li, Y. K., Lin, X., He, M., Zhu, Z. W., Cao, G. H., and Xu, Z. A. (2009a). Superconductivity induced by

Ni doping in BaFe2As2single crystals. *New Journal of Physics*, 11(2):025008.

Li, S., Chen, Y., Chang, S., Lynn, J., Li, L., Luo, Y., Cao, G., Xu, Z., and Dai, P. (2009b). Spin gap and magnetic resonance in superconducting BaFe1.9Ni0.1As2. *Physical Review B*, 79(17):174527.

Li, S., Lu, X., Wang, M., Luo, H.-q., Wang, M., Zhang, C., Faulhaber, E., Regnault, L.-P., Singh, D., and Dai, P. (2011). Effect of the in-plane magnetic field on the neutron spin resonance in optimally doped $FeSe_{0.4}Te_{0.6}$ and $BaFe_{1.9}Ni_{0.1}As_2$ superconductors. *Physical Review B*, 84(2):024518.

Lipscombe, O., Harriger, L., Freeman, P., Enderle, M., Zhang, C., Wang, M., Egami, T., Hu, J., Xiang, T., Norman, M., and Dai, P. (2010). Anisotropic neutron spin resonance in superconducting $BaFe_{1.9}Ni_{0.1}As_2$. *Physical Review B*, 82(6):064515.

Lipscombe, O., Vignolle, B., Perring, T., Frost, C., and Hayden, S. (2009). Emergence of Coherent Magnetic Excitations in the High Temperature Underdoped La2-xSrxCuO4 Superconductor at Low Temperatures. *Physical Review Letters*, 102(16):167002.

Liu, M., Harriger, L. W., Luo, H., Wang, M., Ewings, R. A., Guidi, T., Park, H., Haule, K., Kotliar, G., Hayden, S. M., and Dai, P. (2012a). Nature of magnetic excitations in superconducting $BaFe_{1.9}Ni_{0.1}As_2$. *Nature*, 8(5):376–381.

Liu, M., Lester, C., Kulda, J., Lu, X., Luo, H., Wang, M., Hayden, S., and Dai, P. (2012b). Polarized neutron scattering studies of magnetic excitations in electron-overdoped superconducting $BaFe_{1.85}Ni_{0.15}As_2$. *Physical Review B*, 85(21):214516.

Lorenzana, J., Seibold, G., and Coldea, R. (2005). Sum rules and missing spectral weight in magnetic neutron scattering in the cuprates. *Physical Review B*, 72(22):224511.

Lumsden, M., Christianson, A., Parshall, D., Stone, M., Nagler, S., MacDougall, G., Mook, H., Lokshin, K., Egami, T., Abernathy, D., Goremychkin, E., Osborn, R., McGuire, M., Sefat, A., Jin, R., Sales, B., and Mandrus, D. (2009). Two-dimensional resonant magnetic excitation in BaFe1.84Co0.16As2. *Physical Review Letters*, 102(10):107005.

Luo, H., Yamani, Z., Chen, Y., Lu, X., Wang, M., Li, S., Maier, T., Danilkin, S., Adroja, D., and Dai, P. (2012a). Electron doping evolution of the anisotropic spin excitations in $BaFe_{2x}Ni_xAs_2$. *Physical Review B*, 86(2):024508.

Luo, H., Zhang, R., Laver, M., Yamani, Z., Wang, M., Lu, X., Wang, M., Chen, Y., Li, S., Chang, S., Lynn, J. W., and Dai, P. (2012b). Coexistence and Competition of the Short-Range Incommensurate Antiferromagnetic Order with the Superconducting State of $BaFe_{2-x}Ni_xAs_2$. *Physical Review Letters*, 108(24):247002.

Lv, W. and Phillips, P. (2011). Orbitally and magnetically induced anisotropy in iron-based superconductors. *Physical Review B*, 84(17):174512.

Maier, T., Graser, S., Scalapino, D., and Hirschfeld, P. (2009). Neutron scattering resonance and the iron-pnictide superconducting gap. *Physical Review B*, 79(13):134520.

Maier, T. and Scalapino, D. (2008). Theory of neutron scattering as a probe of the superconducting gap in the iron pnictides. *Physical Review B*, 78(2):020514.

Malaeb, W., Shimojima, T., Ishida, Y., Okazaki, K., Ota, Y., Ohgushi, K., Kihou, K., Saito, T., Lee, C. H., Ishida, S., Nakajima, M., Uchida, S., Fukazawa, H., Kohori, Y., Iyo, A., Eisaki, H., Chen, C. T., Watanabe, S., Ikeda, H., and Shin, S. (2012). Abrupt change in the energy gap of superconducting $Ba_{1-x}K_xFe_2As_2$ single crystals with hole doping. *Physical Review B*, 86(16):165117.

Manousakis, E. (1991). The spin- Heisenberg antiferromagnet on a square lattice and its application to the cuprous oxides. *Reviews of Modern Physics*, 63(1):1–62.

Matan, K., Morinaga, R., Iida, K., and Sato, T. J. (2009). Anisotropic itinerant magnetism and spin fluctuations in $BaFe_2As_2$: A neutron scattering study. *Physical Review B*, 79(5):054526.

Mazin, I. I., Singh, D. J., Johannes, M. D., and Du, M. H. (2008). Unconventional Superconductivity with a Sign Reversal in the Order Parameter of $LaFeAsO_{1-x}F_x$. *Physical Review Letters*, 101(5):057003.

Metoki, N., Haga, Y., Koike, Y., and O nuki, Y. (1998). Superconducting Energy Gap Observed in the Magnetic Excitation Spectra of a Heavy Fermion Superconductor UPd2Al3. *Physical Review Letters*, 80(24):5417–5420.

Mook, H., Yethiraj, M., Aeppli, G., Mason, T., and Armstrong, T. (1993). Polarized neutron determination of the magnetic excitations in $YBa_2Cu_3O_7$. *Physical Review Letters*, 70(22):3490–3493.

Mook, H. A., Lumsden, M. D., Christianson, A. D., Nagler, S. E., Sales, B. C., Jin, R., McGuire, M. A., Sefat, A. S., Mandrus, D., Egami, T., and dela Cruz, C. (2010). Unusual Relationship between Magnetism and Superconductivity in $FeTe_{0.5}Se_{0.5}$. *Physical Review Letters*, 104(18):187002.

Moon, R., Riste, T., and Koehler, W. (1969). Polarization Analysis of Thermal-Neutron Scattering. *Physical Review*, 181(2):920–931.

Müller, G. and Friedrich, J. (2005). Crystal Growth, Bulk: Methods. In *sciencedirect.com.proxy.lib.utk.edu*, pages 262–274. Elsevier.

Nandi, S., Kim, M. G., Kreyssig, A., Fernandes, R. M., Pratt, D. K., Thaler, A., Ni, N., Bud'ko, S. L., Canfield, P. C., Schmalian, J., McQueeney, R. J., and Goldman, A. I. (2010). Anomalous Suppression of the Orthorhombic Lattice Distortion in Superconducting $Ba(Fe_{1-x}Co_x)_2As_2$ Single Crystals. *Physical Review Letters*, 104(5):057006.

Paglione, J. and Greene, R. L. (2010). High-temperature superconductivity in iron-based materials. *Nature Physics*, 6(9):645–658.

Park, H., Haule, K., and Kotliar, G. (2011). Magnetic Excitation Spectra in $BaFe_2As_2$: A Two-Particle Approach within a Combination of the Density Functional Theory and the Dynamical Mean-Field Theory Method. *Physical Review Letters*, 107(13):137007.

Park, J. T., Inosov, D. S., Yaresko, A., Graser, S., Sun, D. L., Bourges, P., Sidis, Y., Li, Y., Kim, J. H., Haug, D., Ivanov, A., Hradil, K., Schneidewind, A., Link, P., Faulhaber, E., Glavatskyy, I., Lin, C. T., Keimer, B., and Hinkov, V. (2010). Symmetry of spin excitation spectra in the tetragonal paramagnetic and superconducting phases of 122-ferropnictides. *Physical Review B*, 82(13):134503.

Prokeš, K., Hiess, A., Bao, W., Wheeler, E., Landsgesell, S., and Argyriou, D. N. (2012). Anisotropy of the (π, π) dynamic susceptibility in magnetically ordered (x=0.05) and superconducting (x = 0.40) $Fe_{1.02}Te_{1-x}Se_x$. *Physical Review B*, 86(6):064503.

Qiu, Y., Bao, W., Zhao, Y., Broholm, C., Stanev, V., Tesanovic, Z., Gasparovic, Y. C., Chang, S., Hu, J., Qian, B., Fang, M., and Mao, Z. (2009). Spin Gap and Resonance at the Nesting Wave Vector in Superconducting $FeSe_{0.4}Te_{0.6}$. *Physical Review Letters*, 103(6):067008.

Qureshi, N., Steffens, P., Wurmehl, S., Aswartham, S., Büchner, B., and Braden, M. (2012). Local magnetic anisotropy in $BaFe_2As_2$: A polarized inelastic neutron scattering study. *Physical Review B*, 86(6):060410.

Regnault, L. P., Bourges, P., Burlet, P., Henry, J. Y., Rossat-Mignod, J., Sidis, Y., and Vettier, C. (1995). Spin dynamics in the high- T c superconducting system YBa 2 Cu 3 O 6+ x. *Physica B: Condensed Matter*, 213:48–53.

Revcolevschi, A. and Jegoudez, J. (1997). Growth of large high-Tc single crystals by the floating zone method: A review. *Progress in Materials Science*, 42(1-4):321–339.

Reznik, D., Ismer, J. P., Eremin, I., Pintschovius, L., Wolf, T., Arai, M., Endoh, Y., Masui, T., and Tajima, S. (2008). Local-moment fluctuations in the optimally doped high-Tc superconductor YBa2Cu3O6.95. *Physical Review B*, 78(13):132503.

Rossat-Mignod, J., Regnault, L. P., Vettier, C., Bourges, P., Burlet, P., Bossy, J., Henry, J. Y., and Lapertot, G. (1991). Neutron scattering study of the $YBa_2Cu_3O_{6+x} system. Physica C : Superconductivity, 185 - 189 : 86 - -92$.

Rotter, M., Tegel, M., and Johrendt, D. (2008). Superconductivity at 38 K in the Iron Arsenide $(Ba_{1-x}K_x)Fe_2As_2$. *Physical Review Letters*, 101(10):107006.

Scalapino, D. J. (1999). CONDENSED MATTER PHYSICS:The Cuprate Pairing Mechanism. *Science*, 284(5418):1282–1283.

Seo, K., Fang, C., Bernevig, B., and Hu, J. (2009). Magnetic properties of the superconducting state of iron-based superconductors. *Physical Review B*, 79(23):235207.

Si, Q. and Abrahams, E. (2008). Strong Correlations and Magnetic Frustration in the High T_c Iron Pnictides. *Physical Review Letters*, 101(7):076401.

Steffens, P., Lee, C. H., Qureshi, N., Kihou, K., Iyo, A., Eisaki, H., and Braden, M. (2012). Splitting of resonance excitations in nearly optimally doped Ba(Fe0.94Co0.06)2As2: an inelastic neutron scattering study with polarization analysis. *arXiv:1210.6386*.

Stock, C., Broholm, C., Hudis, J., Kang, H., and Petrovic, C. (2008). Spin Resonance in the d-Wave Superconductor CeCoIn5. *Physical Review Letters*, 100(8):087001.

Stock, C., Broholm, C., Zhao, Y., Demmel, F., Kang, H. J., Rule, K. C., and Petrovic, C. (2012). Magnetic field splitting of the spin-resonance in CeCoIn5. *arXiv:1203.2189*.

Takagi, H., Uchida, S., and Tokura, Y. (1989). Superconductivity produced by electron doping in CuO_2-layered compounds. *Physical Review Letters*, 62(10):1197–1200.

Tanatar, M. A., Spyrison, N., Cho, K., Blomberg, E. C., Tan, G., Dai, P., Zhang, C., and Prozorov, R. (2012). Evolution of normal and superconducting properties of

single crystals of $Na_{1-\delta}FeAs$ upon interaction with environment. *Physical Review B*, 85(1):014510.

Tokura, Y., Takagi, H., and Uchida, S. (1989). A superconducting copper oxide compound with electrons as the charge carriers. *Nature*, 337(6205):345–347.

Wakimoto, S., Yamada, K., Tranquada, J., Frost, C., Birgeneau, R., and Zhang, H. (2007). Disappearance of Antiferromagnetic Spin Excitations in Overdoped La2-xSrxCuO4. *Physical Review Letters*, 98(24):247003.

Wang, M., Luo, H., Zhao, J., Zhang, C., Wang, M., Marty, K., Chi, S., Lynn, J. W., Schneidewind, A., Li, S., and Dai, P. (2010). Electron-doping evolution of the low-energy spin excitations in the iron arsenide superconductor $BaFe_{2x}Ni_xAs_2$. *Physical Review B*, 81(17):174524.

Wen, J., Xu, G., Xu, Z., Lin, Z. W., Li, Q., Chen, Y., Chi, S., Gu, G., and Tranquada, J. M. (2010). Effect of magnetic field on the spin resonance in $FeTe_{0.5}Se_{0.5}$ as seen via inelastic neutron scattering. *Physical Review B*, 81(10):100513.

Werner, P., Comanac, A., de' Medici, L., Troyer, M., and Millis, A. (2006). Continuous-Time Solver for Quantum Impurity Models. *Physical Review Letters*, 97(7):076405.

Wilson, S., Li, S., Dai, P., Bao, W., Chung, J.-H., Kang, H., Lee, S.-H., Komiya, S., Ando, Y., and Si, Q. (2006a). Evolution of low-energy spin dynamics in the

electron-doped high-transition-temperature superconductor $Pr_{0.88}LaCe_{0.12}CuO_{4\delta}$. *Physical Review B*, 74(14):144514.

Wilson, S., Li, S., Woo, H., Dai, P., Mook, H., Frost, C., Komiya, S., and Ando, Y. (2006b). High-Energy Spin Excitations in the Electron-Doped Superconductor $Pr_{0.88}LaCe_{0.12}CuO_{4-\delta}$ with Tc=21K. *Physical Review Letters*, 96(15):157001.

Wilson, S. D., Dai, P., Li, S., Chi, S., Kang, H. J., and Lynn, J. W. (2006c). Resonance in the electron-doped high-transition-temperature superconductor Pr0.88LaCe0.12CuO4-δ. *Nature*, 442(7098):59–62.

Xu, C., Müller, M., and Sachdev, S. (2008). Ising and spin orders in the iron-based superconductors. *Physical Review B*, 78(2):020501.

Yin, Z. P., Haule, K., and Kotliar, G. (2011). Magnetism and charge dynamics in iron pnictides. *Nature Physics*, 7(4):294–297.

Zhang, C., Wang, M., Luo, H., Wang, M., Liu, M., Zhao, J., Abernathy, D. L., Maier, T. A., Marty, K., Lumsden, M. D., Chi, S., Chang, S., Rodriguez-Rivera, J. A., Lynn, J. W., Xiang, T., Hu, J., and Dai, P. (2011). Neutron Scattering Studies of spin excitations in hole-doped Ba0.67K0.33Fe2As2 superconductor. *Scientific Reports*, 1:–.

Zhang, C. L. (2011). Neutron Scattering Studies of spin excitations in hole-doped $Ba_{0.67}K_{0.33}Fe_2As_2$ superconductor. *Scientific Report*, 1:115 PB –.

Zhang, J., Sknepnek, R., and Schmalian, J. (2010). Spectral analysis for the iron-based superconductors: Anisotropic spin fluctuations and fully gapped $s^{\pm}$-wave superconductivity. *Physical Review B*, 82(13):134527.

Zhao, J., Adroja, D. T., Yao, D.-X., Bewley, R., Li, S., Wang, X. F., Wu, G., Chen, X. H., Hu, J., and Dai, P. (2009). Spin waves and magnetic exchange interactions in CaFe2As2. *Nature*, 5(8):555–560.

Zhao, J., Niestemski, F. C., Kunwar, S., Li, S., Steffens, P., Hiess, A., Kang, H. J., Wilson, S. D., Wang, Z., Dai, P., and Madhavan, V. (2011). Electron-spin excitation coupling in an electron-doped copper oxide superconductor. *Nature Physics*, 7(9):719–724.

Zhao, J., Ratcliff, W., Lynn, J. W., Chen, G. F., Luo, J. L., Wang, N. L., Hu, J., and Dai, P. (2008a). Spin and lattice structures of single-crystalline $SrFe_2As_2$. *Physical Review B*, 78(14):140504.

Zhao, J., Regnault, L.-P., Zhang, C., Wang, M., Li, Z., Zhou, F., Zhao, Z., Fang, C., Hu, J., and Dai, P. (2010). Neutron spin resonance as a probe of the superconducting energy gap of $BaFe_{1.9}Ni_{0.1}As_2$ superconductors. *Physical Review B*, 81(18):180505.

Zhao, J., Yao, D.-X., Li, S., Hong, T., Chen, Y., Chang, S., Ratcliff, W., Lynn, J., Mook, H., Chen, G., Luo, J., Wang, N., Carlson, E., Hu, J., and Dai, P. (2008b).

Low Energy Spin Waves and Magnetic Interactions in SrFe2As2. *Physical Review Letters*, 101(16):167203.

Vita

Mengshu Liu was born in Anyang, Henan, China, on September 12, 1985. She was raised and attended elementary and middle school in Anyang. She graduated from Anyang No.1 High School in in 2004. In July of 2008, She received her Bachelor of Science degree from the Zhengzhou University with a major in physics. She then attended the graduate program in physics at the University of Tennessee in August of 2008.